CORRELATION BETWEEN THE DEGREE OF ALIGNMENT AND OPTO-PIEZOELECTRIC PROPERTIES OF CELLULOSE NANOCRYSTALS FABRICATED FROM WATER HYACYNTH

JACK ABIBO ADEM

A Thesis submitted to the Board of Postgraduate Studies in Fulfillment of the Requirements for the Award of the Degree of Doctor of Philosophy in Physics

SCHOOL OF BIOLOGICAL, PHYSICAL, MATHEMATICS AND ACTUARIAL SCIENCES

JARAMOGI OGINGA ODINGA UNIVERSITY OF SCIENCE AND TECHNOLOGY

DECLARATION

This thesis is my original work and has not been presented for an award of a diploma or conferment of a degree in any other university or institution.

Signature…………………………… ………   Date…………………………………

Jack Abibo Adem

S261/4168/2015

APPROVAL

This thesis has been submitted for examination with our approval as the university supervisors.

1. Signature………………………………….. Date………………………………………….

   Dr. John O. Agumba
   Department of Physical Sciences,
   School of Biological, Physical, Mathematics and Actuarial Sciences
   Jaramogi Oginga Odinga University of Science and Technology

2. Signature……………………………… Date………………………………………….…

   Dr. Godfrey O. Barasa
   Department of Physical Sciences,
   School of Biological, Physical, Mathematics and Actuarial Sciences
   Jaramogi Oginga Odinga University of Science and Technology

This thesis is dedicated to my two sons Rooney Otieno Abibo and Troon Ochieng' Abibo

ACKNOWLEDGEMENTS

TABLE OF CONTENTS

LIST OF FIGURES

LIST OF TABLES

DEFINITION OF KEY TERMS

Amorphous- A material that lacks long range order of the constituent particles

Band gap- Refers to the minimum energy needed to excite an electron from the valence band till a state in the conduction band where it can take part in electrical conduction

Chromophore- A region in the molecule where the energy difference between two separate molecular orbitals falls within the range of the visible light.

Crystallization- Refers to a process where atoms or molecules of a substance align themselves in a well-defined 3-dimensional lattice that minimizes the overall energy within the system.

Degree of polymerization- The number of repeating units

Fluorescence- Refers to the emission of photons from the $S_1 \rightarrow S_0$ radiative transition

Internal Conversion- The non-radiative transition within 2 electronic states in the same spin multiplicity

Intersystem Crossing- The non-radiative transition between two is energetic vibrational levels of electronic states of varying spin multiplicity

Nanocrystals- materials particle having at least one dimension smaller than 100 nanometres

Nanomaterials- Materials possessing, at minimum, one external dimension measuring 1-100nm

Piezoelectricity- Refers to the change of electrical polarization within a material due to external pressure or mechanical stress

Phosphorescence- Refers to a radiative transition between 2 electronic states of different spin multiplicity

Polydispersity- The ratio of weight average to the number average molecular weight

Polymer- Refer to a class of synthetic or natural substances consisting of very large molecules known as macromolecules that are multiples of simpler chemical units referred to as monomers

Polymorphs- A substance to crystallize into different crystalline forms

LIST OF ABBREVIATIONS

ATR FTIR	Attenuated total reflectance Fourier transforms infrared spectroscopy
CF	Cellulose fibre
CNC	Cellulose nanocrystalls
CNF	Cellulose nanofibrils
CMF	Cellulose macrofibrils
DMA	Dynamic mechanical analysis
DMTA	Dynamic mechanical thermal analysis
DSC	Differential scanning calorimetry
DTA	Differential thermal analysis
dTGA	Differential thermogravimetric analysis
FTIR	Fourier transform infrared spectroscopy
HCl	Hydrochloric acid
MCC	Microcrystalline cellulose
MFC	Microfibrillated cellulose
NaOH	Sodium hydroxide
NFC	Nanofibrillated cellulose
NMR	Nuclear magnetic resonance
OM	Optical Microscopy
PET	polyethylene terephthalate
SEM	Scanning electron microscopy
SME	Specific mechanical energy
TAPPI	Technological Association of the Pulp and Paper Industry
TEM	Transmission electron microscope
TGA	Thermogravimetric analysis
UV	Ultraviolet\UV- Vi Ultraviolet-visible light
WH	Water Hyacinth
XRD	X-ray diffraction

LIST OF SYMBOLS

α	Alpha
β	Beta
ºC	Degrees Celsius
cm	Centimetre(s)
cm^{-1}	per centimeter
nm	Nanometer(s) (1 x 10^{-9} meters)
pC/N	picocoulomb per newton
µm	Micrometer(s) (1 x 10^{-6} meters)

ABSTRACT

Cellulose nanomaterials have recently continued to attract higher attention in the current research output, due to their extremely excellent mechanical, optical as well as electrical properties. Their sustainability coupled with good structural and morphological properties have made them become a great resource in the construction of both active and passive components in the electronics sector. Interestingly, water hyacinth, a serious environmental threat in Lake Victoria and other water bodies globally, is a rich source of this novel material. This research study has been dedicated to find out the correlation between the degree of alignment and the piezoelectric effect of cellulose nanocrystals fabricated from water hyacinth. The CNCs were synthesized by a rigorous acid hydrolysis using varied acids, concentration, temperature and time and the effects of these parameters on the opto-structural properties of the resultant films investigated using UV-Vis spectrophotometer, fluorescence spectrophotometer and XRD technique. Further, the Urbach energies have been calculated and found to increase while the optical band gap energies found to decrease with increase in hydrolysis temperature. From a plot of E_g verses E_u, the optical band gap energy of the CNCs when there was no disorder in their microstructure was found to be ~5.43 eV. Further, it has been shown that the Urbach energy is absent when hydrolysis process is done at 14.23^oC. Additionally, the piezoelectric effect of the electric field assisted convective shear assembled CNCs has been systematically studied and the effect of the applied voltage and the frequency mapped. The sensitivity of fabricated sensors was measured using the fabricated measurement setup. From the study, a high degree of CNC orientation in the films has been found to be a key characteristic for the piezoelectric response. The amount of applied voltage and the frequency have been found to increase the degree of the orientation/alignment of the CNCs within the films hence leading to enhanced piezoelectric response. This is because the orientation of crystalline CNC regions inside the films led to a remarkable increase of piezoelectric effect as a result of the large piezoelectric coefficient of the CNCs. From the study, it was clear that functional piezoelectric sensors can be fabricated from CNF films and thus, the results obtained suggests that CNC films are suitable sensor materials for applications in different fields including electronics, biomedical diagnostics and material sciences.

CHAPTER ONE

INTRODUCTION

1.1 Background Information

1.1.1 Outlook

Cellulose nanomaterials possess excellent mechanical properties, are highly transparent, with admirable coefficient of thermal. These characteristics place them at best position to be utilized in fabrication of both active and inactive electronic devices [1]. A case at hand is their ability to be used as substrates for film deposition in electronics industry and visual displays [2, 3]. They have also been excellently used to improve the efficiency of photovoltaic cells [4]. They have equally been proved to act as components of the composites of magnetorestrictive devices [5]. Further, their utility has been harnessed in the creation of the membranes of lithium-ion battery separators [6]. Further, CNMs have often been applied in the manufacture of sensory devices as well as energy harvest and storage tools [7, 8]. The major source of cellulose is plants, both aquatic and non-aquatic. Other minor sources include the tunicates, algae and bacteria. In this research study, we have successfully managed to extract cellulose from the aquatic water hyacinth plant from the Western shores of Lake Victoria, Usenge Beach, Siaya County, Kenya and obtained cellulose nanocrystals (CNCs) from the extract. The obtained CNCs have been subjected to optical absorption measurements, photoluminescence measurements, light microscopy and XRD measurements. Finally, an investigation was conducted on the correlation between the degree of crystallinity of the nanomaterials used in the fabrication of the piezoelectric sensors and the piezoelectric sensitivity.

This chapter outlines the theory of polymers, cellulose structure, cellulose nanomaterials, crystallization theory, light-matter interaction and the theory of piezoelectricity. Finally, we will introduce the objectives, problem statement and justification of the study.

1.1.2 Polymers

Polymer is a term coined from two Greek words, 'poly' and 'mers'. In English, **Poly** means multi or many while **"mers"** means units of high molecular mass. Polymers therefore mean many units

of high molecular weight. Each unit of molecular mass is called a macromolecule. By means of the covalent bonding process, a macromolecule is created by hooking together a very large number of small parts, generally referred to as monomers. The process of chemical reaction where the monomers hook together forming a polymer is called polymerization [9]. Polymers are represented by organic compounds which contain carbon atoms with either hydrogen, nitrogen, oxygen, and/or halogens [10], forming extremely large, chain-like molecules [11]. Due to the wide range of their good mechanical, thermal, optical and even electrical properties, polymers have gained multiple applications in the electronics sector as well as in the manufacture of electronic devices.

Through covalent bonding, large quantity of monomers are embedded together in order to form polymers. [10]. Due to this inter-monomer bonding, the molecular units become dependent. The interdependence of the monomers offers them some degree of freedom that result to polymer's good properties giving them unique behaviors. The total molecular mass of a polymer is directly proportional to its degree of polymerization (DoP). DoP is the integral value the of repeating units. The degree of polymerization of a polymer influences its physical properties such as strength, brittleness, ductility, toughness, malleability, plasticity and elasticity. From data analysis theory, the mathematical mean of the molecular weight of a polymer is given by;

$$\overline{M} = \frac{\sum_{i=1}^{\infty} N_i M_i}{\sum_{i=0}^{\infty} N_i}$$

(1.1)

$\overline{M}$ = mathematical mean of the molecular weight,

N_i = number of monomers in the polymer

N_i = individual monomer molecular weight.

Equation (1.1) is not valid for some optical properties measurements experiments e.g. the light scattering measurements [12]. To take care of this limitation, we use the average weight molecular weight, defined as:

$$\overline{M_n} = \frac{\sum_{i=1}^{\infty} N_i M_i^2}{\sum_{i=1}^{\infty} N_i M_i} = \sum_{i=1}^{\infty} w_i M_i$$

(1.2)

In equation 1.2, we have introduced the term $w_i = \frac{N_i M_i}{\sum_{i=1}^{n} N_i M_i}$ which is basically the weight fraction of M_i. Polydispersity (*PDI*) of a polymer is defined as the ratio of the weight average to number average molecular weight. This is mathematically expressed as;

$$PDI = \frac{M_w}{M_n} \tag{1.3}$$

The molecular size distribution of a polymer is influenced by its polydispersity.

If the weight average of a polymer equals to its number average of the weight of the molecule, then the polymer molecule size is mono-disperse and all the molecular chains have equal lengths. However, if the weight average of a polymer does not match its number average of the molecular weight, then the size is poly-disperse and all molecular chains will have different lengths. This is the most common scenario.

1.1.3   Cellulose

From the available literature, cellulose remains the most abundant organic polymer [13]. It falls in a special class of polymers known as carbohydrate polymer. It comprises a large quantity of hydroxyl groups that are linked by intra-molecular and inter-molecular hydrogen bonds. The main source of Cellulose is wood and plants. In plants, cellulose is richly found in plant cells and biomass. Some of the biomass sources of cellulose are banana rachis, potato tubers, sisal and sugar beet [14, 15]. Interestingly, marine animals (tunicates) [16], bacteria (*Gluconacetobacterxylinus*) [17] and even algae (*Valonia*) [18] also make rich sources of cellulose.

In the interest of this study, cellulose has been extracted from the much-hyped water hyacinth. Research shows that water hyacinth is majorly composed of cellulose, hemicellulose and lignin with percentage compositions of 25%, 33% and 10% respectively. Thus, water hyacinth is a material that is equally best suited to be used in the manufacture of cellulose-based polymers devices [19]. This study has unveiled the cellulose extraction process from the water hyacinth that has always posed a serious environmental threat in Lake Victoria, for better utilization in fabrication of sensory electronics devices. The extracted cellulose has been used to obtain csellulose nanocrystals through pretreatment and acid hydrolysis processes.

1.1.3.1 Cellulose Structure

Cellulose has a flat ribbon-shaped structure formed from a linear chain of glucose molecules which are ringed together. One glucose molecule, which is the repeat unit, is pair of anhydroglucose rings and is given by a general chemical formula $(C_6H_{10}O_5)_n$. The subscript n is an integral number that represents the number of the pairs of anhydroglucose rings making the cellulose. The magnitude of n ranges from 1.0×10^4 to 1.5×10^4 and is largely a factor of the material used as the source of the cellulose. **Figure 1.1a** schematically illustrates the linking pattern of the two anhydoglucose rings. There exists a common oxygen element covalently bonded to the extreme carbon elements from each ring. The oxygen element is bonded to the 1st carbon element (C_1) from ring R_1 and to the 4th carbon element (C_4) from ring R_2. This kind of linkage is commonly referred to as 1-4 linkage since the oxygen elements are linked to the 1st and 4th carbon elements. It forms the generally known β, 1–4 glycosidic bonds [20, 21].
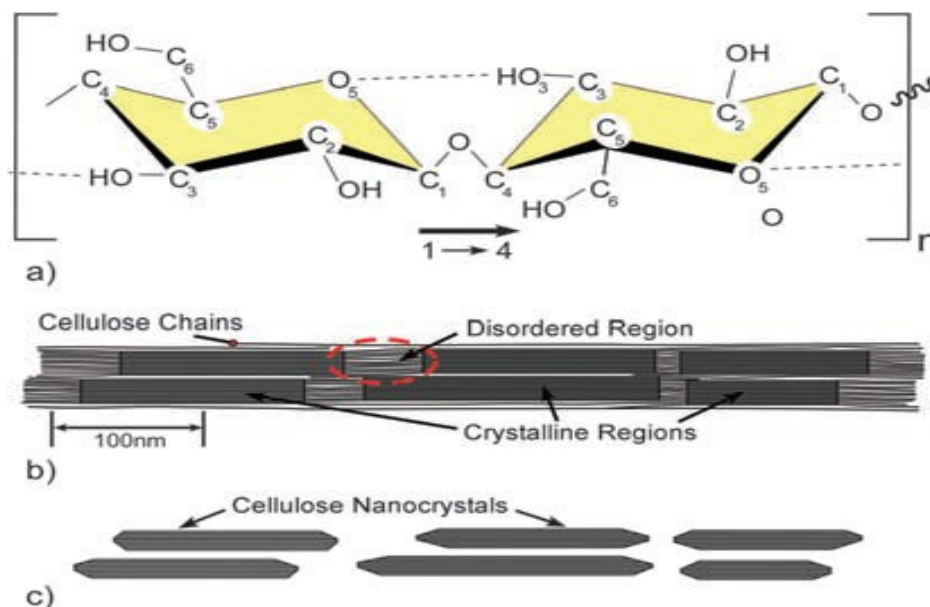
Figure 1. 1: Schematics of the 1-4 linkage pattern of two anhydroglucose rings and the dotted lines showing intrachain hydrogen bonding (a), the amorphous and crystalline zones of the ideal microfibrillar cellulose (b) and cellulose nanocrystals that are fully hydrolyzed with disordered regions fully removed(c) [22]

It is therefore evident that cellulose is clearly a homopolymer of linear trait that comprises of anhydroglucopyranose linked by glycosidic linkage β (1-4) [22]. **Figure 1.1 (a)** shows just one of the repeated segments of the cellulose polymer. This single segment that ever repeats in the chain is called cellobiose and is chemically represented as ($C_{11}H_{22}O_{11}$). Since plants are the most abundant source of cellulose, the tree trunk therefore has a hierarchical structure of cellulose as is schematically presented in **Figure 1.2**.
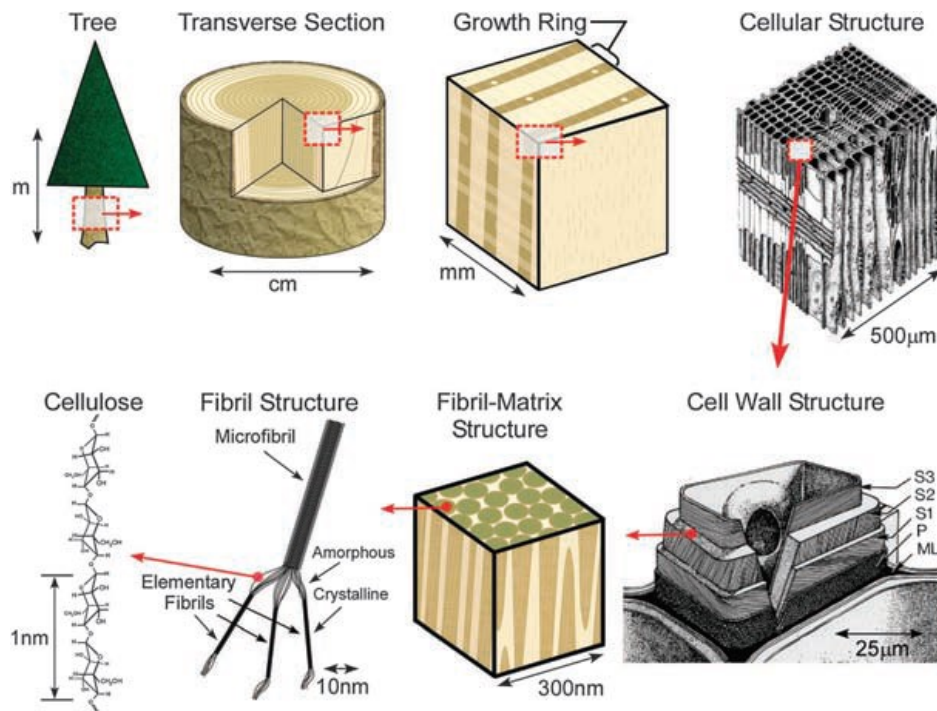
Figure 1. 2: A schematic of how a plant can be hierarchically reduced from tree trunk in the unit-scale to cellulose in the nanoscale [23]

1.1.3.2 Cellulose Polymorphs and their Cellulose Crystal Structures

Naturally, cellulose exists in four unique Crystalline Structures. The crystalline structures enable us to categorize cellulose as Cellulose I, Cellulose II, Cellulose III and Cellulose IV. The first crystalline structure, Cellulose I, is the natural cellulose since it is produced naturally by living organisms like plants, bacteria, algae and the marine-based tunicate. Cellulose I has unstable

crystalline structure and has thermodynamic metastability. As such its structure can be thermodynamically converted to form either cellulose II or III. Cellulose II can be obtained from Cellulose I through regeneration process followed by mercerization processes [23]. Interestingly, Cellulose II exists in monoclinic structure. Of all the polymorphs of cellulose, Cellulose II is the most stable polymorph [23]. The formation of Cellulose III is achieved by subjecting Cellulose I or II to liquid ammonia treatment. Once Cellulose III is obtained, we simply subject it to further thermal treatments to obtain Cellulose IV.

In terms of crystalline structure, Cellulose I exists in two structures. These are the triclinic structure and the monoclinic structure. The triclinic structure is symbolically represented as (Iα) while monoclinic structure is represented as (Iβ) [24]. As discussed earlier, cellulose sources are majorly plants, algae, bacteria and tunicates. Each of these sources have their unique dominant polymorphs. Algae and bacteria make the dominant polymorph for Iα structure [25, 26], whereas plant and tunicates make the dominant polymorph of Iβ structure [27]. Research has shown that Iα polymorph is quite metastable. A study unveils that Iα can be successfully be transformed to Iβ by subjecting it to hydrothermal therapy in alkaline solution [25, 28]. Further, high temperature treatment of Iα while submerged in organic solvents and helium gas can easily yield Iβ [29]. In another parallel study, it was shown that subjecting Iα to a rigorous annealing process can easily yield Iβ [30]. XRD measurements on the two polymorphs were successfully performed by Nishiyama and his co-workers [31,32]. Their neutron fiber diffraction and synchrotron XRD measurements gave the following results:

The unit cell measurements for Iα and Iβ are as follows;

For Iα: a = 0.672 nm   α = 118.081   For Iβ; a = 0.778 nm   α = 134.081

       b = 0.596 nm   β = 114.801   b = 0.820 nm   β = 130.801

       c = 1.040 nm   γ = 80.3751.38   c = 1.038 nm   γ = 96.51.37,

Electron diffraction studies on the two structures were also done and findings unraveled that the major disparity between Iα and Iβ is that their cellulose sheets have relative displacements along the (110) triclinic plane and (200) monoclinic planes in the direction parallel to the chain axis [33].
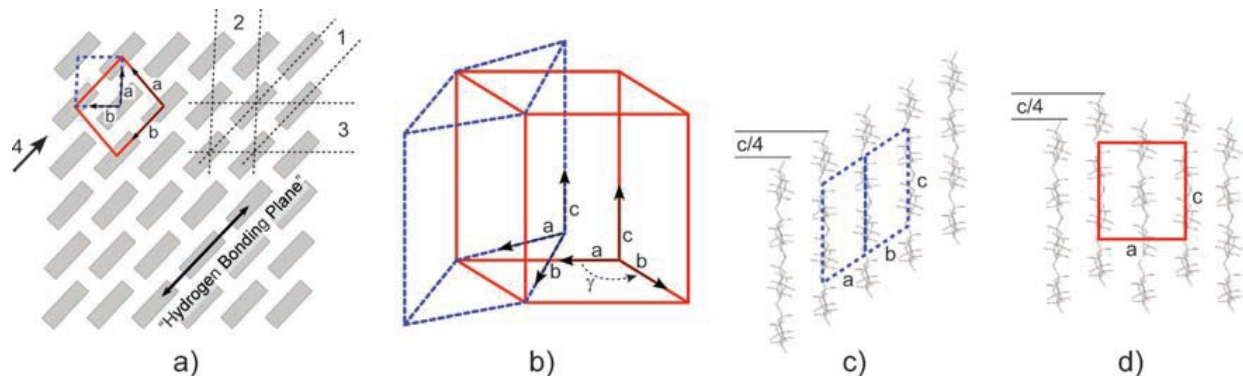
Figure 1. 3: Geometric representation of the triclinic unit cells for cellulose Iα triclinic unit cell (shown by dashed lines) and that of cellulose Iβ monoclinic unit cell (shown by solid lines)

Figure (a) shows the parallelogram shape of both Iα and Iβ unit cells as projected along the c-axis. Figure (b) the configuration of Iα relative to Iβ unit cell. Figure (c) shows the translation of the sheets of the hydrogen bonding of Iα quarter way along of the positive c side, and Figure (d) shows the translation of the hydrogen bonding sheets Iβ quarter way along the alternating positive c side [22, 33].

1.1.3.3. From Cellulose to Nanocellulose

There are two broad processes of extraction of nanocellulose, these are acid hydrolysis and mechanical treatment process. Acid hydrolysis of cellulose material yields cellulose nanocrystals while mechanical treatment yields cellulose nanofibrils. The nanomaterials produced, CNCs and CNFs, have completely different properties even if the source materials are similar. The two classes of the CNMs have totally different crystallinity, distinct elastic property, unique flexibility and even unmatched aspect ratio. The flow chart represented in **Figure 1.4** shows the general procedure for obtaining the nanocellulose materials from cellulose product.
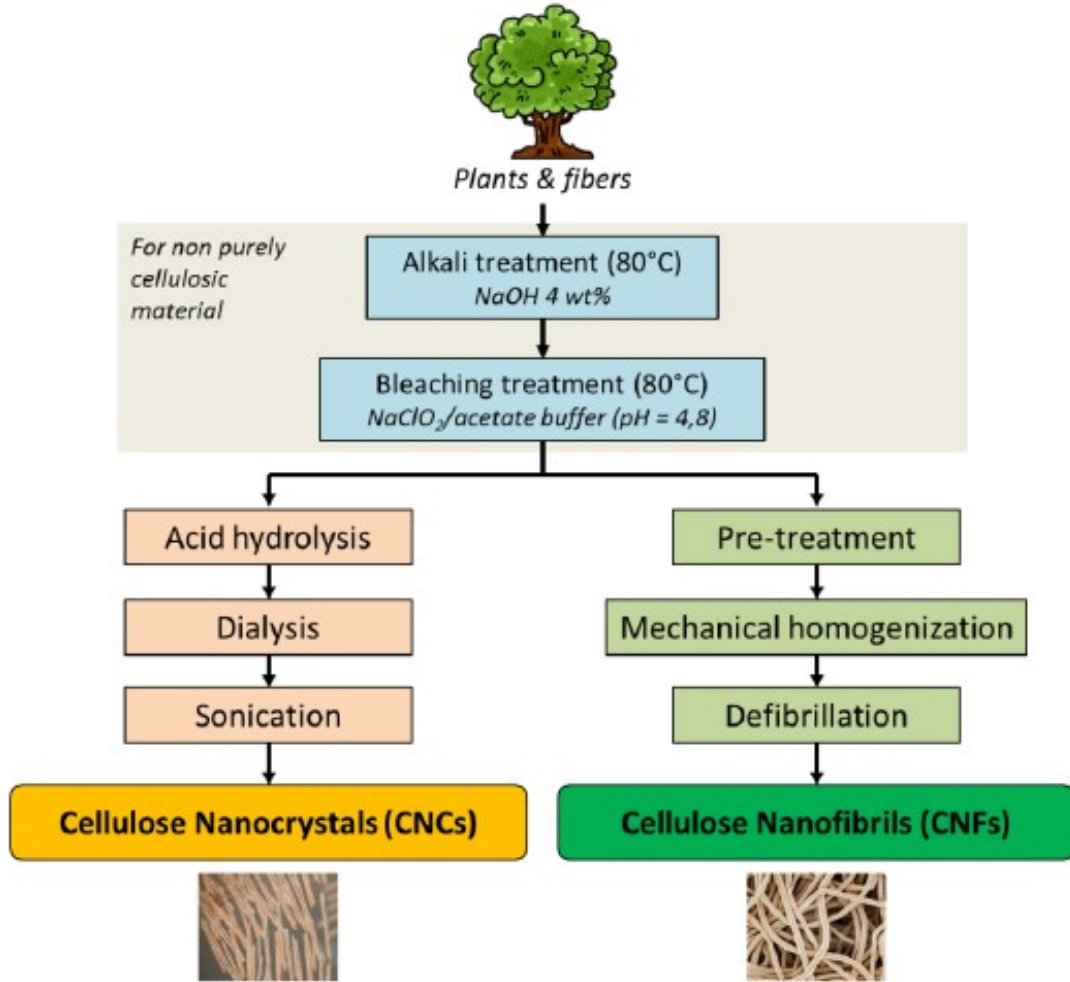
Figure 1. 4: The Flow chart of the extraction process of CNCs and CNFs from cellulose source material [23]

Cellulose Nanofibrills

Herrick and Turbak were the first scientists to discover CNFs [34]. In their study, they made a milestone by successfully extracting CNFs from cellulosic fibers. They subjected cellulosic fiber suspensions to mechanical fibrillation whereby the suspensions were repeatedly made to flow through a homogenizer having very high pressure [34, 35]. This rigorous mechanical process weakens the bonds that link elementary fibrils to bundled fibrils enhancing the creation of CNFs. In the current material science research, new methods for mechanical fibrillation have been discovered and put in play. These include grinding, micro-fluidization and homogenization. In

each case the source material suspension is passed through the process repeatedly until fine CNFs are obtained. However, the obtained CNFs consist of both amorphous and crystalline zones. The acid hydrolysis process eliminates the amorphous region. Therefore, subjecting CNFs to acid hydrolysis finally yields CNCs, which are devoid of the amorphous regions.

Cellulose Nanocrystals

In the recent past, a lot of research activities have shifted focus to the research on the primary and industrial properties of the cellulose-based nanoparticles [36-38]. This has been propelled by their unique fascinating properties. As explained earlier in section 1.1.3.1, cellulose, naturally, is a fabric of intrachain and interchain hydrogen bonding web. This bonding property makes its fibrils to have high axial stiffness enhancing its stability. Cellulose fibrils thus remain the main reinforcement materials for cellulose sources like plants, bacteria, algae and tunicates. The fibrils of cellulose are made of amorphous and crystalline regions. Crystalline zones are the regions where the chains of cellulose are stacked in a periodic structure while the amorphous zones are the regions where the cellulose chains are stacked in a non-periodic manner. To obtain CNCs, we extract the crystalline regions through hydrolysis process. In the process of acid hydrolysis process, the amorphous zone gets eaten away resulting to a purely crystalline structure referred to as cellulose nanocrystals. This was well illustrated in **Figure 1.1 c)**.

1.1.4   Extraction of CNC

The extraction process of cellulose nanoparticles from a source material laden with cellulose is a two-stage procedure, the pretreatment stage and the hydrolysis stage.

1.1.4.1 The Pretreatment Stage

At this stage, the source material is subjected to high degree of purification and a further homogenization process to enable it react more consistently in subsequent treatments. The specific objective of the pretreatment process is to eliminate the non-cellulosic materials from the cellulose source material [34]. The non-cellulosic molecules in cellulose are like lignin,

hemicelluloses, and protein. Once the non-cellulosic materials are removed the cellulose molecules become accessible to reagents in the subsequent stages. Each cellulose source material has its unique non-cellulosic material targeted for elimination by the pretreatment process. For plants and wood, the non-cellulosic material is the matrix materials which are basically hemicellulose, lignin, and protein while that of tunicates, algea and bacteria are the mantel, algal wall matrix and bacterial matrix media respectively. Pretreatment process for plants and wood basically involves alcoholic synthesis. For both algae and bacteria sources, it involves a thorough culturing procedure followed by series of washing. The protocol adopted by Titik I. *et al* [19] for the pretreatment process was adopted in this study.

1.1.4.2 Hydrolysis Stage

This is the second stage of CNC extraction from source material. The main goal of hydrolysis process is to separate the pure cellulose materials into its two distinct components; the crystalline and microfibrillar components. It is generally called acid hydrolysis since it is chemically induced through a high level of control of the physical parameters. The amorphous regions in the extracted cellulose make regions of structural defects which are easily attacked by the acid. As such, by subjecting the cellulose into highly controlled timing, temperature and acid concentration, we can fully get rid of the amorphous regions through acid erosion leaving behind stable and strong crystalline regions. The acid hydrolysis process can be given a chemical insight. The hydronium ions (H_3O+) present in the acid penetrates through the chains of cellulose present in the amorphous regions enhancing the hydrolytic cleavage of the glycosidic bonds consequently yielding individual crystallites [39, 40]. **Figure 1.5** illustrates the acid hydrolysis mechanism. Acid hydrolysis process is basically a 4-steps procedure, namely: subjecting the pretreated cellulosic material into strong acid hydrolysis through controlled timing, temperature, acid concentration parameters; Culmination of the hydrolysis reaction through water dilution; Repeated washing followed by intense centrifugation in order to fully eliminate any excess acid in the product; And finally, thorough dialysis using distilled water with the aim to fully get rid of free acid molecules and any soluble sugars possibly present.
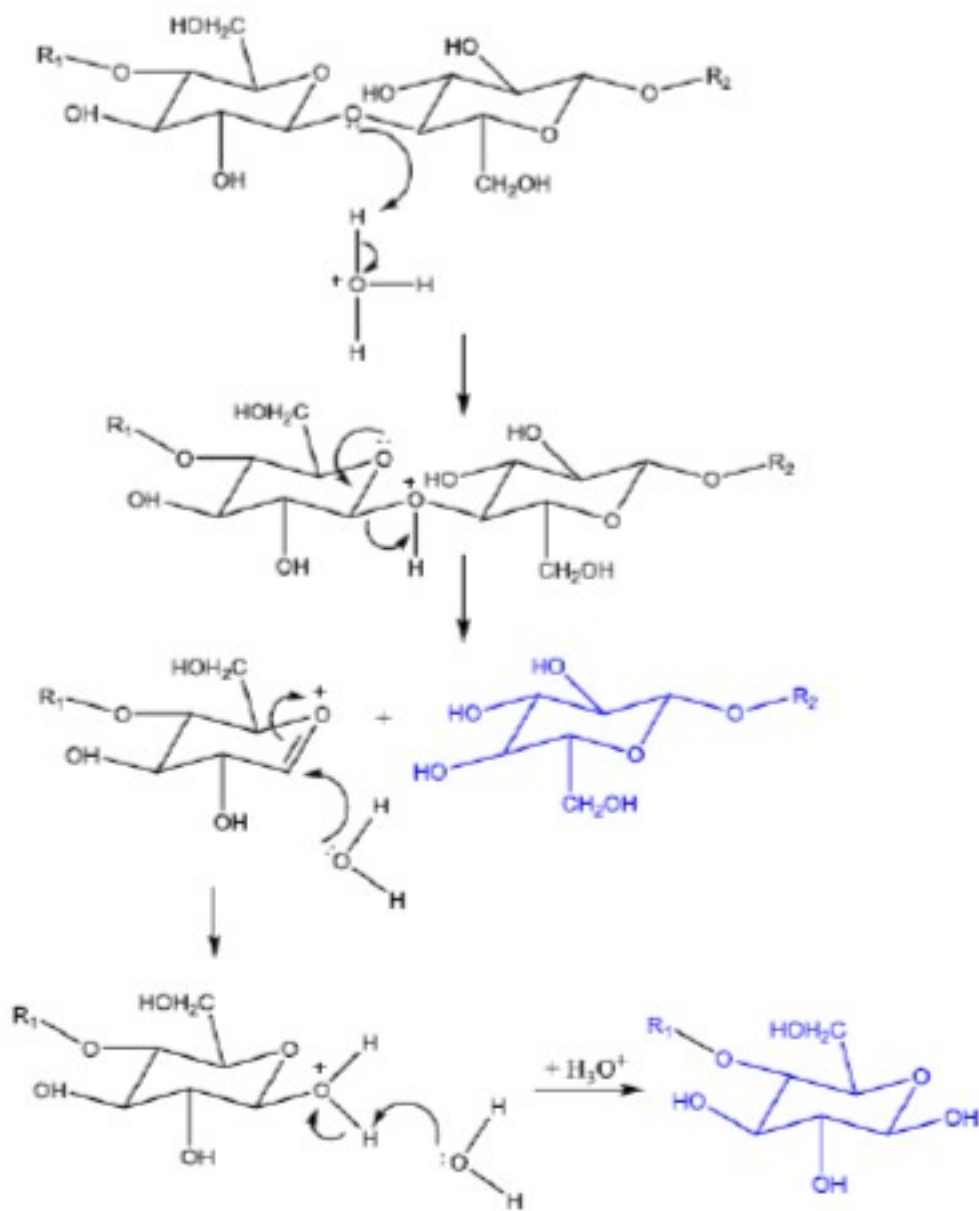
Figure 1. 5: Chemical chain flow of the acid hydrolysis reaction mechanism [41]

The crystalline structure, morphology, density, polymorphism, physical, chemical, electrical, optical characteristics of the synthesized CNCs are a factor hydrolysis time-span, thermodynamic temperature, type of the acid and concentration of the acid used for chemical hydrolysis [42, 43]. Different acids yield CNCs with different abilities to disperse in polar solvents.

11

1.1.5   Properties of Cellulose Nanocrystals

As reported earlier, Cellulose nanocrystals have displayed very important unique chemical and physical properties that make them highly regarded in the manufacture of electronic sensory devises as well as energy sourcing and storage devices [44, 45]. Specifically, CNCs have been proved to be highly hydrophilic, have good thermal stability, adamant to chemical corrosion, have admirable mechanical properties, are of low density and even low thermal conductivity.

Even though they are highly hydrophilic, CNCs are insoluble not only in water but also in all organic solvents. In regard to thermal stability, CNCs decompose just before melting when exposed to excess heat, a property also known as thermoplasticity. They are known to be resistant to chemical attack as they defy chemical derivatization. CNCs have highly desired mechanical properties. For instance, it's tensile strength is very high as well as its stiffness. For this reason, they have proved to be very useful as reinforcing elements in polymeric composites. Worth noting is the fact that the structure and final chemical and physical properties of extracted CNCs are basically determined by two major factors; the primary material used as the cellulose source and the procedure adopted for the extraction CNCs from the cellulose source material.

Figure 1.6 a-c, show Transmission Electron Micrographs of CNCs extracted from different sources. It illustrates how different cellulose sources as well as polymorphism influence the final shape and size of the nanoparticles [44]. From the figure, we can observe the glaring morphological difference between the native wood pulp fibers and the mercerized wood pulps. The CNCs from wood and Glaucocysts **(Figure 1.6 a, b)** correspond to Cellulose I polymorph while that from Lyocell **(Figure 1.6 c)** correspond to Cellulose II polymorph.
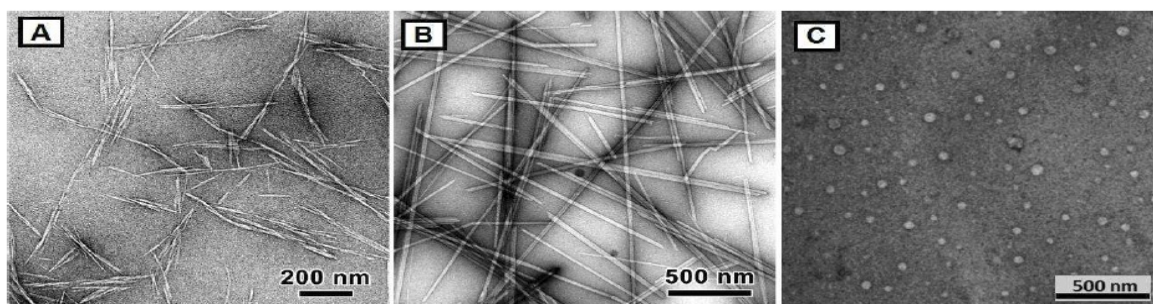
Figure 1. 6: TEMs of CNCs that are negatively stained from different sources: a) wood; b) Glaucocystis; c) Lyocell [44, 45]

1.1.6   Applications of CNCs

Cellulose nanocrystals possess highly admirable unique characteristics. These make them best suited in vast applications in various sectors. Their good properties include large specific surface area, low density, high specific strength, high aspect ratio, highly reactive hydroxyl groups, non-abrasiveness, non-toxicity, biocompatibility, polymorphism and ability to be biodegradable. Following their amazing chemical and physical properties originating from their unique structure, CNCs have enjoyed utility in most fields. They are considered as materials of high value since they can improve the performance of most available electronic products. They have been equally used to come up with new products in several industries. In paper and paint industry they have been used as reinforcement additives, emulsion thickeners and rheology modelling tool [23] and paint stabilizer. In biomedical industry, CNCs have proved to be very useful as pharmaceutical binders, biosensing agent and bioimaging appliance. In polymer nanocomposite field CNCs play a significant role as the chief reinforcement tool. Cellulose Nanocrystals therefore provide a wide range of potential applications in fields such as packaging and biomedicine.

Other sectors, worth mentioning, where CNCs have been predominantly applied include beauty and therapy industry, textiles industry, automotive sector, aerospace environment and electrical industry [44, 46]. This study investigated the relationship between the linearity of CNC crystals and their electric response to surface pressure and obtained a novel application of water hyacinth based CNCs as piezoelectric sensors. **Figure 1.7** shows the illustration of different cellulose nanocrystals field of application.
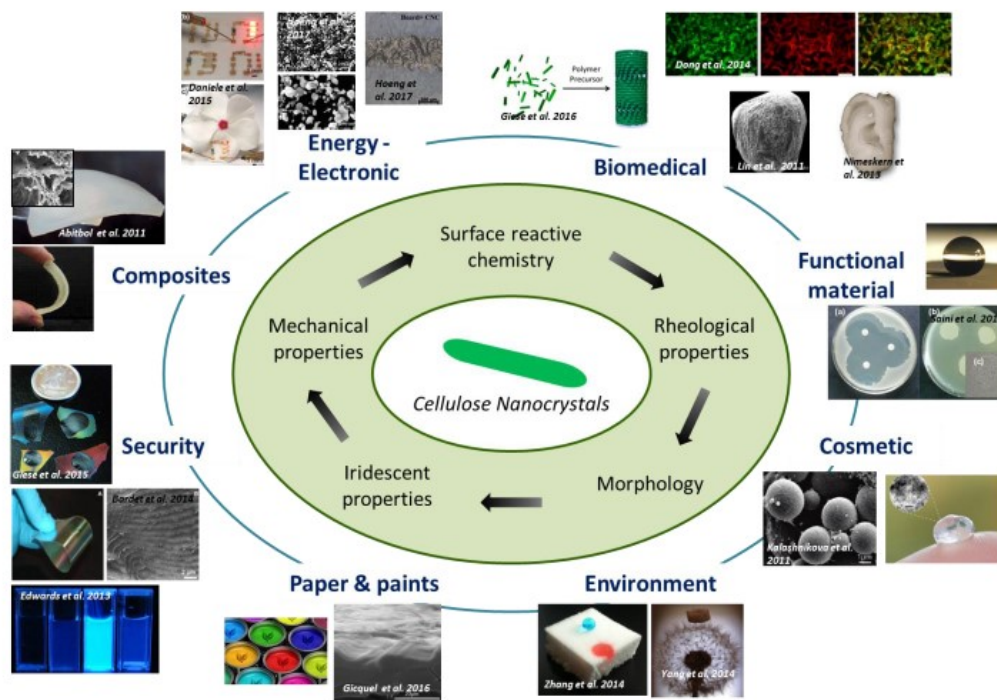
Figure 1. 7: The vast application fields of cellulose nanocrystals [23]

1.1.7 Physics of Polymer Crystallization

Polymers are made up by linking an enormous number of repeating molecular units known as monomers via covalent bonding [10]. The repeating units form the backbone of the polymer macromolecule. Side groups and side chains may be attached to the backbone chain. The backbone and the attached side groups determine whether the polymer becomes electrically neutral or conjugated. When a polymer has an ever alternating single and double bonds, then it is referred to as conjugated polymer. They contain overlapping π- orbitals that create a system of mobile π-electrons that gives the polymer a semiconducting ability that makes its way into electronic device applications. During polymerization of conjugated polymers, there occurs crystal imperfections leading to disorders in the long-range structure. This has hindered most scientists in achieving optimum ideal applications of these conjugated polymers in electronic industry [47]. To improve on the polymer applications, there are several methodologies that are adopted. One of the methodologies is to conduct molecular ordering of the chains of the polymer chains through the crystallization process which has since remained one of the most important

subjects of polymer science. The conformations of the polymer chains and their crystallinity index have great impact on their final physical properties. Early scientists who studied polymer crystallization were mainly interested on the final crystalline structure and their morphology [48, 49]. Initially, polymer crystallization theories were adapted from theories that were developed for the describing crystallization process of metals and small-sized molecules. The initial findings revealed that the major different methods adopted in the crystallization processes for the small-sized molecules and metals for the long-chain polymers resulted to much deviating results in terms of the size, shape and stability of the yielded polymer crystals [50]. Earlier studies in polymers have shown that crystals can be grown from supercooled melts or solutions [51, 52]. Both complex and simple polymers can crystallize. The simple polymers are made of linear polymer structures. Examples of simple polymers are polystyrene and polyethylene [53]. From experimental research, polymer crystallization process cannot yield a purely perfect crystalline polymer whose crystallinity index is 100%. The index of crystallinity for a crystalline polymers always lies approximately in the range of 10% to 80%, an indicator that some small quantity of amorphous structures are still present in a crystalline polymer [10]. Crystallinity of a polymer highly influences its brittleness. The higher crystallinity, the higher the brittleness. It is the amorphous region of the polymer that gives the polymer toughness. A polymer with more amorphous region has the ability to bend without breaking and the ability to absorb impact energy. Both the crystallinity and the preferential orientation of the crystals have great influence on the characteristics of a crystalline polymer [54].

1.1.7.1 Factors Affecting Polymer Crystallization

The crystallization rate and growth rate of a perfect crystal depend on the number of molecules that are transported and deposited to the crystal and the ease with which the molecules attach on the surface of the seed crystal. Good number of molecules should be available at the growth front to enhance the crystal growth. Attraction of far-flung molecules to the growth front should equally be enhanced. This is achieved by increasing and/or controlling the concentration or diffusion rate of molecules in the solution or melt. The molecules should not just stay at a fixed point where they arrived first, but through the attachment and detachment possibilities, molecules should settle on a seed where the Gibbs free energy is as minimal as possible. If this is

not the case, then defects such as cavities would not be done away with. The attachment possibility of any given molecule to a growth front and the growth rate of a crystal is effectively controlled by temperature [55]. For a crystal to grow, then the temperatures should be lower than the melting temperature for a solid or dissolution temperature for a solution. The attachment and detachment rates are similar at the melting or dissolution temperature, thus no observable crystal growth. Based on the *"diffusion limited aggregation"* (DLA) theory, the higher the probability of surface attachment of molecules, the higher the diffusion rate of the molecules to the crystal front hence the higher the crystal growth rate [56]. Since polymers have long chains which are highly entangled with interpenetrating chains, polymer crystallization from seed crystals in solved or molten states is still a challenge to date.

1.1.7.2 Nucleation

Nucleation process is the initial stage of changing from the mother phase (liquid or gas) to the solid phase. This is a first order phase transition. Nucleation and controlled rate of nuclei formation are the main factors which determine the final crystal number density, size, their perfection, and polymorphism [57-59]. Nucleation falls into two main categories; homogenous nucleation and heterogeneous nucleation. Homogenous nucleation occurs spontaneously while heterogeneous nucleation is induced. The size of the final crystal formed therefore greatly depends on the probability of nucleation and the rate of the crystal growth. Reducing the temperature of solution below the dissolution temperature makes molecules less stable. This makes the molecules diffuse in the fluid and they may arrange themselves to form solid clusters and as the result, the solid-liquid interface is established. The bulk material has a lower energy than the solid-liquid boundary [54]. The smallest cluster of the solid phase is called a nucleus. The transformation of liquid into nuclei requires a certain amount of energy. From the Gibbs free energy law, the net change in free energy of a system must be balanced by the energy gained when creating a new volume and the energy lost during the creation of new interfaces. This is given Gibbs free energy equation (1.4).

$$\Delta G = \Delta G_S + \Delta G_V \tag{1.4}$$

Where ΔG_s is the Surface/Area energy required to create a surface and is always taken as a positive term. ΔG_V is the Volume/Bulk energy that drives the transformation for a spherical cluster of radius r and is always taken as negative term. In case the resultant change in Gibbs free energy is less than zero, then nucleation is highly enhanced.

For a spherical nucleus of radius r, then equation (1.4) becomes;

$$\Delta G = 4\pi r^2 \gamma - \frac{4}{3}\pi r^3 \varepsilon \qquad (1.5)$$

Where;

$\gamma =$ the constant for the surface energy

$\varepsilon =$ the constant for the volume energy.

γ is the liquid-solid interface tension force between the aggregate and solution while ε is the free change in energy per unit volume associated with phase transition [60]. Equation (1.4) can be represented graphically by the energy potential diagram. **Figure 1.8** shows volume energy change, surface free energy change and total free energy change variation with nuclei radius during the cluster formation process. When the size of the cluster increases from zero to a size r^*, there is a proportional increase in the total free energy from zero to a maximum value at radius r^*. The radius r^* is known as the critical radius. Past the critical radius, a further increment in the size of the cluster gives a decrement in net change in free energy. This shows that the energy needed to drive the transformation of a spherical cluster is much smaller than that needed to form a surface.
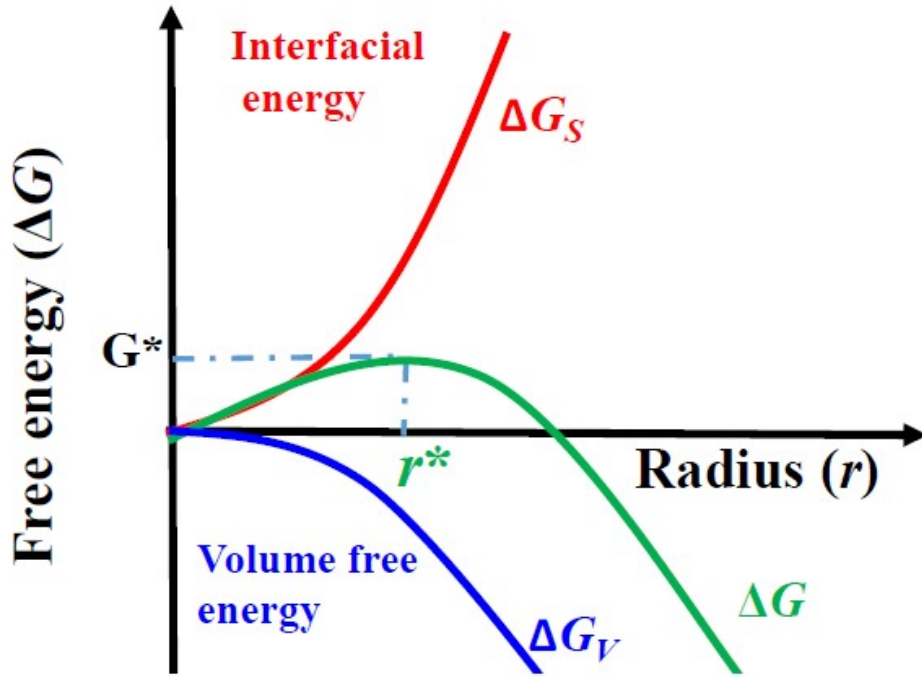
Figure 1. 8: A graphical representation of the net change in free energy variation with nuclei radius during nucleation [61]

A cluster of the critical size at the critical radius is called a nucleus. Once a nucleus reaches the critical size at radius r^*, then growth starts. At the point where the critical radius r^* is reached, the free energy becomes maximum. The nuclei whose sizes are less than the critical size are therefore said to be unstable and thus more energy is needed to add a molecule to the surface of such nucleus. In that state, the unstable nucleus is referred as an embryo.

Mathematically, at the critical size, the equation (1.5) will satisfy;

$$\frac{d\Delta G}{dr} = 0 \tag{1.6}$$

Evaluating the differential in Equation (1.5), we obtain the critical radius as;

$$r^* = \frac{2\gamma}{\varepsilon} \tag{1.7}$$

Substituting the critical radius Equation (1.7) into Equation (1.5) we obtain;

$$\Delta G^* = \frac{16\pi\gamma^3}{3\varepsilon^2}$$

(1.8)

The critical radius, r^*, of the cluster material at critical size at a nucleation temperature T always decreases with increasing undercooling.

Let T_m be the temperature at the melting point in Kelvin,

    L be the latent heat of fusion and

    ΔT be the undercooling,

then the critical radius r^* becomes;

$$r^* = -\frac{2\gamma}{\Delta G_V} = \left(\frac{2\gamma T_m}{L}\right)\left(\frac{1}{T_m - T}\right) = \left(\frac{2\gamma T_m}{L}\right)\left(\frac{1}{\Delta T}\right)$$

(1.9)

In a polymer solution the rate of nucleation is a factor of several parameters of the solvent such as temperature of the solution, solution concentration, energy of the intermolecular interactions and energy of the polymer-solvent interactions. Equation 1.4 can equally be expressed in terms of latent heat of fusion H and entropy S in the form;

$$\Delta G = \Delta H - T_c \Delta S$$

(1.10)

Where;

    T_c = the temperature of crystallization,

    ΔH = the net change in latent heat of fusion,

    ΔS = the net change in entropy

The equilibrium melting temperature is reached when the free energy is equal to zero and is denoted by $\left(T_m^0\right)$. From equation (1.9), taking the free energy value, ΔG, to be zero, we obtain

$$T_m^0 = \frac{\Delta H}{\Delta S}$$

(1.11)

The actual melting temperature depends on the lamellar thickness l [62] and their relationship is given by the Gibbs-Thomson law given in equation (1.12) below.

$$T_m = T_m^0 \left(1 - \frac{2\sigma}{l \Delta H T_m^0} \right) \qquad (1.12)$$

The constant σ is the free energy area density of interfacial surface of the spherical nuclei.

Heterogeneous Nucleation takes place when a solid particle of the solute is added to its solution. The added particle is the nucleation agent and is generally referred to the seed crystal. The nucleation agent may be hung freely in the liquid or embedded on the inner walls of the vessel containing the liquid. For heterogenous nucleation to occur successfully, the following three conditions must be achieved:

There must be an energetic barrier to diffusion, $\left(E_{diff} \right)$

There must be energetic barrier to desorption $\left(E_{des} \right)$,

There must be thermodynamic barrier for formation of stable nuclei $\left(\Delta G^* \right)$.

From the above parameters the nucleation density, N, of stable clusters can be given by the equation

$$N = R \alpha e^{\frac{E_i}{kT}} \qquad (1.13)$$

Where;

R = Molecule deposition rate,

α = the constant for Critical cluster size,

k = Boltzmann's constant,

T = Thermodynamic temperature of the solution, and

E_i = The Energy associated with crystal disintegration,

The Crystal disintegration energy E_i is approximated to be equal to the negative crystal free energy of formation, ΔG^*. Therefore, the product of homogeneous nucleation and a function of the contact angle (ζ) basically give the effective free energy needed during heterogeneous nucleation. The contact angle (ζ) is that between a liquid and solid on the surface of the seed crystal. The net free energy required for the heterogeneous nucleation process is therefore expressed as;

$$\Delta G_{het} = \Delta G_{hom} \times f\left(\zeta\right) \tag{1.14}$$

$$\text{Where} f(\zeta) = \frac{2 - 3\cos\zeta + co^{\ 3}\zeta}{4}$$

From equation 1.14, we observe that the total free energy needed for the process of heterogeneous nucleation is always less than the free energy required for the homogeneous nucleation process. This is well shown in **Figure 1.9**.
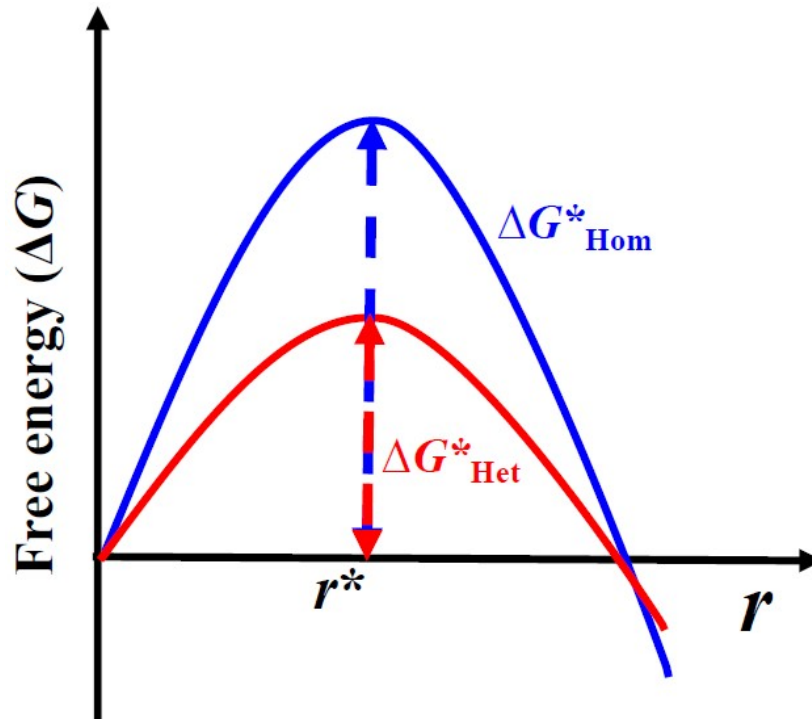
Figure 1. 9: Comparison of the effective free energy for homogeneous nucleation ΔG^*_{Hom}

Versus that of heterogeneous nucleation ΔG^*_{Het} [63]

Polymer crystallization is therefore a two-steps procedure, the nucleation process followed by crystal growth process. During the nucleation process, nucleus formation occurs either by heterogeneous or homogeneous nucleation process [10]. As was discussed in section 1.1.7.2, nucleation process occurs at sizes of radius below $r*$ where the embryo is unstable. For sizes larger than $r*$, the crystalline state will become stable enhancing the induction of the crystallization process. From the thermodynamic perspective, the effective free energy required for stable nucleation can also be expressed as;

$$\Delta G^* = \frac{16\pi\sigma^3 \left(T_m^0\right)}{3\left(\Delta H\right)^2 \left(\Delta T\right)^2} \tag{1.15}$$

Where $\Delta T = T_m^0 - T_c$, with T_c being the crystallization temperature.

From equation 1.15, we observe that the free energy needed to nucleate, ΔG^*, and $\Delta T = T_m^0 - T_c$, obey the inverse square law. The undercooling processes highly influence the nucleation rate, $\varphi_{nuc.}$ The rate of nucleation greatly reduced with decreased undercooling while it increases exponentially with increased undercooling [64, 65]. The rate of nucleation can therefore be expressed as,

$$\varphi_{nuc} = e^{\frac{\sigma^2\left(T_m^0\right)}{\left(\Delta H\right)^2 \left(\Delta T\right)^2}} \tag{1.16}$$

Another important point worth noting is that nucleation barrier is not a factor of the molecular length forming the chain. However, it is very sensitive to the surrounding environmental conditions [66].

1.1.7.3 Crystal Growth

The process of crystal growth commences immediately just after the nucleation process. During the crystal growth, molecules move towards the growth front and get embedded on to the structure [67-70]. The rate of crystal growth must be made as slow as possible to produce a perfect crystal. Slow growth rate minimizes crystal defects and yields admirable molecular ordering [71, 72]. Further, the crystal growth rate depends on two factors, namely; the quantity of the molecules moved to the seed crystal and the probability of molecular attachment. Temperature controls the attachment probability of a molecule to a growth front and thus the growth rate of a crystal [55]. Normally, crystal growth takes place at temperatures that are below the melting point. When the undercooling is made constant, then the growth of a nucleated crystal lamella takes pace through a secondary nucleation process [73]. This secondary nucleation results in an increase of free energy. If we consider a secondary nucleation taking place in two growth directions given by g and G each having stem thickness of a and b respectively, then the incremental change in free energy is given according to;

$$\Delta G_1^* = 2bl\sigma_L - \varphi abl\Delta\mu \tag{1.17}$$

Where φ = Apportioning parameter and

$\nabla\mu$ = The term representing the volume energy,

In equation 1.17, the free energy of the folded surface for the first stem is assumed. Immediately after this first process, the secondary nucleus then spreads in the lateral dimensions with a new growth rate g. This initiates a second term of the free energy increase given by;

$$\Delta G_2^* = 2bl\sigma_e - \varphi abl\Delta\mu \tag{1.18a}$$

Therefore, the rate of deposition of the first stem is given as;

$$A_0 = \beta e^{-bl\left(\frac{2\sigma_L - \varphi abl\Delta\mu}{kT}\right)} \tag{1.18b}$$

Where β = the velocity of the polymer segments towards the growth front.

However, the rate to remove the first and subsequent stems is expressed by;

$$B = \beta e^{\left(\frac{(\varphi-1)abl\Delta\mu}{kT}\right)} \tag{1.19}$$

Similarly, the deposition rate for the second and the subsequent stems can be expressed as;

$$A = \beta e^{-b\left(\frac{2\sigma_e + \varphi l\Delta\mu}{kT}\right)} \tag{1.20}$$

From earlier experimental studies the radial growth rate is not a factor of time [74]. The crystal growth process can be broken into three different parts namely; the initial seeding step (pre-factor), G_0, the diffusion part, G_D and the nucleation part, G_N [74, 75].

The general growth rate of a crystal is therefore given by;

$$G(T) = G_0 * G_D * G_N = G_0 e^{-\left(\frac{U*}{R(T_C - T_0)}\right)} e^{-\left(\frac{Kg*}{T_C\Delta T}\right)} \tag{1.21}$$

Where G_0 = Pre-factor,

G_D = The diffusion part

G_N = The nucleation part of the crystal growth rate

$U*$ = The energy of activation for the diffusion of the molecule chain into the crystal surface.

K_g* = The energy of activation for secondary nucleation,

R = Universal gas constant and

T_0 = The temperature measurement when the diffusion process completely stops.

1.1.8 Interaction of Light with Matter

When ultraviolet and visible light interact with molecules, photon may be absorbed. The absorption of the photon by the valence electrons leaves them in an excited state whereby they undergo transition from ground state to higher electronic state known as the energized or excited state. In this excited state, electrons reside in the lowest occupied molecular orbitals (LOMO). The Absorption of photons by matter occurs in a very short time span of about 10^{-15} seconds leading to change in the electronic structure of the molecule absorbing the photon. However, the process does not alter the atomic nuclei positions within the molecule. The energy at the ground state is denoted as E_0 while that of the excited state at the nth electronic level is denoted as E_n. The absorbed photon energy hv therefore makes the electron undergo transition from energy level E_0 to E_n. The absorbed energy is therefore the difference of the two energy states and can be expressed as;

$$hv = E_n - E_0 \tag{1.22}$$

Similarly, when an electron undergoes transition from a higher to a lower electronic state, then photon energy in the order hv is emitted.

1.1.8.1 Frank-Condon Principle

Light energy propagates through space in discrete form of wave packets. Each discrete wave packet is called a photon. Each packet has energy which has a specific energy related to a certain frequency or wavelength. The photon energy is given by;

$$E = hv = h\frac{c}{\lambda} \tag{1.23}$$

Where;

h = The Plank's constant, $h = 6.626x10^{-34} Js$,

λ = The wavelength of the incident light.

c = The speed of the incident light, and

v = The frequency of the incident light.

During light-matter interaction, light absorbance, transmittance and reflectance occur. That is, part of the light energy gets absorbed, other part gets transmitted while some fraction undergoes reflection. As was given in equation 1.22, absorbed energy of the photon equals to the net change in energy from the energy of the highest occupied orbital (OO) to the energy of the closest unoccupied orbital (UO). This is given by the relation;

$$E_{light} = h\nu_{light} = h\frac{c}{\lambda_{light}} = \Delta E_{UO} - E_{OO} \tag{1.24}$$

The frequency of the ultraviolet or visible light needed to energize an electron from the stable ground state to the excited state is chiefly dependent on chemical component of the absorbing molecule. This is because the energy gap from the topmost occupied orbital (OO) energy the nearest unoccupied orbital (UO) energy also depends on chemical identity of the molecule [75]. **Figure 1.10** shows the electronic configuration before and after absorbing a photon of light.
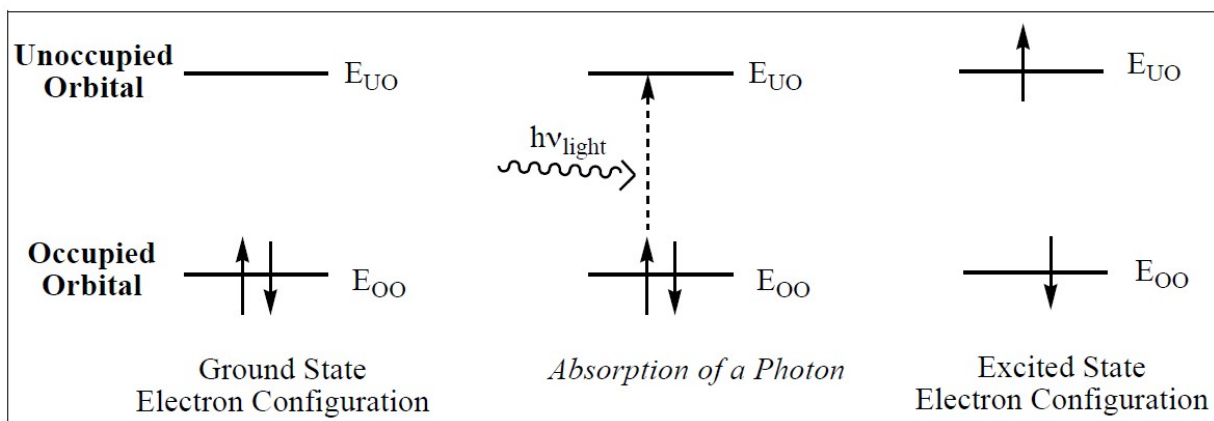
Figure 1. 10: Electronic configurations before photon absorption and at post photon absorption [75]

The intensity of electronic transitions is explained by Frank-Condon principle. The principle is widely used in spectroscopy and quantum physics. The electronic transitions are caused by the changes in electronic and vibrational energies that always occur simultaneously when a molecule absorbs or emits photon energy. Frank-Condon principle states that during the process of electronic transition, the probability of a transition from one vibrational energy level to another is

highly increased when there is significant overlap of the two vibrational wavefunctions. **Figure 1.11** shows the Franck-Condon diagram. It shows the maximum region of overlap of the ground quantum state with the excited quantum state. One of the assumptions in this principle is that electronic transition occurs only within a stationary nuclear framework. This is on the basis that during the electronic transition process, electrons move much faster than nuclei making the nuclei to remain effectively stationary with respect to the whole atomic structure. Consequently, in the event that electronic excitation takes place much faster compared to the nuclei movement, then the wave function should not remain constant [76].
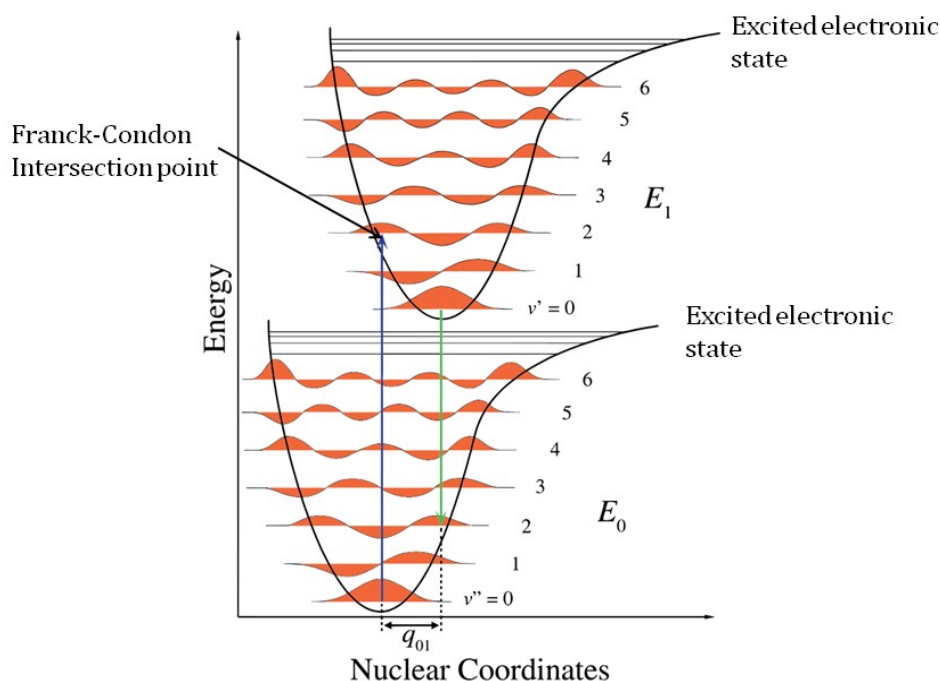
Figure 1. 11: A typical Franck-Condon diagrams showing the maximum overlap of the excited quantum state and ground state [76]

1.1.8.2 Perrin-Jablonski Diagram

During light-matter interactions, transitions of electrons occur to higher electronic states. These transitions can be either radiative or non-radiative. Perrin-Jablonski diagram is a graphical illustration of the excited states, energy levels, and non-radiative & radiative transitions that can possibly take place during photo-excitation. It is therefore chiefly used in fluorescence

spectroscopy. This important transition visualization tool was developed by two scientists, Jean Perrin and Jablonski. Jean Perrin robbed in the idea of resonant energy transfer between molecules. He explained the concept of delayed fluorescence that is aggravated thermally (metastable state) [77]. This, he did with the aid of a visualization energy level diagram that enabled him to demonstrate how light radiation undergoes absorption and emission processes. [78]. Jablonski, on the other hand, developed the tool by introducing the component of radiative transition process whereby the electron undergoes transition from higher electronic state (excited state) falling back to the stable ground state creating a phenomenon known as phosphorescence. **Figure 1.12.** shows a schematic Perrin-Jablonski.
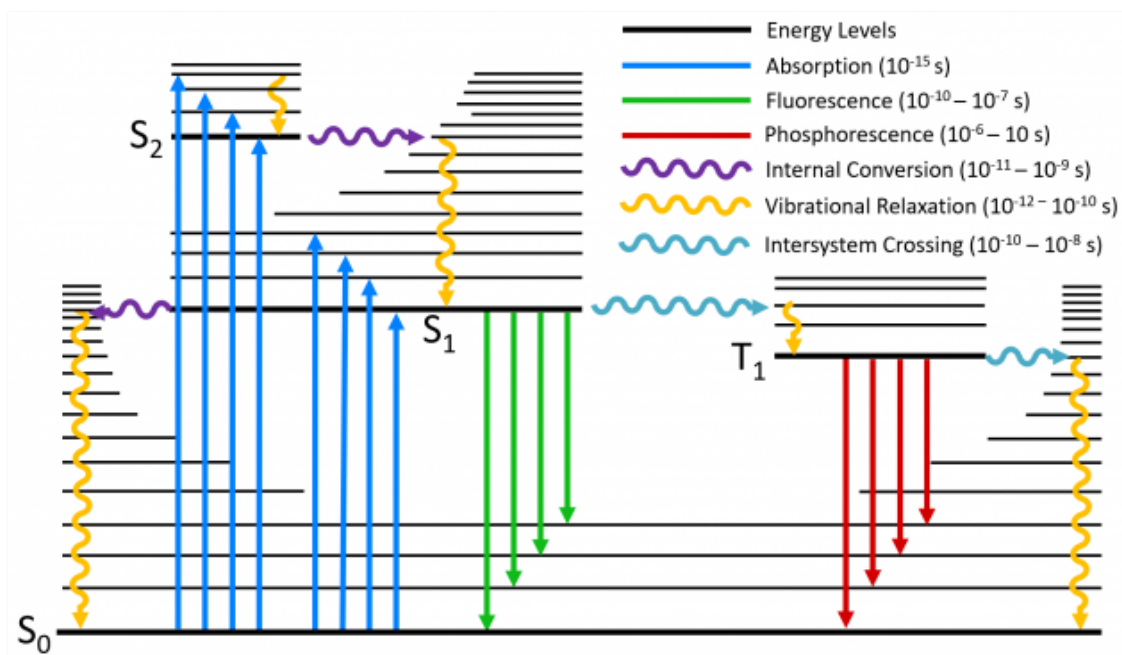
Figure 1. 12: A Schematic Perrin-Jablonski diagram with full illustrations of energy levels and all radiative and non-radiative transitions [79]

The orbital energy levels and the transitions in **Figure 1.12** are discussed in the section below.

Energy Levels

The energy levels are represented by the black horizontal parallel lines. The energy magnitude of the energy levels increases as we move vertically upwards (y- axis of the diagram). Energy levels with lower vibrational levels are represented by bolder lines and vise versa. The spacing of the vibrational levels get closer with the increase in energy and vise-versa. The effective spin angular momentum has great impact on the nomenclature of the electronic states. The electronic states whose total spin angular momentum is zero are referred to as Singlet states, represented by letter S while those whose total spin angular momentum is one are referred to as triplet states, demoted by letter T. The subscript integer on the S and T denote the number of the excited state relative to the ground state. For instance, S_0 is interpreted to mean the singlet ground state. S_1 denotes the first excited singlet state while S_n represents the arbitrary n^{th} excited singlet state.

1.1.8.3 Radiative & Non-Radiative Transitions

There are two types of transitions that can occur during light-matter interactions. These are Radiative & Non-Radiative Transitions. In the Jablonski diagram, (**Figure 1.12**), they are shown by the colored arrows. In radiative transitions, the electron undergo transition from one energy state to another after absorbing or emitting a photon. They are shown by straight colored arrows. On the other hand, in non-radiative transitions, the electron moves from one energy state to another without absorbing or emitting a photon. In the Jablonski diagram, they are represented by wavy arrows. When a molecule's surface receives an incident light, the light's photon energy is converted to increase the molecule's internal energy. Absorption is therefore said to have taken place. A molecule that has absorbed photon energy rises from the low ground state to occupy a higher excited state. Absorption process is the fastest radiative transition and takes place in a time span of 10^{-15} seconds. Fluorescence is a radiative transition that involves the emission of photons from S_1 retrieving back S_0. Fluorescence occurs rapidly faster but slightly lower than the rate of absorption. Its timescale varies from 1.0×10^{-10} to 1.0×10^{-7} seconds. They are represented using the arrows in green in **Figure 1.12.** Since fluorescence involves a rapid emission of photons from the lowest vibrational level of the S_1 state to the S_0 state, it consequently creates a net loss in energy. This energy loss due to fluorescence process can be

explained by popularly known Kasha's Rule which asserts that luminescence takes place with quantifiable yield when the transition is only from the least excited state of a given multiplicity [80]. The rule is consistent with the Stokes-Shift phenomenon where fluorescence of a material takes place at a greater wavelength compared to that of the absorption process, creating wavelength shift. Delayed fluorescence takes place when a molecule transition takes place from the first excited triplet state, T_1, to the first excited singlet state S_1 followed by a radiative transition to the singlet ground state S_0. Because of the elongated route, it results to an emission similar to standard fluorescence but with an elongated timescale [81]. Delayed fluorescence can take place through two unique mechanisms as discussed below.

Thermally Activated Delayed Fluorescence is a delayed fluorescence in which the molecule undergoes transitions from the first excited triplet state, T_1 falling back to the first excited singlet state, S_1 via reverse intersystem crossing. It is said to be thermally activated since the molecules must acquire enough thermal energy sufficient enough to overcome the resistance offered by the energy gap that exists between the electronic states S_1 and T_1. This delayed fluorescence type is also referred to as the E-type delayed fluorescence since its discovery was made using eosin fluorescent compound. [78]. Triplet-triplet annihilation delayed fluorescence is a type of delayed fluorescence that involves the transition of two molecules initially in the T_1 state. When the two molecules undergo such a transition one molecule gets energized and becomes promoted to the S_1 state while the other molecule emits a photon and perches down to the S_0 state. This delayed fluorescence type is also referred to as the P-type delayed fluorescence since its discovery was made using Pyrene fluorescent compound. **Figure 1.13** summarizes the two mechanisms of delayed fluorescence.
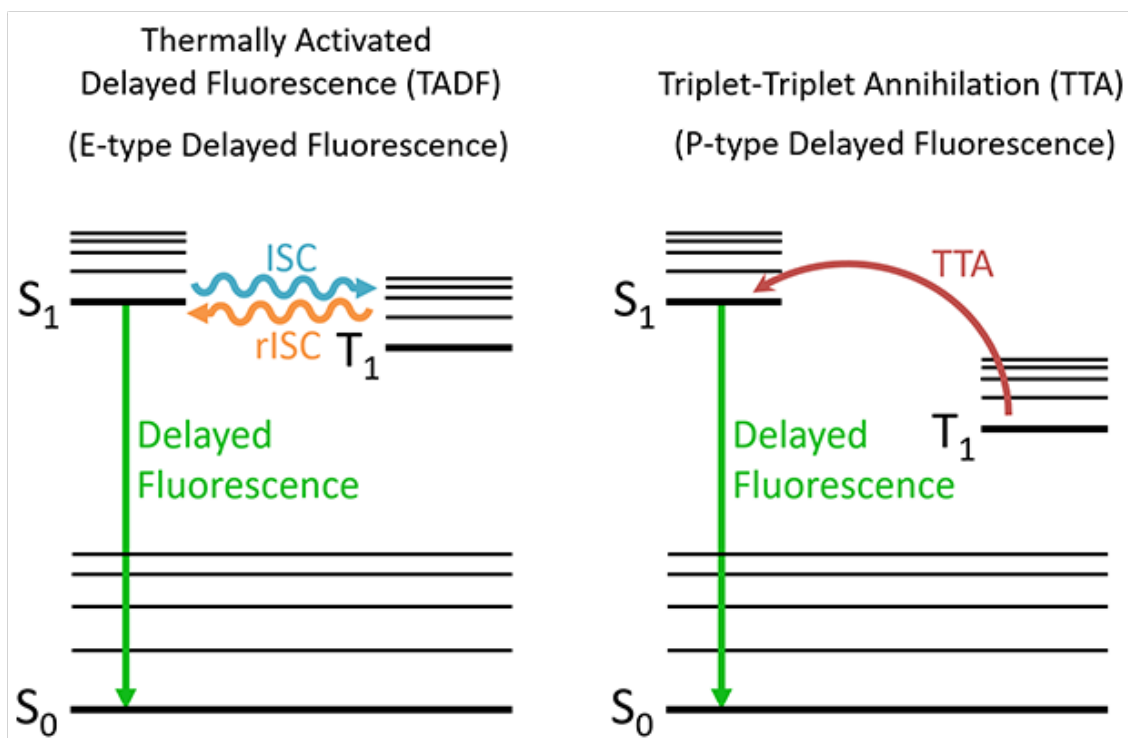
Figure 1. 13: E-type and P-type delayed fluorescence mechanisms [81]

Phosphorescence is a radiative transition process in which a molecule emits a photon to undergo a transition from the first excited triplet state to the singlet ground state, i.e. from $T_1 \rightarrow S_0$ states. Phosphorescence is transition that is forbidden just as was witnessed with the intersystem crossing, However, it meekly occurs via spin-orbit coupling. Being a forbidden process, phosphorescence takes place on a highly elongated timescale relative to that of fluorescence. Its approximate timescale ranges from 10^{-6} to 10^{-8} seconds.

The Non-Radiative Transitions include vibrational relaxation, internal conversion and intersystem crossing. There exist various vibrational levels within one electronic state. Vibrational relaxation is said to occur when a molecule undergoes a transition from an upper vibrational level of a given electronic state to a lower vibrational level of the same electronic state. After absorbing photon energy, a molecule gets promoted to an excited state where it

becomes unstable and would then be in dire need to regain stability. As such, it will dissipate energy gained so as to resettle down at the ground state. During the energy dissipation process, the first means of energy loss takes place via vibrational relaxation process in which the excess vibrational energy is dissipated to intermolecular and intramolecular modes of vibrational. Vibrational relaxation is too rapid and occurs on a scale of 10^{-12} to 10^{-10} seconds. It is indicated by the orange arrows in **Figure 1.12**. Internal Conversion is said to take place when a molecule undergoes transition from one electronic state to the other electronic state of the same total angular spin. An excellent example of an internal conversion occurs when a molecule undergoes transition from a singlet electronic state at a higher level to occupy a singlet electronic state at a lower level through internal conversion. To regain full stability, internal conversion must be immediately preceded by vibrational relaxation for the molecule to settle in the vibrational level of the least energy. As opposed to internal conversion, Intersystem crossing is that transition that takes place when a molecule changes its occupancy between two electronic states of different spin multiplicity. For instance, in the event a molecule gets energized to rise from S_1 to T_1 state, it is said to have undergone intersystem crossing. In **Figure 1.12**, this non-radiative transition is shown by the colored arrows.

1.1.8.4 The Born–Oppenheimer Approximation

When an electron absorbs a photon, it gets excited. At the excited state the electron gains kinetic energy which can cause it to either; vibrate, rotate, and even display both electric and nucleic attractions. This phenomenon was summarized by the Born–Oppenheimer (BO) approximation. In this approximation, it is assumed that all these motion effects can be categorized into electronic part and the nuclear part. Thus, the effective wave function for such an excited molecule is the algebraic sum of the wave function of the electronic part and that of the nuclear part. The electronic component will constitute the vibrational and rotational energies while the nuclear components will constitute electrical and nucleic attraction energies. The net energy of excitation is therefore the algebraic sum of these individual energy components.

$$E_{tot} = E_{elec} + E_{vib} + E_{rot} + E_{nuc} \tag{1.25}$$

Where;

E_{tot} = Total Energy

E_{elec} = Electrical Energy

E_{vib} = Vibrational Energy

E_{rot} = Rotational Energy

E_{nuc} = Nuclear Energy

In BO approximation, it is further assumed that the electronic wave function is dependent of only the nuclear positions. The velocities of the nuclear vibrations do not affect the wavefunctions. From quantum mechanics principle, when the Hamiltonian of a system is split into distinct parts then its net eigenfunction is the product of the individual eigenfunctions of the split Hamiltonian terms. Likewise, the total eigenvalue of such a system is the algebraic sum of individual eigenvalues of the split Hamiltonian terms. From the BO approximation, it was assumed that the excitation energy of a molecule can be separated into electronic and nucleic parts. We therefore consider a Hamiltonian of an excited molecule that is separable into two terms. Let one term involve space coordinate q_1 and the second term involve space coordinate q_2. Therefore, the Hamiltonian can be expressed as

$$H = H_1(q_1) + H_2(q_2) \tag{1.26}$$

The overall Schrödinger equation of such a system will take the form

$$H\psi(q_1, q_2) = E\psi(q_1, q_1) \tag{1.27}$$

Let us consider the total wavefunction of such a system to take the form

$$\psi(q_1, q_2) = \psi_1(q_1)\psi_2(q_2) \tag{1.28a}$$

then

$$H\psi(q_1, q_2) = (H_1 + H_2)\psi_1(q_1)\psi_2(q_2)$$
$$H\psi(q_1, q_2) = H_1\psi_1(q_1)\psi_2(q_2) + H_2\psi_1(q_1)\psi_2(q_2)$$
$$= E_1\psi_1(q_1)\psi_2(q_2) + E_2\psi_1(q_1)\psi_2(q_2)$$
$$= (E_1 + E_2)\psi_1(q_1)\psi_2(q_2)$$
$$= E\psi_1(q_1)\psi_2(q_2)$$
$$= E\psi(q_1, q_2) \tag{1.28b}$$

Thus, in consistency with the quantum mechanics theory, we observe that the net eigenfunction of H is the product of individual eigenfunctions of H_1 and H_2. On the other hand, the net eigenvalues of H is the sum of individual eigenvalues of H_1 and H_2.

1.1.9 Piezoelectric Effect of CNCs

1.1.9.1 Theoretical Considerations of the Piezoelectric Effect

A phenomenon whereby an application of an external force on a surface of a material causes change in charge distribution in the material is called piezoelectricity. Such a material that undergoes change in distribution in its charges due to the application of an external force is said to be a piezoelectric material. Thus, piezoelectricity can be simply defined as stress dependent change in polarization. When two electrodes are connected to a piezoelectric material in such a way that one lies on the upper surface and the other on the lower surface, quantifiable amount of voltage can be measured across the two electrodes. Cellulose nanocrystals have been proved to have this noble property of piezoelectricity. Piezoelectricity phenomenon can be explained from the atomic model. When a piezoelectric material is not subjected to any externally sourced stress, the centroids of its positive and negative charges from all the molecules perfectly overlap making the whole medium to be electrically neutral. On the other hand, on application of an externally sourced stress makes the internal reticular undergo deformation which results to the alienation of the negative and positive centroids of the molecules leading to generation of little dipoles which induce fixed charges on the surface. Thus, during polarization, the applied mechanical stress is transduced into electrical energy. A simple electrical circuit can be designed whereby two electrodes are connected on the extreme surfaces of a piezoelectric film with a galvanometer connected to the two terminals (electrodes). When the material's surface is pressed, fixed charge density is created on the surface and current will be seen registered on the galvanometer. Polarization therefore creates an electric field that enhances the flow of free charges in the circuit.

On the withdrawal of the external force, the polarization ceases immediately. The ceasing of polarization makes the free charges to flow in the reverse reinstating the initial equilibrium state of the piezoelectric material. When a galvanometer is connected to such a system, it would display the two opposite sign current peaks. The piezoelectric effect has remained a fundamental phenomenon applied in several energy tapping techniques that convert mechanical energy from vibrations [82, 83] into electrical energy form which can be used to run machines. The generation of electricity by application of external pressure, discussed so far, is referred as direct

piezoelectricity. However, there is also reverse piezoelectric effect where application of voltage across two electrodes can cause mechanical deformation. The reverse piezoelectricity has been chiefly applied in nano-positioning devices. The linear theory piezoelectricity holds that at low-scale, mechanical stress generates low-scale electric fields, producing a linear profile [84, 85]. From this linear theory of piezoelectric effect [83-85], the created fixed charge density in a piezoelectric material, P_{pz}, is directly proportional to the externally applied Tension, T as per;

$$P_{pz} = d \times T \tag{1.29}$$

where P_{pz} = polarization vector of piezoelectricity,

d = The strain coefficient of piezoelectricity

Similarly, mechanical strain S_{pz} generated in the reverse piezoelectricity can be expressed as;

$$S_{pz} = d \times E \tag{1.30}$$

Where E = The magnitude of the electric field applied.

Applying the elasticity property of the piezoelectric substance, we can derive a relation between the direct and reverse piezoelectricity as;

$$P_{pz} = d \times T = d \times c \times S = e \times S \tag{1.31}$$

$$T_{pz} = c \times S_{pz} = c \times d \times E = e \times E \tag{1.32}$$

Where;

c = The elastic constant due to the applied stress

T = The strain applied on the material.

The applied strain T is a factor of mechanical strain S and can be expressed as

$$T = c \text{x } S \tag{1.33}$$

The piezoelectric effect increases the stiffness of a material. This is well explained in the steps below. Consider a piezoelectric material under application of external strain S. The impact of this strain will lead to generation of both elastic stress T_e, and piezoelectric polarization P_p. The polarization will finally induce electric field in the material E_{pz} expressed as;

$$E_{pz} = \frac{P_{pz}}{\varepsilon} = \frac{e \times S}{\varepsilon} \tag{1.34}$$

Where the symbol ε represents the dielectric constant of the piezoelectric substance

Analogous to Lenz law of electromagnetism, the electric field generated by piezoelectric effect creates a mechanical stress which acts in the reverse direction relative to that of the externally

applied stress. The net stress on the material T is therefore the sum of the stress produced by the electric field T_{pz} and the stress produced from the elastic property of the material T_e, according to;

$$T = T_e + T_{pz} \tag{1.35}$$

$$T = cxS + \frac{e^2}{\varepsilon}xS \tag{1.36}$$

$$T = \left(c + \frac{e^2}{\varepsilon}\right) \times S \tag{1.37}$$

$$T = \bar{c} \times S \tag{1.38}$$

Where $\bar{c}$ = the piezoelectrically stiffened constant.

Equation 1.40 illustrates the fact that piezoelectric effect increases stiffness of the piezoelectric material as it increases the elastic constant.

Further, when an external electric field is applied between the two terminals of a piezoelectric substance having a dielectric constant ε, then an electric displacement directed towards the terminals is created. This leads to generation of surface charge density. This electric displacement D is a factor of the externally applied electric field according to the equation;

$$D = \varepsilon \times E \tag{1.39}$$

The externally applied electric field E equally produces a strain that that can be expressed as;

$$P_{pz} = e \times S_{pe} \tag{1.40}$$
$$P_{pz} = e \times d \times E \tag{1.41}$$

The strain due to the reverse piezoelectricity can take a negative or a positive value. This is dependent on the direction of the external electric field relative to that of the poling field. In a piezoelectric circuit, there exists a net free charge density that is observed on the electrodes. This effective free charge density is the algebraic sum of the charge density due to vacuum and the charge density induced by the dielectric medium, mathematically expressed as;

$$\sigma = \sigma_0 + \sigma_d = \varepsilon_0 \times E + \chi \times E = \left(\varepsilon_0 + \chi\right) \times E \tag{1.42}$$

Where ε_o = the vacuum dielectric permittivity due to vacuum and

χ = the dielectric susceptibility of the material.

It is worth noting that the strain on a material takes a positive value if the direction of the external field is similar to the direction of the poling field. In such a state, the material will definitely undergo extension along the direction of the poling field. Essentially, there is an increase in the charge density on the surface of a dielectric material undergoing polarization when the directions of applied external field and that of poling field coincide. The increment in the surface charge density can be expressed as;

$$P_{pe} = e \times S_{pe} = e \times d \times E \tag{1.43}$$

In the event the magnitude of the electric field is kept constant, then the additional polarization caused by the piezoelectric effect will definitely increase the electric displacement of free charges as they approach the electrodes by the same quantity, i.e,

$$\sigma_{pe} = P_{pe} \tag{1.44}$$

The total electric displacement D is therefore given as:

$$D = \varepsilon \times E + P_{pe} = \varepsilon \times E + e \times d \times E = \varepsilon \times E \tag{1.45}$$

where ε is the effective dielectric constant.

Practically, piezoelectric effect is a phenomenon that cuts across the elastic variables and the dielectric variables. The elastic variables are the mechanical stress denoted by T and mechanical strain denoted by S while the dielectric variables are the electric charge density denoted by D and electric field denoted by E. Use of linear electro-elastic constitutive equations have been made to explain this coupling of elastic and dielectric variables in piezoelectricity. Tensor relations that relate S, T, D and E are given by;

$$S_p = S_{pq}^E T_g + d_{pq} E_k \tag{1.46}$$

$$D_i = d_{iq} T_q + \varepsilon_{ik}^T E_k \tag{1.47}$$

where, s_{pq}^E = the elastic compliance tensor at constant electric field,

ε_{ik}^T = dielectric constant tens or under constant stress,

d_{iq} = piezoelectric constant tensor,

S_p = the mechanical strain in p direction,

D_i = electric displacement in i direction,

T_q = mechanical stress in q direction, and

E_k= electric field in k direction.

The tensor relations above are useful in determining the electromechanical response of a piezoelectric film in the direction of the stimulus. In a piezoelectric material, directions of stretch, perpendicular axis and polarization axis can be marked with integral values. Similarly, their corresponding shear directions can equally be marked. In essence, the stretch direction is marked as 1 while the axis that is perpendicular to this stretch direction is marked as 2. The axis of polarization which is always orthogonal to the film surface is marked as 3. The shear plane that is perpendicular stretch direction is marked 4. Similarly, the shear directions that are perpendicular to 2 and 3 are marked 5 and 6 respectively.

Using these directions, equations (1.48) and (1.49) can therefore be expressed in matrix form as;

$$
\begin{bmatrix} S_1 \\ S_2 \\ S_3 \\ S_4 \\ S_5 \\ S_6 \end{bmatrix} = \begin{bmatrix} S_{11}^E & S_{12}^E & S_{13}^E & S_{14}^E & S_{15}^E & S_{16}^E \\ S_{21}^E & S_{22}^E & S_{23}^E & S_{24}^E & S_{25}^E & S_{26}^E \\ S_{31}^E & S_{32}^E & S_{33}^E & S_{34}^E & S_{35}^E & S_{36}^E \\ S_{41}^E & S_{42}^E & S_{43}^E & S_{44}^E & S_{45}^E & S_{46}^E \\ S_{51}^E & S_{52}^E & S_{53}^E & S_{54}^E & S_{55}^E & S_{56}^E \\ S_{61}^E & S_{62}^E & S_{63}^E & S_{64}^E & S_{65}^E & S_{66}^E \end{bmatrix} \begin{bmatrix} T_1 \\ T_2 \\ T_3 \\ T_4 \\ T_5 \\ T_6 \end{bmatrix} + \begin{bmatrix} d_{11} & d_{12} & d_{13} \\ d_{21} & d_{22} & d_{23} \\ d_{31} & d_{32} & d_{33} \\ d_{41} & d_{42} & d_{43} \\ d_{51} & d_{52} & d_{53} \\ d_{61} & d_{62} & d_{63} \end{bmatrix} \begin{bmatrix} E_1 \\ E_2 \\ E_3 \end{bmatrix} \tag{1.48}
$$

$$
\begin{bmatrix} D_1 \\ D_2 \\ D_3 \end{bmatrix} = \begin{bmatrix} d_{11} & d_{12} & d_{13} & d_{14} & d_{15} & d_{16} \\ d_{21} & d_{22} & d_{23} & d_{24} & d_{25} & d_{26} \\ d_{31} & d_{32} & d_{33} & d_{34} & d_{35} & d_{36} \end{bmatrix} \begin{bmatrix} T_1 \\ T_2 \\ T_3 \\ T_4 \\ T_5 \\ T_6 \end{bmatrix} + \begin{bmatrix} \varepsilon_{11}^T & \varepsilon_{12}^T & \varepsilon_{13}^T \\ \varepsilon_{21}^T & \varepsilon_{22}^T & \varepsilon_{23}^T \\ \varepsilon_{31}^T & \varepsilon_{32}^T & \varepsilon_{33}^T \end{bmatrix} \begin{bmatrix} E_1 \\ E_2 \\ E_3 \end{bmatrix} \tag{1.49}
$$

A third rank tensor can be used to express the charge density produced when the film is subjected to mechanical stress. In piezoelectricity the stress applies can be described by a piezoelectric coefficient d_{mn}. Such a third-rank tensor has the components of piezoelectric coefficients d_{mn} which can be displayed in three by six. The subscript *m* stands for the electrical axis occupying the rows of the matrix and takes the values m=1,2 and 3 whereas the subscript n for the mechanical axis forming the columns of the matrix. It takes the values $n = 1, 2, 3,4,5$ and 6 [84]. Therefore, the general third rank tensor showing the piezoelectric coefficients can be expanded in the form;

$$Pz_{mn} = \begin{bmatrix} d_{11} & d_{12} & d_{13} & d_{14} & d_{15} & d_{16} \\ d_{21} & d_{22} & d_{23} & d_{24} & d_{25} & d_{26} \\ d_{31} & d_{32} & d_{33} & d_{34} & d_{35} & d_{36} \end{bmatrix} \tag{1.50}$$

Cellulose has been identified to possess piezoelectric property. Its piezoelectric tensor d_{mn} can be obtained its symmetrical structure [85]. Specifically, cellulose has a monoclinic symmetry with space group of $C_2 \parallel$ x3. Its piezoelectric third rank tensor therefore can be represented as;

$$Pz_{mn} = \begin{bmatrix} 0 & 0 & 0 & d_{14} & d_{15} & 0 \\ 0 & 0 & 0 & d_{24} & d_{25} & 0 \\ d_{31} & d_{32} & d_{33} & 0 & 0 & d_{36} \end{bmatrix} \tag{1.51}$$

Equation 1.53 is only valid for just one cellulose crystal. For the case of a combination of randomly aligned crystals such as Cellulose Nanofiber film, the net piezoelectric stimulus is derived from the combination of the different individual coefficients. For instance, wood has been confirmed to have a highly reduced effective piezoelectric tensor [85];

$$Pz_{mn} = \begin{bmatrix} 0 & 0 & 0 & d_{14} & 0 & 0 \\ 0 & 0 & 0 & 0 & d_{25} & 0 \\ 0 & 0 & 0 & 0 & 0 & 0 \end{bmatrix} \tag{1.52}$$

$$\text{Where } d_{14} = -d_{25}$$

1.1.9.2. Fabrication of Piezoelectric Sensors from CNCs

Cellulose nanocrystals have been used to fabricate piezoelectric sensory devices. The sensors are simply fabricated by placing two electrodes, one on the upper surface and the other on the lower surfaces of a CNC film. In one of the studies [86], the electrodes were fabricated on polyethylene terephthalate substrate that was 1.25×10^{-6} m thick. A very thin layer of copper, in the order of 100nm, was evaporated using a shadow mask. This was to ensure that the fabricated electrodes acquire the desired pattern. Finally, the CNC film was sandwiched in between the two electrodes, as schematically illustrated in **Figure 1.14**.
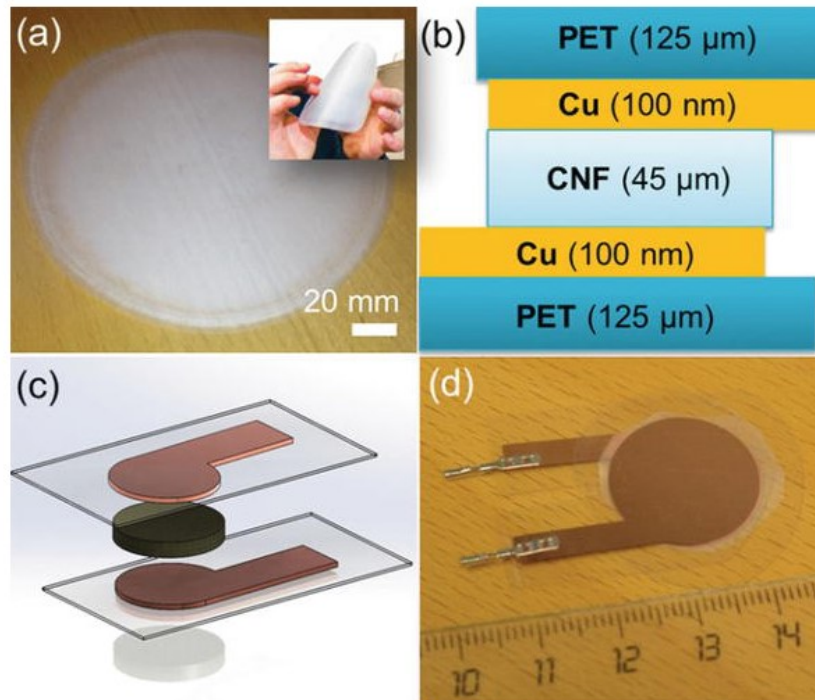
Figure 1. 14: (a) Schematics of a fabricated stand-alone Cellulose Nanofibers film. The insert shows its mechanical flexibility (b) Cross sectional area view (c) aerial view and (d) the assembled sensor, adapted from [86]

1.2 Statement of the Problem

The sustainability, structural, morphological and crystallinity of cellulose nanocrystals have made them become very attractive in the construction and manufacture of passive and active electronic devices. Several applications of nanocellulose crystals have been made in diverse sectors such as pharmaceuticals, energy, aesthetics, and adhesives. Recently, attention has been drawn on the piezoelectric behavior of cellulose nanocrystals. However, the way in which the degree of alignment of the CNCs affects the piezoelectricity of these CNCs have not been investigated. The most common sources of Cellulose are wood and plants. The most basic plant sources of cellulose used to extract CNCs are banana richis, rice husks and the like. Interestingly, water hyacinth which in record has posed the worst environmental nuisances in the water basins, is an excellent source of cellulose. The water hyacinth-base cellulose nanomaterials still, have not been subjected to various characterization techniques. The water hyacinth, especially from

the fresh waters of Lake Victoria has little been used as a source of Cellulose nanocrystals for piezoelectric behavior investigations, leave alone for the full investigation of the various properties through characterization techniques. Thus, the interest of this study was to extract cellulose from the fresh waters of Lake Victoria and prepare cellulose nanocrystals that would eventually be subjected to the vast characterization techniques available enabling us to study their structural, morphological, optical absorption, mechanical and electrical properties among others. The characterized water hyacinth-based CNC films were eventually used to investigate the correlation between their degree of orientation and their piezoelectric behavior. From the correlation result, the final focus was on the design, construction and implementation of a highly sensitive, reliable and high precision laboratory based piezoelectric sensor. The success and commercialization of this study will eventually boost the electronic sector as well as aid in the conservation of the water basin environments.

1.3 Objectives of the Study

1.3.1 Main Objective

The main objective of this is to investigate the correlation between the degree of alignment and opto-piezoelectric effect of cellulose nanocrystals fabricated from water hyacinth.

1.3.2 Specific Objectives

The specific objectives of this study are:

(i)   To extract cellulose nanocrystals from water hyacinth obtained from the Kenyan shores of Lake Victoria

(ii)   To perform UV-Vis spectroscopy on the CNCs thin films

(iii)   To perform Fluorescence spectroscopy on the CNCs thin films

(iv)   To design and fabricate a piezoelectric sensor from the characterized CNCs

(v)   To perform the pressure sensitivity measurements of the fabricated sensors made of films with varying degree of crystallinity.

1.4 Justification of the Study

There is need to increase the utility of cellulose nanomaterials in the manufacture of the electronic and sensory appliances. There is even urgent need to conserve the water basin environment by mass harvesting of the water hyacinth and putting it in good use. These two factors jointly call for the urgent need to research in the best way to utilize the water hyacinth in the production of the much-needed nanocellulose materials necessary for the fabrication of piezoelectricity. This study therefore aims at designing and fabricating piezoelectric sensors made from best aligned and characterized CNCs sourced from water hyacinth from Lake Victoria basin.

1.5 Significance of the Study

Through the study a novel electronic device, the piezoelectric sensor, which is very key in surface sensory measurement was unveiled. This study is therefore key in boosting the manufacturing industry in the electronic sector. The piezoelectric sensor fabricated is useful in a host of applications including weight measurement, pressure measurements on surfaces, surface sensitivity measurements among others. The study is equally important as it is geared towards conserving the water basins through elimination of the water hyacinth weed which is a great nuisance in our water bodies

1.6 Scope of the Study

The scope of the study has basically involved the extraction of cellulose nanocrystals from water hyacinth harvested from the Kenyan shores of Lake Victoria, Usenge beach, Siaya County followed by the extraction of CNCs which were then deposited using drop casting techniques to form thin layer films with varying degrees of linearity of crystals which and later subjected to various characterization techniques. The characterized films were eventually used to design and fabricate a piezoelectric sensor and the study eventually concluded by performing pressure sensitivity measurements on the fabricated sensors.

1.7 Limitations of the Study

Due to lack of appropriate equipment required for high level characterization, the study did not involve some high-level characterization techniques such as water and air adsorption properties of the CNC films. The study has focused only in the use of water hyacinth as our main source material for the nanocellulose. It did not resort to any other alternative source of cellulose.

CHAPTER TWO

LITERATURE REVIEW

2.1 Introduction

Several scientific research works have been conducted in the utility of cellulose nanoparticles in several applications. The applications range both in the energy production and storage field and in the manufacture of electronic and display devices. In the existing literature, a lot has been studied about the sources, structure, extraction procedures, characterization techniques and general applications of Cellulose nanoparticles. In this section, a review is given on what exists in the literature about the sources of CNCs, extraction methods, characterization techniques, the piezoelectric properties and sensory applications of CNCs films.

2.2 Sources of Cellulose Nanocrystals

As mentioned earlier in chapter one, plants and wood are the abundant source of cellulose. Other sources of cellulose include algae, bacteria and tunicates. In higher plants, cellulose remains the major structural component at both the primary and secondary cell layers [87]. Its synthesis occurs within the membrane of the plasma by the use of rosette cellulose synthesizing tools that contain 18-24 cellulose synthase [88, 89]. The resultant product of the synthesis process is distinct microfibrils generally known as elementary fibrils. These rudimentary (elementary) fibrils comprise of 1824 cellulose chains having radius of close to 1.5 nm [88, 89]. The microfibrils are tethered together by hemicellulose to microfibril bundles and the resulting hierarchical structure is surrounded by lignin and hemicellulose [90]. The cellulose is hierarchical as borne from the plant wall. The hierarchy is schematically shown in **Figure 2.1**. There exist strong interactions between cellulose, lignin and hemicellulose making mechanical pulping and chemical treatment of wood to yield a combination of these three elements [91]. In **Figure 2.1**, the inset shows the cellulose chains in the molecular level. From the figure, it is clear that the monomer units are made up of two broad groups. The first unit is the equatorial hydrophilic hydroxyl groups while the second unit is the axial hydrophobic methanetryl groups.

Figure 2.1 schematically shows that the bundles of microfibrils are the chief components in the plants cell layers.
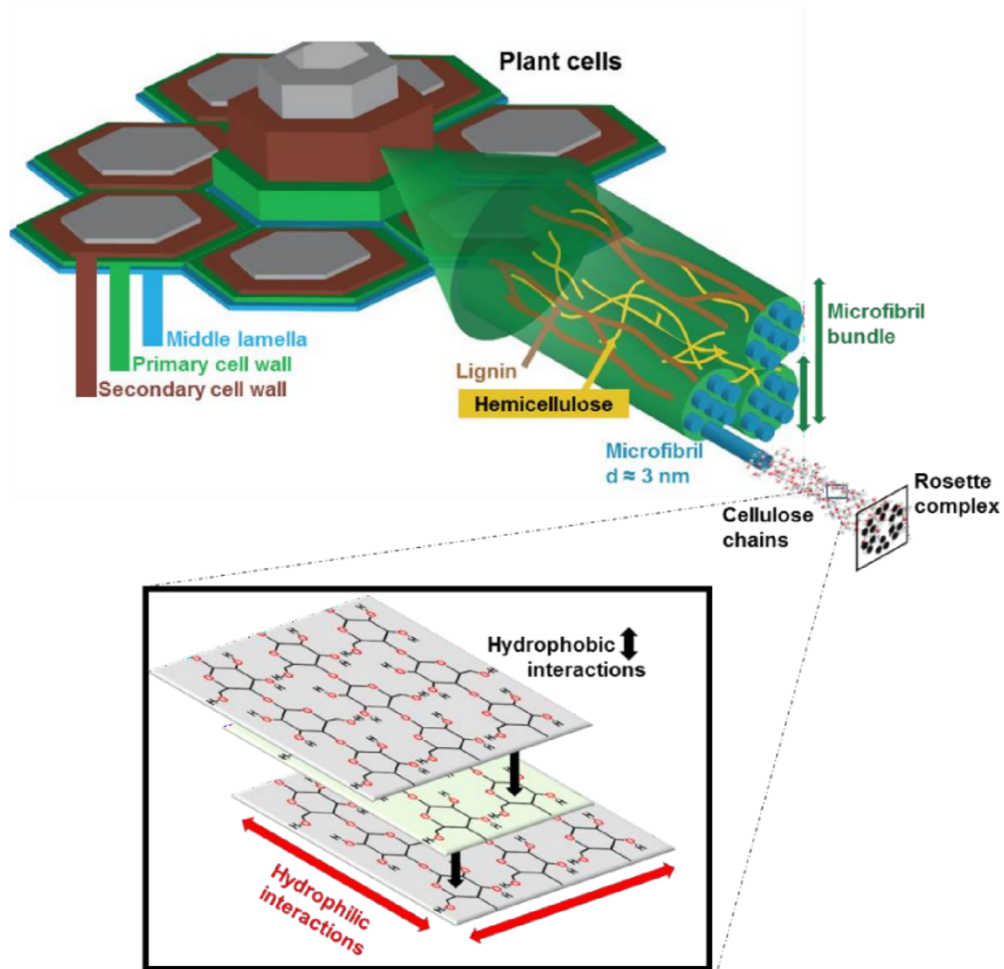
Figure 2. 1: Bundles of the Microfibrils in the plants cell layers. The inset show-cases the interchain and intrachain structure of the hydrogen bonds originating from hydrophobic and hydrophilic interactions [92]

A highlight of some of the existing literature on the work done so far in the extraction of cellulose from plant sources and subsequent applications is hereby unveiled. Globally, wood remains the most abundant source of cellulose. The cellulose component of wood is

approximately 40% [93]. The Technological Association of the Paper and Pulp Industry, abbreviated as (TAPPI), has managed to produce Cellulose Nanomaterials from wood in large scale for several decades [94]. In the world over, TAPPI remains the largest producer of pulp and paper. Their general extraction process of CNs from wood begins with the elimination of the hemicellulose, lignin and other impurities from a pure wood material. This is followed by bleaching and finally dissolving the pulp to produce cellulosic products like Rayon [94]. Apart from wood, live plants also make another attractive source of cellulose. Most plant materials, both aquatic and non-aquatic, have been used to extract CNCs. In their work, Elazzouzi-Hafraoui and his workmates, successfully used cotton to extract CNCs [95]. Sisal has also been used as a real source of CNCs as depicted by Rodriguez and colleagues [96]. Some other plants that are rich in cellulose and have been exploited in the extraction of cellulose are straws of wheat [97], tubers of potato [98], pulp of sugarcane [99], stocks of soybean [100] and banana peels among others. In the aquatic plants field, water hyacinth has been also exploited for CNC extraction though in a limited scale. In their work, Titik successfully extracted cellulose from tropical water hyacinth for membrane preparation that could be used for water purification applications [19]. Due to limited exploitation of the water hyacinth for cellulose production, the study focused on the extraction of cellulose from water hyacinth from Lake Victoria.

Besides the wood and plants, tunicates have also been exploited to extract cellulose. Tunicates are sea creatures with mantles. In the mantle, there exists microfibrils of cellulose that are attached in a matrix of protein. Some of the most common species of tunicates that have been used to extract cellulose are Halocynthiaroretzi and Halocynthiapapillosa [18]. S. Iwamoto *et al* also managed to exploit the Halocynthiapapillosa species of tunicates to extract cellulose [101]. However, tunicates have not remained attractive source since they are difficult to harvest from the deep sea. Another important source of cellulose is algae. Algea produce CMFs within their cell walls. Green algae have been commonly used to extract cellulose nanofibrils. Some of the most frequently used species of green algae used to extract cellulose nanofibrils include Micrasteriasdenticulate [18], Micrasteriasrotate [18], Valonia [102]. Algae have posed a serious setback as a source of cellulose. Algae has proved to be very delicate in the culturing stage hence have not been used to extract cellulose to a commercial stage. Besides the algae, bacteria have also been used to extract cellulose to some limited scale. Gluconacetobacterxylinus is a species

of bacteria that produces cellulose and has remained the focus of research [17]. Cellulose is extracted from bacteria by culturing process. When bacteria are cultured under special culturing conditions, it secretes cellulose microfibrils. At the secretion stage, they end up producing thick gel that consists of cellulose microfibrils and water [103]. The CMFs can therefore be extracted at this stage. Just like algae, bacteria culturing is a tedious and slow process. This has therefore made bacteria not become an attractive source of cellulose. It is therefore evident that wood as a source is not popular due to the tedious extraction process since wood is hard to crush. Biomass as a source equally offers a challenge since the yield is very low and cleaning process must be very thorough. The remaining sources; algae, bacteria and tunicates are not only scarce but also produce very low yield and takes very long process. This justifies the source of water hyacinth which is abundant, easy to crush and has very high cellulosic content.

In the study, the aquatic plant, water hyacinth, *(Eichhorniacrassipes),* from Lake Victoria, has been used as our source of the cellulose nanomaterials. This abundant aquatic weed species, poses a great challenge in open water masses. It hampers irrigation, generation of power, boating, navigation and fishing in the infested water body surface. To minimize these challenges, the study resorted to reduce the population of the weed by physical harvesting for its utility in this noble electronic application. From available literature, water hyacinth is very rich in composition in cellulose compared to other major plant sources as depicted in **Table 2.1.** This heavily justifies the choice of the source of cellulose to be the water hyacinth. Due to its huge abundance and high cellulosic concentration, desired amounts of cellulose nanocrystals were extracted and subjected to further characterization and eventual application in the piezoelectricity and sensory measurements. This will not only boost the electronic industry but also conserve the environment.

Table 2. 1: Comparison of percentage composition of the three major components of various fibers

Fiber	Cellulose	Hemicellulose	Lignin	Reference
Water hyacinth	60	23.7	13	[104]
Grass	45	31.4	12	[105]
Hardwood stem	40-45	24-40	18-25	[106]
Barley straw	33-40	20-30	8-17	[105]
Pineapple leaf	34-40	21-25	25-29	[107]
Bagasse	45	30	20-22	[108]
Wheat straw	30	50	15	[105]

2.3 Extraction of Cellulose Nanocrystals

As was mentioned in chapter one, CNCs extraction from the source materials is a two-stage process. It involves the purification and homogenization pretreatment process followed by hydrolysis process. The pretreatment stage exposes the internal parts of the source material to become more reactive in the subsequent extraction processes. The second procedure, the hydrolysis process, eliminates the amorphous regions leaving behind the pure crystalline parts. Previous studies have reviewed vast mechanisms of the hydrolysis process, majorly focusing on mechanical hydrolysis, chemical hydrolysis and enzymatic hydrolysis [109,110]. The approach used will pose great impact on the morphology and other physical and chemical characteristics of the produced cellulose nanoparticles. A brief review of these main mechanisms is presented. Several processes have been utilized in the mechanical approach to realize cellulose nanofibrils from different cellulose-laden materials. These mechanical hydrolysis processes include high-pressure homogenization [103] use of grain grinders and refiners [111], cryocrushing mechanism [112] and very intense ultrasonic treatments [113]. All these mechanical processes cause measurable shear effect on the source material. The shear effect creates transverse cleavage that is parallel to and overlaps on the axis of the structure of the cellulose microfibrils. This finally

leads to the production of longer cellulose fibrils which are generally called microfibrillated cellulose (MFC). Turbak with his colleagues [35] as well as Herrick with co-workers [34] were the first successful achievers in extraction of CNCs using mechanical treatment. The two research groups managed to produce cellulose fibrils at nanoscale. Their source material was softwood pulps. In their work, they typically subjected the source materials into mechanical treatment repeatedly. As the mechanical treatment is repeated, the yielded particles get smaller and become more uniform in radius. However, they become more mechanically damaged leading to poor crystallinity. Thus, one of the greatest limitations of mechanical extraction process is the reduced crystallinity percentage of the yielded nanofibrils [111]. Another limitation of mechanical treatment worth noting is the fact that it must be crowned by a chemical treatment. Subjecting the mechanically prepared nanofibrils into chemical treatment not only completely eliminates the amorphous component leaving highly synthesized crystalline component but also functionalizes the particle surface.

The second approach is the acid hydrolysis which has remained the most common approach of CNC extraction from many cellulose sources. Acid hydrolysis process basically eliminates the amorphous regions existing in the microfibrils structure. It has chiefly been used in the extraction of bio-based fibrillated cellulose [113]. This chemical process of acid hydrolysis is executed in the following major steps: the source material obtained from the pretreatment stage is added to an acid whose concentration is already prepared; The acid is then left to react with the material for some given time and at a controlled temperature; The syrup formed is then diluted with distilled water so that the reaction of cellulose with the acid can seize; This is followed by series of separation procedures achieved by centrifugation and washing steps. Finally, dialysis is done against distilled water in order to fully eliminate any remaining acid and salt. From the available literature, several studies are cited as having successfully extracted cellulose nanocrystals using acid hydrolysis processes. For instance, in 1947 Nickerson and Habrle were the first to prepare CNC by the acid hydrolysis method. They hydrolyzed the cellulose source material using hydrochloric and sulfuric acids separately [114]. Later In 1951, Ranby registered a breakthrough in synthesizing CNCs from acid hydrolysis process. He used wood fiber to produce very stable Cellulose nanocrystals colloidal suspensions using concentrated sulfuric acid [115]. In acid

hydrolysis, the most commonly used mineral acids are H_2SO_4 [116], HCl [117], H_3PO_4 [118], HBr [119], and the acids obtained from their mixtures [120]. However, Sulphuric and hydrochloric acids have some inherent advantages over the rest and remain the most preferred acids for acid hydrolysis. For instance, Sulphuric acid leaves the particles with negative surface charges thereby producing very stable suspensions of cellulose nanocrystals. Just like in mechanical treatment, acid hydrolysis has its own limitations of equal measure. For instance, with little control of the hydrolysis parameters, acid hydrolysis can lead to highly degraded CNCs. Further, the production cost is at its peak following high corrosion rate of the apparatus involved. It also poses a great threat to the environmental health since great quantities of chemical waste and other pollutants are produced. In the study, the increase in the yield of CNCs was achieved by reducing the acid concentration while elongating the reaction time span.

The other extraction method to be mentioned is the Enzymatic Hydrolysis which involves use of the Cellulase enzyme to extract CNCs from the source material. The cellulase is a multicomponent enzyme system with three major components. The first component is the endoglucanases (EG), the second component is the cellobiohydrolases (CBH). The third component is the β-glucosidase (GB). Each of these components have their unique roles in the hydrolysis process. EG majorly react with the amorphous region with the major goal of breaking the 1-to-4-Betta glycosidic bonds of cellulose. CBH on the other hand react with the extreme ends of linear cellulose molecules in order to break the crystalline area. The last component, β-glucosidase has a major role of converting cellulose into glucose through hydrolysis process [121]. Several scientists have successfully extracted CNCs using the enzymatic hydrolysis procedure. For instance, Filson and coworkers made use of endoglucanase to successfully prepare CNCs from recycled wood pulp [122]. Enzymatic hydrolysis equally has its share of limitations; it poses harsh experimental conditions, produces very low yield and the process takes longer time to be fully accomplished. However, one of the outstanding advantages of enzymatic hydrolysis is that the process is environment friendly. It is therefore the interest of this study to use mineral acid hydrolysis as it is more convenient, abundant, yields higher crystallinity with high yield of the extracted CNCs. **Figure 2.2** gives the illustration of the CNC extraction processes using the two broad processes, the acid hydrolysis method and the mechanical

treatment method. As can be observed from the diagram, the acid hydrolysis generally produces finer CNCs having shorter dimensions in diameter and length compared to the mechanically produced coarse CNFs with much longer dimensions in diameter and length [123].
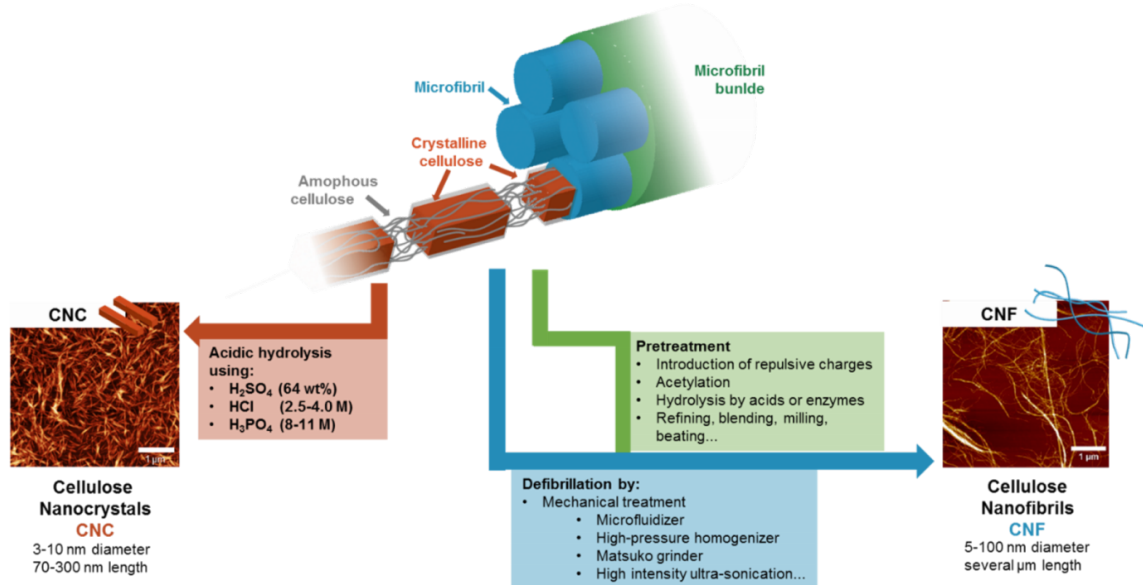
Figure 2. 2: The schematics of CNC extraction processes using the two broad processes, the acid hydrolysis method and the mechanical treatment method (123)

2.4 Characterization Techniques for the CNCs

2.4.1 Introduction

Several techniques of characterization have been performed on cellulose nanomaterials obtained from different source materials. These techniques have greatly supported the study of several properties of materials like structural, morphological, optical absorption and optical photoluminescence, electrical, thermal and mechanical among others. However, not all these techniques mentioned have been performed on Cellulose nanomaterials obtained from water hyacinth. In this section, the review of some characteristic techniques that have been so far performed on CNMs obtained from water hyacinth is presented.

2.4.2 Fourier Transform Infrared Spectroscopy (FTIR) Analysis of CNCs

FTIR spectroscopy is a technique that uses the beam of infrared radiations to identify functional groups in materials. Several studies have been conducted in characterization using FTIR. Meriko Enweku is one of the first scientists who conducted a research experiment to examine the characteristic peaks for cellulose sourced from hyacinth harvested from raw water. He examined the peaks in the range of $3.5x10^3$ to $3.0x10^3$ cm^{-1} [124]. Their results showed that the peaks correspond to the expansion zones of the functional groups of -OH caused by the interactions between hydrogen bond and the hydroxyl groups as explained by Asrofi M. *et al* and Abraham E. *et al* [125, 126]. **Figure 2.3** shows the spectra obtained from Fourier Transform Infrared spectroscopy for water hyacinth in raw form and that of cellulose sourced from it. From the diagram, we observe that the characteristic peaks due to the stretched C-H functional group appear in the wavenumbers ranging from $3.0x10^3$ to $2.8x10^3$ cm^{-1} a sign that the two samples possess aliphatic saturated particles [127]. There is a stark difference in the spectra at $1.735x10^3$. The fiber, in its crude form, has a peak at this wavenumber while the purely extracted cellulose has no peak. This is a clear indicator that the raw water hyacinth is still laden with hemicellulose and lignin possessing the acetyl and uronic ester web of carboxylic group of the ferulic and p-coumaric acids that cause the peak [128,129]. Pure extracted cellulose lacks these bonds after excessive removal of lignin and hemicellulose after effective acid hydrolysis. This peak was not observed in the chemically treated cellulose extract, signifying that the lignin and hemicellulose were fully eliminated. Similarly, the presence of adsorbed water due hemicellulose contained in the raw water hyacinth caused a peak to occur at $1.639x10^3$ cm^{-1} This peak was not observed in the pure extracted cellulose due to lack of hemicellulose. Lignin contains aromatic rings that are ever in vibration. These vibrations are the source of the spectral peaks in the crude hyacinth spectrum observed $1.248x10^3$ cm^{-1} which is distinctly lacking in the pure cellulose spectrum. This too is an indicator that pure cellulose is lignin-free [130]. However, the two samples showed characteristic common peaks at 1.426 cm^{-1}. The raw water hyacinth and cellulose extract displayed outstanding peaks at $1.426x10^3$ cm^{-1} because both experience plane bending of the CH_2 functional group [131].

51
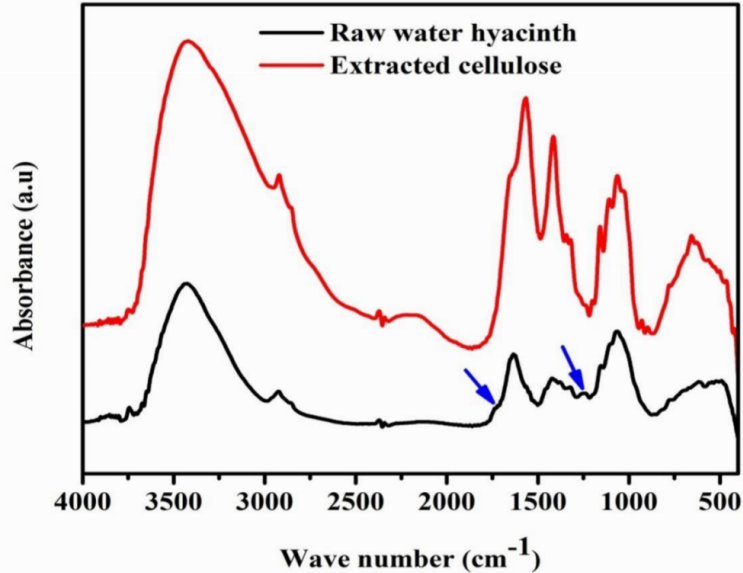
Figure 2. 3: Characteristic spectral peaks for water hyacinth in raw form and pure cellulose as obtained from FTIR spectroscopy [124]

Another research study that involved subjecting water hyacinth cellulose into FTIR spectroscopy was conducted by Setyaningsih and workmates [132]. They extracted cellulose using different solvents. They then identified and compared the functional groups of cellulose extracted using the various solvents. They observed that the spectra of extracted cellulose samples containing solvents of H_2O_2 showed peak absorbance in the wavenumbers of 3.44765×10^3 cm^{-1} and 2.90137×10^3 cm^{-1}, a phenomenon they attributed to the vibrations caused by the extension of –OH and C-H functional groups. Further, their analysis revealed that pure extracted cellulose spectra depicted more intense bands at 1161.5 cm^{-1} and 1112.88 cm^{-1}, an observation missing in the raw water hyacinth spectra. Interestingly, similar observation was reported in cellulose extracted from oat and rise husks, in an experiment undertaken by Oliveira [133]. In yet another FTIR spectroscopy, Halal [134], observed intense bands occurring at 161.5 cm^{-1} and 1319.44 cm^{-1}. He reasoned that the two band intensities were indications of C_3-carbon and glycosidic C-O-C bond vibrations respectively. It was also shown that functional groups of cellulose constituent

components were also present. This was seen in the occurrence of bands at 1060.7 cm^{-1} and 893.79 cm^{-1} attributed to vibrations of C-O and C-H due to stretching.[135].

In their study, Titik and coworkers, managed to isolate cellulose from water hyacinth and further prepared membranes from the extracts by phase separation methods [19]. The resultant membranes were subjected to FTIR measurements where their water surface chemistry and water flux were metered. One of their key revelations was that water flux magnitude was inversely proportional to time of evaporation, i.e, when the evaporation time is increased, then water flux reduces. Scientifically, when evaporation occurs for a longer time, the pore size of the membrane reduces following increased polymer concentration at the topmost sheet of the membrane. In all these FTIR measurements done the samples subjected to measurements were not prepared under parametrized acid hydrolysis process. There was no attempt to investigate the impact of time, temperature and acid concentrations on the FTIR measurements obtained.

2.4.3 Thermal Analysis of CNCs

Thermal analysis of materials is performed by a thermogravimetric analyzer (TGA). The tool helps in analyzing thermal stability of a cellulose-laden fiber sample. Two separate research studies have been cited as having conducted thermal analysis on the thermal properties of cellulose obtained from water hyacinth. In their research work, Titik *et al*, managed to isolate cellulose from water hyacinth and further prepared membranes from the extracts [19]. In their thermal analysis procedure, they took about 6g of dried water hyacinth sample and pyrolyzed the sample by a TGA. Their TGA results indicated that hemicellulose and lignin are decomposed at different temperature ranges. They decompose at 200-350°C and at 350−470°C respectively. It further revealed that hemicellulose gets fully digested at 265°C. A peak on the spectrum was also observed at 326°C, a clear indicator of the cellulose degradation point. In another research study, Fang and his research fellows investigated the thermal properties of raw recycled sheets of paper and recycled paper reinforced with cellulose nanofibers using TGA [4]. One of their findings was that all samples lost mass when the treatment temperature approached 90°C, an indicator that water evaporation occurred from the surfaces of the sheets. Their further analysis was focused on the comparison of thermal stability of the prepared samples at distinct temperatures

and corresponding mass losses. They learnt that the raw recycled paper lost mass by 10% at a temperature of 190°C. However, with the inclusion of the CNFs into the matrix, the 10% mass loss was registered at a higher temperature of 200°C. Their general conclusion was thus, the thermal stability of recycled papers is highly enhanced by the addition of CNFs. The thermal stability of the RP/CNF composites is directly proportional to the CNFs content. The graphs in **Figure 2.4** show the TGA and DTGA spectra of raw recycled paper and recycled paper cum CNFs composite sheets having varied contents of CNFs. As can be seen, the graphs in figure 2.4b, clearly illustrate that for the RP/CNF composite sheets, the degradation rate is higher for CNF content of 5, 10 and 15% but lower for the lower CNF percentage compositions. This can be attributed to the hydrogen bonds created between the CNFs and the RP structure which really improves thermal degradation temperature. The increased CNF content in the composite drastically increases the strength of the hydrogen bonds thereby increasing thermal stability.
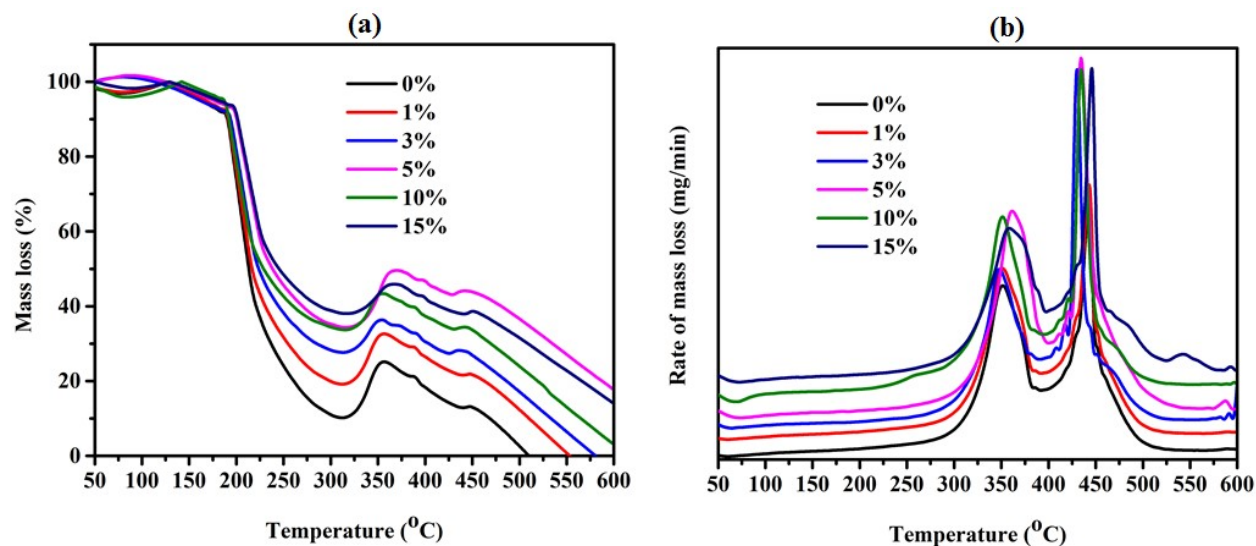
Figure 2. 4: Schematics of the TGA (a) and DTGA (b) graphs for the RP/CNFs composite sheets of paper with different percentage composition of the reinforcing CNFs [4]

From the above literature, Turbak *et al* did not make any attempt to investigate how degree of alignment of the prepared samples influence their thermal properties.

54

2.4.4 Optical Properties of CNFs

In a study carried out by Turbak and coworkers [135], optical property measurements were done on CNFs prepared from rice husks. In particular, transmittance measurements showed that optical transmittance CNFs dispersion is highly influenced by thickness of the fibers and their ability to disperse in water. In yet another study conducted by Meriko Ewnetu [124], Optical transparency of raw water hyacinth was compared to that of cellulose extracted from them. As can be seen in the graph of **Figure 2.5**, the transparency peaks are 2.007 % at 800 nm and 17.71 % at 608 nm for raw water hyacinth and cellulose respectively. They further learnt that CNFs dispersions exhibited higher transparency at longer wavelengths. In particular optical transparency for CNF dispersions was 65 % at 800 nm. This is an indicator that CNFs are indeed in the nanoscale and their sizes are much smaller relative to the wavelength of visible light used in the spectroscopy as compared to the sizes of raw water hyacinth and the cellulose extracted from them. Thus, optical transparency of a material increases with decrease in its size. The shape of a material and its size greatly influence its optical transparency. For a larger material with rough surface, less transmittance will be observed since more light scattering and absorption takes place in the extended rough surface leaving little light to be transmitted. This explains why the raw water hyacinth and cellulose have lower optical transmittance compared to the CNFs.
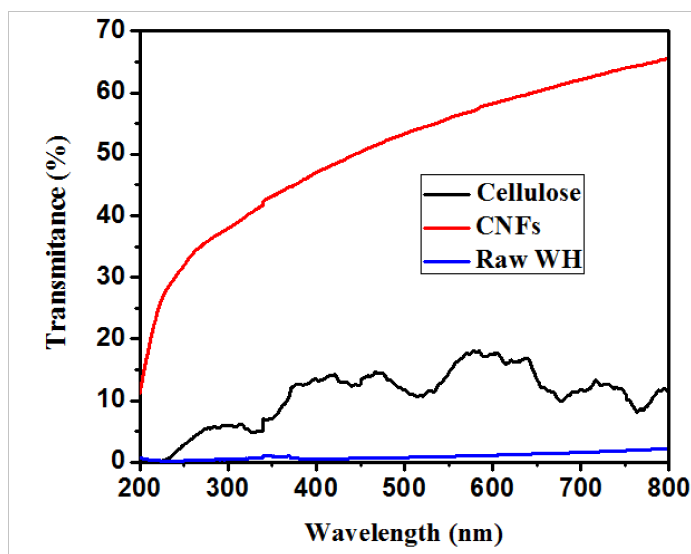
Figure 2. 5: The Ultraviolet-Visible light Optical Transmittance of one-percent by weight dispersion of raw water hyacinth WH, Cellulose and Cellulose Nanofibres [135-137]

In the optical measurement presented by Turbak and coworkers above, the samples were not subjected to acid hydrolysis. Only pretreatment and mechanical hydrolysis was done to realize cellulose and CNF respectively. The mechanical hydrolysis was equally not parametrized as per time, temperature and strain magnitude. The procedure did not proceed to obtain the optical measurements like optical band gap energy, the *Tauc* energy among others.

2.4.5 Mechanical Properties of CNCs

In yet another paper [138], tensile resistance was measured using a tensile machine. Various nanocomposites having various measured nanocellulose fibers compositions were prepared. The tensile machine could measure and display the ratio of the force applied and the surface area of each sample. This was expressed in KPa, a unit of pressure. Percentage elongation was equally measured by the machine. This was calculated as the ratio of extension of the composite to the initial length of the sample and expressed in percentage. The results were tabulated as shown in **Table 2.2**.

Table 2. 2: Tensile measurements data as obtained from Tensile machine.

Parameters	CNFs content in the composite sheets (wt. %)					
	0	1	3	5	10	15
Thickness (mm)	1.27	1.09	0.98	0.96	0.88	0.8
Elongation (%)	2.01	2.05	2.24	2.92	5.18	2.95
Tensile strength (KPa)	29.8	45.6	53.5	63.1	69	80.4
Young's modulus (KPa)	14.8	22.3	23.9	21.6	13.3	27.2
Density (g/m^3)	16.9	20.3	23.3	24.5	27.8	33

From the data presented in **Table 2.2**, there is an overwhelming advantage of adding CNFs in the composite sheets. CNFs increase the interactions between the fibers of cellulose and the fibers of the recycled paper thereby promoting a better realignment. This makes the pores between the fibers get fully filled during the production process. Thus, more uniform, highly compact and dense structures of the composite paper sheets are produced. The mechanical properties of the resultant composite are consequently increased through increased density and reduced porosity. The greater surface area of contact between the neighboring cellulose fibers gives an increased population of hydrogen bridge bonds resulting to a denser structure eventually yielding the composite sheets which are stronger and stiffer. The data further reveals that the percentage elongation of the composite increases up to 10% composition of CNFs but drastically reduces at 15% content. This is an indicator that when the percentage composition of cellulose surpasses 10% then produced composites become stiffer and harder increasing their brittleness. Another information that is clear from **Table 2.2** is that the tensile strength of the composite sheet is directly proportional to the CNFs contents. This is attributed to the fact that percolation occurs between the Recycled paper network and the Cellulose nanofibers through hydrogen bonding. This enhances the creation of rigid interconnected matrix that is able to resist the tensile process. Finally, a staggered change in the Young's modulus is recorded. It increases in the range of 0 to 3% then reduces in the range of 5 to 10% before increasing again in the range of 10 to 15%. The initial increment is due to the transfer of stress the recycled paper which is in disordered structure to relatively ordered and stiffer CNFs. Similarly, significant increase in fracture strain values can also be said to be responsible for the decrease in Young's modulus in the 5 to 10% range. The final increase observed at higher percentage composition can be attributed to the drastic reduction in the percentage elongation at the high percentage content of the CNFs.

From the review done so far and from the available literature, little work has been done in characterization techniques of cellulose nanomaterials sourced from water hyacinth. No recorded work has investigated morphological, optical absorption and optical photoluminescence properties of cellulose nanomaterials sourced from water hyacinth and how their degree of crystallinity impact on these properties. The study has therefore focused on investigation of the correlation of degree of alignment of CNCs obtained from water hyacinth on their optical properties and piezoelectric behavior.

2.5 Piezoelectricity of Cellulose Nanocrystals

2.5.1 Introduction

When a material is subjected to an external mechanical stress, it undergoes change in electrical polarization as it responds to this external pressure. This phenomenon is called Piezoelectricity [139]. Piezoelectric effect is expected to be highly manifested in crystalline nanomaterials including crystalline cellulose nanocrystals (CNC) [54]. Fukada, a renowned scientist, was the first researcher to report the piezoelectric behavior of wood as early as 1955[140]. However, the research in this area has since remained low. The evidence of the piezoelectricity of cellulose nanocrystals has been experimentally reported by few recent studies [140, 141].

2.5.2   Fabrication of Piezoelectric Sensors

In their study, Rajala and coworkers managed to fabricate CNF films sensors and further performed the sensor sensitivity measurements [142]. They successfully extracted CNF material using mechanical homogenizing method. They passed the cellulose source material (bleached birch cellulose mass) in microfibrillator machine repeatedly until CNFs were produced [142]. They used the obtained CNFs to create CNF films. This, they achieved by a 30 minutes long pressure filtering process that was immediately followed by pressing using a presser. The pressed films were finally dried in an in hot-press at 100°C for a period of 2 hours. Using the micrometer screw gauge, they learnt that the yielded films were 70 micrometre thick. They finally embedded the electrodes on the CNF films using polyethylene terephthalate (PET) substrate by e-beam evaporation using Varian vacuum evaporator whereby they evaporated 100 nm thick copper (Cu) sheet through a laser-cut stencil shadow mask.

2.5.3 Sensor Sensitivity Measurements

The sensor sensitivity can be defined as the quantity of charges produced by the sensor per unit normal force exerted on the sensor. A special tool called Brüel & Kjaer Mini-Shaker model 4810 is always applied to conduct sensitivity measurement. This tool generates a dynamic excitation force with a rating of 10N sinusoidal peak. Its frequency ranges from DC to 18000 Hz. For accurate measurements, a sinusoidal input is required in the shaker. Thus, a function generator type Tektronix AFG3101 was used to provide the required sinusoidal input. Referencing was

equally a feature that must be done for correct data to be sourced from the shaker. To achieve this, a very sensitive dynamic force sensor was used to reference the dynamic excitation force. Finally, a load cell was applied as reference sensor to gauge the static force generated at the sample-shaker's piston interface. For mounting purposes to prevent the shaking of the whole setup pretension that produces static force was applied. Sensor sensitivity measurements were equally done in the transverse direction where the sensor horizontally orientated on a metal plate. In one of the attempts, a 3N static force was applied on the sensor surface accompanied with sinusoidal 2 Hz input signal of 1000mV. This resulted to excitation force of about 1.3N. This procedure of sensitivity measurement was repeated thrice. The quantity of charge yielded by the sensor was finally measured. The charge measurement was achieved using a tailor-made combination of amplifier and a 16-bit analogue to digital converter (ADC). The ADC was interfaced with the sensor through coaxial cables and crimp connectors. The data obtained was used to calculate the sensor sensitivity by simply dividing the charge generated on the sensor surface with the dynamic force applied on the sensor. The SI unit of sensor sensitivity is thus Coulombs per unit Newton (C/N). Since the charges produced in this manner are in the pico-scale, the sensor sensitivity is therefore measured in pC/N. Using their data, they found that the sensor sensitivity values for their fabricated piezoelectric sensors was ranging from 5.2 -7.0 pC/N. The sensors therefore showed uniform sensitivity an indicator that cellulose nanofibrils are uniformly spread inside the film. Their results therefore depicted high degree of reliability. However, in their work, they failed to vary the degree of crystallinity so as to obtain the varying values of sensitivity.

In this study, similar sensitivity measurements have been performed on CNC film sensors fabricated from CNCs extracted from water hyacinth but with different crystallinity indices. The degree of polarization of the CNC films were successfully varied which led to varying orientation of crystals of the CNC films leading to remarkable variations of piezoelectricity. Different sensitivity values were recorded from various sensors with varying crystallinity indices. Thus, the study unraveled the correlation between the degree of linearity of CNCs and their piezoelectric properties.

CHAPTER THREE

RESEARCH METHODOLOGY

3.1 Introduction

In this chapter, detailed outline is presented for all the materials and equipment used in this research are outlined, detailed procedures followed in the extraction process of the CNCs, film preparation methods applied, characterization technique used, piezoelectric sensor fabrication method applied, and how the sensitivity measurements were done on the fabricated sensors. It also gives information on the analysis technique used to investigate the correlation between the degree of alignment of the CNCs and the piezoelectric effect of the water hyacinth based fabricated sensors.

3.2 Materials and Equipment

3.2.1 Materials

Most of the chemicals and reagents used in this work were sourced from the JOOUST Teaching and Research Laboratory (JTRL) main campus. These included Hydrochloric acid, sulphuric acid, nitric acid, Sodium Hydroxide, Sodium hypochlorate, toluene and ethanol. All the glassware, Glass vials sample containers, microscope slides, droppers, sieve, filters that were used in the research were also sourced from the lab.

3.2.2 Equipment

Laboratory protective gears as well as sample holders were obtained from Jaramogi Oginga Odinga University Chemistry Research laboratory. The UV-Vis spectroscopy was conducted using the nanodrop spectrometer named Eppendorf Bio-Spectrometer Kinetic Perkin available in Jaramogi Oginga Odinga University Research laboratory. The fluorescence spectroscopy was conducted using F96Pro Fluorescence also available in JTRL. The Light microscope used (LEICA DM 500) used for light microscopy was also available in JTRL characterization

techniques were all available in JTRL. The XRD machine that was used for crystallography was sourced at KIRDI, Kisumu Branch.

3.3 Experimental Procedure

3.3.1 Extraction of Cellulose Nanocrystals from Water Hyacinth

Cellulose Nanocrystals from water hyacinth were extracted through a rigorous process that involved source material collection, cleaning and drying, ball milling, alcohol treatment, alkaline hydrolysis, bleaching and finally categorized acid hydrolysis.

3.3.1.1 Sample Collection, Cleaning and Drying.

Fresh water hyacinth plants were collected from the Kenyan Shores of Lake Victoria in Usenge Beach Imbo Division, Bondo subcounty, Siaya County. Being a gulf, the site was identified as having highly matured healthy water hyacinth. Usenge Beach is shielded from strong direct water waves from the lake hence makes a good breeding site for the weed. We therefore expect to obtain high cellulose content from the hyacinth weed sourced from this site. After collection, the stalks and stems were cut off from the plants and cleaned to get rid of mud, sand, minerals and any other aquatic impurity that could be lying on their surfaces. The cleaned stalks and stems were then chopped into small cubes then fed into an oven where they were dried at 100°C for 30 minutes. The final product after drying appeared as shown in **Figure 3.1.** Water hyacinth melts at 220° C and drying them at 100°C is safe and cellulose that are free of char and with unbroken crystallinity.

Figure 3. 1: Fully dried water hyacinth cubes and chops just before ball milling

3.3.1.2 Sample Crushing and Grinding

The fully dried water hyacinth chops were reduced to half powder form by ball milling using a ball milling machine. The milling machine was set to rotate at 60 rpm for a shorter duration of 5 minutes. This low frequency of rotation and shorter crushing duration was to ensure that the crystalline regions are not broken. The coarsely ground fibers were subjected to sieving using a sieve of hole diameter 1mm to obtain course powder free of chuff. A total of 20g mass of the powder was prepared ready for the cellulose extraction. As was explained earlier the water hyacinth powder obtained consists of cellulose, hemicellulose and lignin. Their percentage compositions in the powder are 25%, 33% and 10% respectively [19]. The lignin and the hemicellulose components must therefore be eliminated in the pretreatment stage and in the subsequent acid hydrolysis process. For the CNC extraction procedure, the study adopted the protocol provided by Titik I. *et al* [19]. This formed the procedure applied in the pretreatment stage and acid hydrolysis process.

3.3.1.3 Pretreatment Stage

The coarse hyacinth powder measuring 10g was measured using an electronic beam balance and transferred into a round bottomed flask containing 150ml homogeneous solution which is a fully stirred mixture of two alcoholic solutions, ethanol and toluene. Ethanol and toluene are mixed in the ratio 1.2. In our study, the ethanol/toluene mixture was made by mixing 50ml of toluene to 100ml of ethanol and then stirred to homogeneity. Toluene/ethanol mixture is one of the best cellulose extracts from a source material. Once dipped into the mixture, the water hyacinth sludge was heated at $70^{\circ}C$ for 2 hours at a constant stirring using the rotor vapor instrument as shown in the set up in **Figure 3.2.**

Figure 3. 2: Rotor-vap set up for the water hyacinth powder soaked in ethanol/toluene mixture being stirred continuously in an ever rotating round bottomed flask while being heated in the rotor bath

This process was done to get rid of extractive components that are in the water hyacinth stalks leaving behind the three major components of the hyacinth powder which are cellulose, hemicellulose and lignin. The resultant product after sieving and thorough washing was brown thick sediment, shown in **Figure 3.3.**

Figure 3. 3: Water hyacinth sediment product after alcohol pretreatment

The sediment was then subjected to a bleaching process using $NaClO_3$ for two hours at 80^oC. This first bleaching process not only increased the whiteness of the cellulose sludge but also led to the elimination of lignin by breaking the ether bonds. The bleached sludge was then subjected to alkaline hydrolysis using NaOH 1% at 60^oC for 2 hrs. This was to ensure that the main chain cellulose is free of hemicellulose. NaOH reaction with the sludge led termination of major bonds

leading to heavy degradation of the molecules of the lignin. The resultant product was further subjected to a second bleaching process using NaClO$_3$ 2% at 75°C for 2hrs to fully eliminate any trace of hemicellulose and lignin that could still be clinging in the product. The final product, shown in **Figure 3.4**, was therefore ready to be subjected to acid hydrolysis so as to obtain the cellulose nanocrystals.

Figure 3. 4: The final product of the extracted CNCs from water hyacinth

3.3.1.4 Acid Hydrolysis

As was explained in chapter 1, the acid hydrolysis is done to get rid of the amorphous region of the pure cellulose material so as to remain with the crystalline region only thereby obtaining cellulose nanocrystals in syrup form. Use of mineral acids was resorted to as they yield CNCs with high crystalline index. The mineral acids used were the H$_2$SO$_4$, HCl and HNO$_3$ for different samples. This would help in investigating the acids which gives the best yield. For each acid used, the degree of concentration was also varied from 5%, 10% and 15%. Further for every acid concentration value of the acid, the hydrolysis heating temperature was equally varied from 50^{0}C, 70^{0}C and 90^{0}C. The heating was done in a water bath set at these three distinct

temperatures. For every hydrolysis temperature, the duration for the hydrolysis process was equally varied from 2hours, 3 hours and 4hours. For instance, **Figure 3.5** shows 6 samples of extracted cellulose undergoing hydrolysis using same acid but of different concentrations being heated in a water bath at a uniform temperature.

Figure 3. 5: Samples of extracted cellulose undergoing hydrolysis using same acid but of different concentrations being heated in a water bath at a uniform temperature

The large cellulose sludge obtained from the pretreatment stage was therefore divided into three equal parts, with each part being subjected to hydrolysis processes using one unique mineral acid. The parts were named Sample A, sample B and sample C. Sample A was treated using H_2SO_4 which was prepared in three different concentrations; H_2SO_4 5%, H_2SO_4 10%, and H_2SO_4 15%. Sample A was therefore further divided into 3 equal parts with each part having its corresponding acid concentration. These three samples were labeled as; H_2SO_4 5%, H_2SO_4 10%, and H_2SO_4 15%. Each of these samples was divided into 9 equal parts to take care of the three parameters named earlier. Sample A therefore yielded 27 samples each subjected to a unique

acid hydrolysis process. The same procedure was applied to sample B and sample C that corresponded to HCl and HNO_3 respectively. A total of 81 samples were prepared and safely kept in labeled sealed glass tubes as shown in **Figure 3.6**.
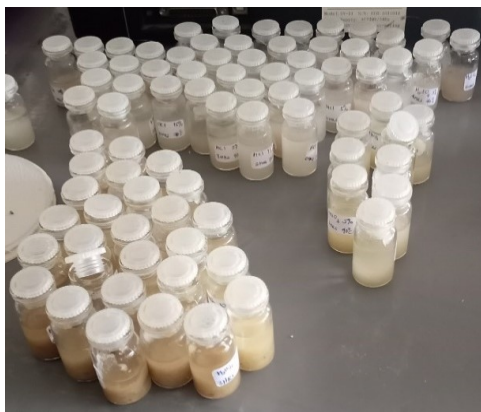
Figure 3. 6: Vials containing cellulose powder prepared by HCl, H_2SO_4 and HNO_3 acid hydrolysis with different concentrations, temperature and hydrolysis time

The essence of parameterizing the process was to enable the research team to investigate how the four hydrolysis parameters affect the degree of crystallinity of the extracted CNCs. These four parameters are namely: the mineral acid used; the concentration of the acid, Temperature of hydrolysis and duration of the hydrolysis process. The samples were given unique acid hydrolysis treatments to help us investigate how change in the above four parameters impact in the characteristics of the obtained CNCs such as surface morphology, crystallinity, Optical band gap, electrical properties and even the mechanical properties.

3.3.2 Thin Films of CNCs

3.3.2.1 Preparation of Thin Layer Films

After the preparation of the desired CNCs from the water hyacinth stalks and stem, the focus the shifted to obtaining CNC thin films. Use of drop casting method was adopted to create the CNC

films of each of the sample made. This was achieved in a two-stage procedure that began with cleaning the glass substrates followed with the deposition of the CNCs to form thin films. The glass slides which are often used in microscopy made good substrates where thin films were deposited. The slides were first thoroughly cleaned using liquid detergent. All the grease and stains of oil were then eliminated from the slides surfaces by dipping them in pure alcohol. This was followed by rigorous rinsing using distilled water. Finally, the clean, sterilized glass slides were dried in an oven at a temperature $100^{o}C$ for another half an hour. Each of the labeled samples of the extract was drop-cast on a clean slide. The slide was then tilted at an angle to allow the drop to spread evenly forming a homogenous thin layer on the slide surface. They were later transferred to dry in an oven at $40^{o}C$ for about 50 minutes. A total of 81 thin films were formed and labeled as per the sample name of the corresponding CNC syrup as shown in **Table 3.1**.

Table 3. 1: Prepared samples according to the acid type, concentration and hydrolysis time

Samples treated by H_2SO_4		Samples treated by HCl		Samples treated by HNO_3	
Sample 1	H_2SO_4 5% $50^{o}C$ 2h	**Sample28**	HCl 5% $50^{o}C$ 2h	**Sample55**	HNO_3 5% $50^{o}C$ 2h
Sample 2	H_2SO_4 5% $50^{o}C$ 3h	**Sample29**	HCl 5% $50^{o}C$ 3h	**Sample56**	HNO_3 5% $50^{o}C$ 3h
Sample 3	H_2SO_4 5% $50^{o}C$ 4h	**Sample30**	HCl 5% $50^{o}C$ 4h	**Sample57**	HNO_3 5% $50^{o}C$ 4h
Sample 4	H_2SO_4 5% $70^{o}C$ 2h	**Sample31**	HCl 5% $70^{o}C$ 2h	**Sample58**	HNO_3 5% $70^{o}C$ 2h
Sample 5	H_2SO_4 5% $70^{o}C$ 3h	**Sample32**	HCl 5% $70^{o}C$ 3h	**Sample59**	HNO_3 5% $70^{o}C$ 3h
Sample 6	H_2SO_4 5% $70^{o}C$ 4h	**Sample33**	HCl 5% $70^{o}C$ 4h	**Sample60**	HNO_3 5% $70^{o}C$ 4h
Sample 7	H_2SO_4 5% $90^{o}C$ 2h	**Sample34**	HCl 5% $90^{o}C$ 2h	**Sample61**	HNO_3 5% $90^{o}C$ 2h
Sample 8	H_2SO_4 5% $90^{o}C$ 3h	**Sample35**	HCl 5% $90^{o}C$ 3h	**Sample62**	HNO_3 5% $90^{o}C$ 3h

Sample 9	H_2SO_4 5% 90^oC 4h	**Sample36**	HCl 5% 90^oC4h	**Sample63**	$HNO_3$5% 90^oC 4h
Sample10	H_2SO_4 10%50^0C2h	**Sample37**	HCl 10%50^oC2h	**Sample64**	HNO_3 10%50^oC2h
Sample11	H_2SO_4 10%50^0C3h	**Sample38**	HCl 10%50^oC3h	**Sample65**	HNO_3 10%50^oC3h
Sample12	H_2SO_4 10%50^0C4h	**Sample39**	HCl10%50^oC4h	**Sample66**	HNO_3 10%50^oC4h
Sample13	H_2SO_4 10%70^oC2h	**Sample40**	HCl10%70^oC2h	**Sample67**	$HNO_3$10%70^oC2h
Sample14	H_2SO_4 10%70^oC3h	**Sample41**	HCl10%70^oC3h	**Sample68**	$HNO_3$10%70^oC3h
Sample15	H_2SO_4 10%70^oC4h	**Sample42**	HCl 10%70^oC4h	**Sample69**	HNO_3 10%70^oC4h
Sample16	H_2SO_4 10%90^oC2h	**Sample43**	HCl 10%90^oC2h	**Sample70**	HNO_3 10%90^oC2h
Sample17	H_2SO_4 10%90^oC3h	**Sample44**	HCl 10%90^oC3h	**Sample71**	HNO_3 10%90^oC3h
Sample18	H_2SO_4 10%90^oC4h	**Sample45**	HCl 10%90^oC4h	**Sample72**	HNO_3 10%90^oC4h
Sample19	H_2SO_4 15%50^oC2h	**Sample46**	HCl 15%50^oC2h	**Sample73**	HNO_3 15%50^oC2h
Sample20	H_2SO_4 15%50^oC3h	**Sample47**	HCl 15%50^oC3h	**Sample74**	HNO_3 15%50^oC3h
Sample21	H_2SO_4 15%50^oC4h	**Sample48**	HCl 15%50^oC4h	**Sample75**	$HNO_3$15%50^oC4h
Sample22	H_2SO_4 15%70^oC2h	**Sample49**	HCl 15%70^oC2h	**Sample76**	HNO_3 15%70^oC2h
Sample23	H_2SO_4 15%70^oC3h	**Sample50**	HCl 15%70^oC3h	**Sample77**	HNO_3 15%70^oC3h
Sample24	H_2SO_4 15%70^oC4h	**Sample51**	HCl 15%70^oC4h	**Sample78**	$HNO_3$15%70^oC4h
Sample25	H_2SO_4 15%90^oC2h	**Sample52**	HCl 15%90^oC2h	**Sample79**	$HNO_3$15%90^oC2h
Sample26	H_2SO_4 15%90^oC3h	**Sample53**	HCl 15%90^oC3h	**Sample80**	HNO_3 15%90^oC3h
Sample27	H_2SO_4 15%90^oC4h	**Sample54**	HCl 15%90^oC4h	**Sample81**	HNO_3 15%90^oC4h

3.3.2.2 Manufacture of Aligned CNC Films

The CNCs used here were prepared using HCl acid hydrolysis process at a constant temperature of 50^oC. With varied acid concentrations of 5%, 10% and 15%, the hydrolysis time was kept constant at 4hrs. The final product which was the suspensions of aqueous cellulose nanocrystals suspensions were finally utilized to create thin films. The deposition of the thin films was achieved using a convective shear alignment assembly setup. The convective shear alignment set up consisted of a horizontal solid support and a withdrawal plate that is movable. Silica material that was laden with cations was adopted as the substrate. A homogeneous mixture of sulfuric acid and hydrogen peroxide in the ratio 3:2 was used to clean the silica substrate for 30 minutes. They were then rigorously rinsed using deionized water. To perform the deposition, the silica substrate was placed in the horizontal platform of the solid support as shown in **Figure 3.7.** Using a syringe, 20 ml of CNC suspension was measured and introduced in the chamber between the inclined deposition plate and the horizontal substrate. The deposition plate is inclined at 20° angle relative to the horizontal plane. A uniform thin film of the CNC suspension was then smeared on the substrate surface by gently moving the deposition plate at a non-accelerating speed on top of the fixed substrate laid on the upper surface of the horizontal solid support. The deposited thin films were finally air-dried in a cabinet having a laminar air flow.
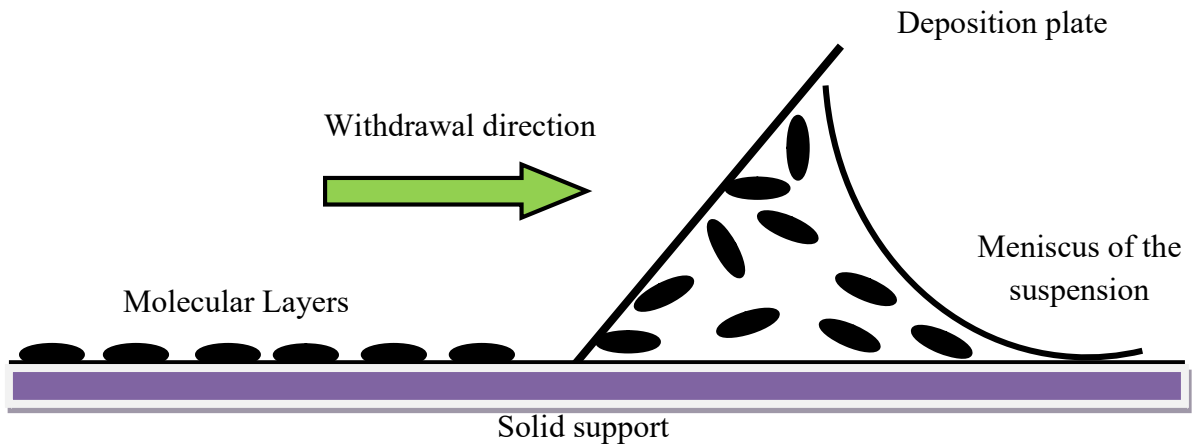
Figure 3. 7: Experimental setup for assembly and deposition showing the CNC suspension, solid support and deposition plate

3.3.2.3 Fabrication of Piezoelectric Sensor

The piezoelectric sensor basically consists of a deposited CNC thin film sandwiched between two electrode plates. The electrode plates are made from a 5mm wide copper tape plated with tin. The tape was folded so that the metal side was in contact with the sensor material. The prepared CNC films were sandwiched between two copper electrodes using a tape as shown in the schematic diagram below. An adhesive film that has glue on both sides was used assemble the electrodes on both sides of the thin film surface. Crimp connectors were used to make the connections to the electrodes to the external circuitry.

(a)   (b)
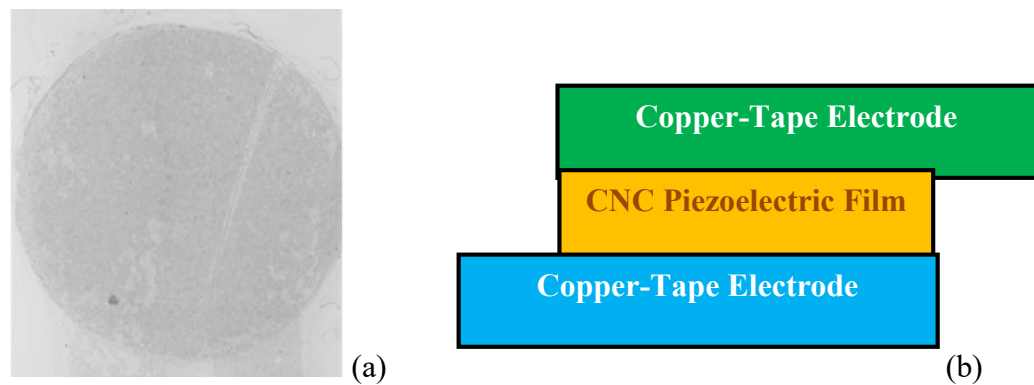
Figure 3. 8: A photograph of a CNC (a) film and a schematic side-view of a CNC sensor sandwiched between copper electrodes (b)

3.3.2.4 Sensitivity Measurement

In the sensitivity measurement of the fabricated piezoelectric sensor, the study adopted the protocol of Rajala et al [142]. A dynamic force generator was used to measure the sensitivity of the fabricated sensor generator. Dynamic excitation force was generated by a mini shaker of the model Bruel & Kjaer type 4180. For referencing purposes, PCB Piezotronics model number 209C02, which is a highly sensitive dynamic force sensor was adopted. The static force between the shakers piston and the sample was measured using a load cell which equally acted as the reference sensor. **Figure 3.9** outlines the schematics of the setup for the piezoelectric sensor sensitivity measurements.

71
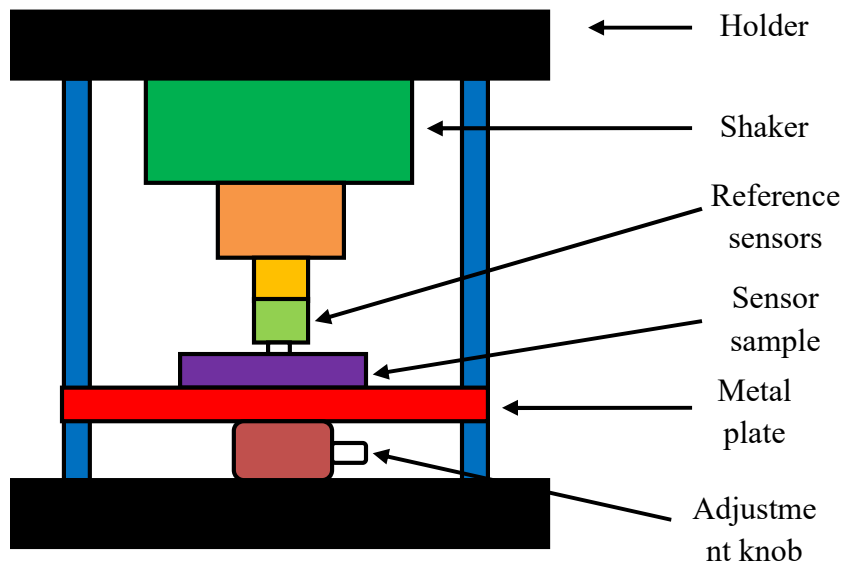
Figure 3. 9: Schematic view of the sensitivity measurement setup

Figure 3.10 shows the block diagram of the sensitivity measurement setup.
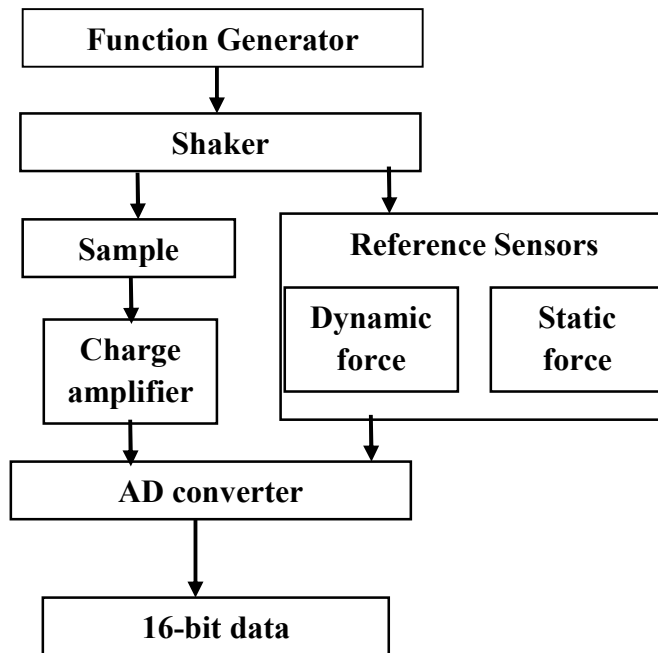
Figure 3. 10: The block diagram of the sensitivity measurement setup

The sensitivity of the sensor is mathematically obtained by dividing the magnitude of the charge generated by the sensor due to the external force by the dynamic force on the sensor.

$$Sensitivity = \frac{Generated\ Charge}{Force} \tag{3.1}$$

The SI unit of sensor sensitivity is thus C/N. However, since the charge generated from the sensor is in very little magnitude the unit adopted is picocoulombs per Newton pC/N. The amount of charge generated by the sensor due to the external stress was measured by a connected circuitry of a charge amplifier and a 16-bit AD-converter. A coaxial cable and crimp connecters were used to interface the AD-converter with the sensor. The AD-converter, in addition, could help in sampling the voltage signals from the reference sensor.

3.3.3 Characterization Techniques

3.3.3.1 Optical Microscopy

Optical microscopy is a technique that allows us to study the morphological features and surface structures of a sample through optical magnification. An optical microscope (OM) is a light instrument that uses visible light and a systematic combination of magnifying lenses to magnify images of very small objects in micrometer scale. A typical OM consists of the following principal parts; a sample specimen stage to hold the specimen, the objective lens, condenser lens the eyepiece lens, projector lens and photographic plate acting as the screen. This set of lenses are enclosed in a movable tube. The tube is movable to allow change of magnification and for the mechanical control for easy movement of the body and the specimen during focusing. **Figure 3.11** shows the architecture of an optical microscope.
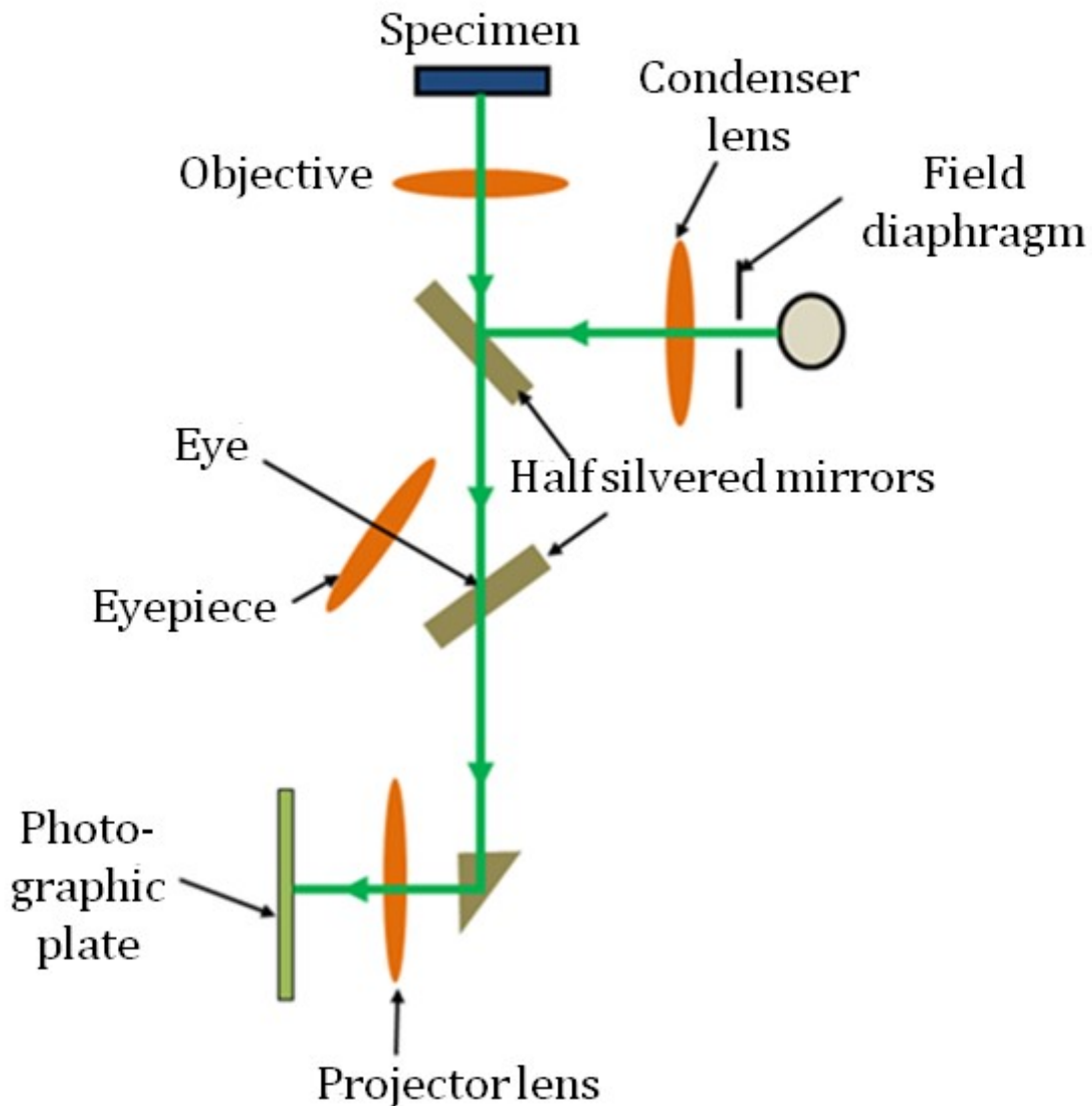
Figure 3. 11: The architectural design of a light microscope [143]

As shown in the light path of **Figure 3.11**, the condenser lens of the optical microscope focuses the light beam direct to the sample while the objective lens magnifies the beam containing the image of the sample. This magnified beam is directed to the projector lens which acts as the platform on which the image is viewed by the observer. The ability of a microscope to show fine details of the object being observed is called the optical resolution (R) [101], and the maximum resolution (R_{max}) of an optical microscope is given by;

$$R_{max} = \frac{0.61\lambda}{N.A} \tag{3.2}$$

Where 0.61 = The geometrical constant based on the average 20-20 eye (normal eye),

λ = The wavelength of illuminated light, and

N.A= The Numerical Aperture.

Taking the refractive index of medium as η and letting α be the angle subtended by the lens, then the measure of the light gathering capabilities of an objective lens (Numerical Aperture, *N.A*), is given by;

$$N.A = \eta sin\alpha$$

$$\tag{3.3}$$

Using equation (3.3) in equation 3.2, we obtain the alternative relationship for the maximum resolution as;

$$R_{max} = \frac{0.61\lambda}{\eta sin\alpha} \tag{3.4}$$

The image of the object is formed by the objective lens and is given by the objective magnification m_o. This image is further magnified by the eyepiece lens by eyepiece magnification m_i. The Total Magnification in an optical microscope is therefore the product of the objective and eyepiece magnifications.

In this study, specimen of CNCs prepared in different acid types, at varied hydrolysis temperatures, timings and acid concentrations were viewed under light microscope (LEICA DM 500) to observe the surface morphology and determine how these varied hydrolysis parameters affect the formation of the surfaces of the prepared CNCs. The images formed were extracted from a computer through an interface.

3.3.2.2 UV-Vis Spectroscopy

The word spectroscopy is coined from two key scientific terms namely; spectro meaning 'of spectrum' and scope meaning 'study of'. Spectroscopy is therefore the branch of science that deals with the study of spectrum. It involves the investigation of how electromagnetic field

interacts with matter. Its origin can be traced to the study of dispersion of light by prisms. Its scope later widened to include the study of light-matter interactions as the radiative energy is varied due to change in their wavelength or frequency. Basically, the field of spectroscopy can be distinctly categorized into two broad categories: The first category is the techniques based on energy transfer between photon and the sample under study while the second category is the technique based on refractions, reflections, dispersion, diffraction, or scattering of light by the sample leading to the change in the amplitude, polarization, phase angle, or even in the final direction of propagation of the electromagnetic radiation.

Up to date, spectroscopy has undergone scientific evolution and has remained a vital technique for characterization and analyses of various samples in our research laboratories and even in the manufacturing industries. One of the most important spectroscopic techniques used in optical analysis of materials is the Ultraviolet-Visible light (UV-Vis) spectrophotometry. UV-Vis Spectrophotometer is a characterization tool that measures, records and displays the intensity of light as a function of wavelength in a spectral format. The architectural design of UV-Vis spectrophotometer is shown in **Figure 3.12**. As is outlined in the figure, the light beam is diffracted into a spectrum of wavelengths. The different intensities at each wavelength are then detected by a charge-coupled device and the resultant spectrum is displayed on the screen as a graph. The light from the lamps is directed by an array of mirrors to pass through the sample in the spectrophotometer through a slit. The incident light on the sample will undergo through three processes. Some will undergo absorption into the sample, another fraction will be transmitted and propagate past the sample while a small fraction will undergo refection and travel back to the source. The light is therefore said to undergo absorbance, transmittance and reflectance. The UV-Vis Spectroscopy compares the intensities of the incident light on the sample with that of the transmitted light. The output result is a graph of intensity against wavelength as shown in [144].
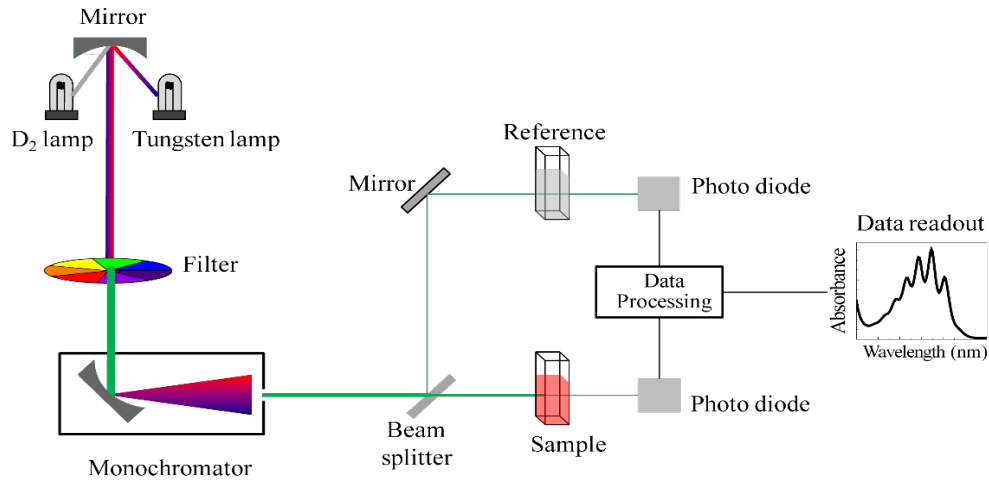
Figure 3. 12: The architecture of the UV-Vis spectrophotometer [144]

One of the laws that govern the measurements and analysis of the absorbance spectra obtained from UV-Vis spectroscopy measurements is the Beer-Lamberts Law. It gives the relationship of the light transmitted to the absorbance. From Beer lamberts law, we obtain a linear relationship of the intensity of the absorbing light and the distance travelled by light through the sample as given in equation (3.5) below.

$$log\left(\frac{I_0}{I}\right) = ct\alpha \tag{3.5}$$

Where c = the concentration of the sample,

   t = the path length (thickness of the sample, and

   α = the absorption coefficient.

The product on the RHS of equation (3.5) is the absorbance A. The absorbance A can therefore be expressed as;

$$A = ct\alpha \tag{3.6}$$

Using equation (3.6) in (3.5), we obtain;

$$log\left(\frac{I_0}{I}\right) = A \tag{3.7}$$

Making I the subject of the equation, we obtain;

$$I = I_0 e^{-A} = I_0 e^{-ct\alpha} \tag{3.8}$$

From equation (3.8), we observe that light absorbance of any sample is a factor of an absorption coefficient α. The absorption coefficient can be easily calculated from absorption and/or transmission data sourced from a UV-Vis spectrophotometer. Taking I_0 to be the intensity of the incident light and I to be the intensity of the transmitted light, we can express the optical transmittance (T) according to;

$$T = \frac{I}{I_0} \tag{3.9}$$

Assuming all the interference effects, we can equally express Transmittance as a factor of Reflectance according to;

$$T = \frac{(1-R)^2 e^{-\alpha t}}{1-R^2 e^{-2\alpha t}} \tag{3.10}$$

Where t = light path (sample thickness)

As the product αt approaches infinity, the denominator approaches unity, making Equation (3.10) to take the form;

$$T = (1 - R)^2 e^{-\alpha t} \tag{3.11}$$

Further, taking $I = 1 - R$ equation becomes;

$$T = I^2 e^{-\alpha t} \tag{3.12}$$

The relations in equation 3.10 and 3.11 give the relations between the transmittance with reflectance and the intensity of the absorbed light. Absorbance measurements on the prepared samples were performed at Kenya Bureau of Standards laboratory, Lake Region Centre in Kibos, Kisumu, using UV-Vis Spectrophotometer (Agilent-Technology, Chary60 UV-Vis). However, a Nano drop spectrophotometer (Eppendorf Biospectrometer ® Kinetic) was later acquired by JOOUST laboratory which was later used for all the UV-Vis spectroscopy for all the availed samples prepared under different hydrolysis parameters. The acquired data were used to plot UV-Vis absorbance graphs that were analyzed using OriginPro software to determine the values of the peak absorbance wavelength, full wave at half maximum, band gap energy, Urbach energy and other optical parameters.

The Tauc's Model of the Band Gap Energy

One of the most important electronic properties of a material is the band gap energy which is the minimum energy required to excite an electron from its stable ground state to a higher energy leaving the electron in an excited state. For an electron to participate in electrical conduction it must be excited from the valence band (ground state) to the conduction band (excited state). The absorption edge of the absorption spectrum is the initial step of electronic transitions from the highest occupied valence band (HOVB) to the lowest unoccupied conduction band (LUCB). The difference in energy between these two bands is the Band Gap Energy. *Tauc's* Model is one of the techniques used to calculate the band gap energy using absorbance spectra measured by a UV-Vis spectrophotometer. The *Tauc's* equation gives the relationship between the coefficient of absorption, α, the photon energy of the incident radiation, *hv,* and the Band gap Energy E_g.

In most experimental results, large absorption values are obtained. To take care of this, an *n*-order dependence of band gap energy with the materials absorption coefficient is observed. All these relationships and the n-order dependence of the band gap are given by *Tauc's* equation as per;

$$\alpha hv = B\left(hv - E_g\right)^n \tag{3.13}$$

Where;

h = The Planck's constant,

V = The photon's frequency,

α = The absorption coefficient,

E_g = The Band gap energy.

and B = a constant independent of energy, also known as band tailing parameter.

The value of the exponent *n* depends on the nature of the electronic transition. The transition can be allowed or forbidden, and in both cases, it can occur directly or indirectly.

For transitions that are direct allowed, $n = \dfrac{1}{2}$

For transitions that are direct forbidden, $n = \dfrac{3}{2}$

For transitions that are indirect allowed, $n = 2$

Lastly, for transitions that are indirect forbidden, $n = 3$.

The absorption coefficient is a function of wavelength and is given by;

$$\alpha_{(\lambda)} = 2.303 \left[\frac{A}{d}\right] \tag{3.14}$$

Where d = path length (sample thickness)

and A = The absorption value at the given wavelength.

When the Tauc's Equation given in equation (3.13) is compared to the linear equation $y=mx+c$ a linear graph is obtained when we plot a graph of $(\alpha h v)^{\frac{1}{n}}$ (y-axis) against $h v$ (x-axis). From the graph obtained, the Band gap energy is estimated by fitting the linear region of the curve obtained from the *Tauc's* plot and extrapolated to the x-axis. The x-axis intercept corresponds to the Band Gap Energy of the material under study. This is supported by the *Tauc's* analysis as shown in the equations below.

From the *Tauc's* equation given in equation (3.12), we can see that;

$$\alpha h v = A(h v - E_g)^n \tag{3.15}$$

By taking $n = \frac{1}{2}$ and doing further rearrangements, we obtain equation (3.15) to be

$$(\alpha h v)^2 = A h v - A E_g \tag{3.16}$$

Taking $A=1$ leads us to

$$(\alpha h v)^2 = h v - E_g \tag{3.17}$$

At x intercept $(\alpha h v)^2 = 0$ and $h v = E_g$

The corresponding value of $h v$, at the x-axis therefore gives the value of the band gap energy. In this study, fingerprints on the hydrolysis parameters on the optical absorption of the band gap energy of the fabricated CNCs have been systematically investigated.

Urbach Energy

An electron in the valence band is always stable and is said to be in ground state. When such an electron is shone with light, it absorbs the photon energy and gets excited making it to undergo a transition from the highest occupied valence band (HOVB) to the lowest unoccupied conduction band (LUCB). During this transition, when the electron encounters some disorder in the

arrangement of particles, its density of state is subjected to tailing into the energy gap. This phenomenon of tailing of density of state extending into the energy band gap is called Urbach tail. The energy associated with the Urbach tail it is referred to Urbach energy.

The Urbach energy equation is given by;

$$\propto (h\nu) = \alpha_o \exp\left(\frac{h\nu}{E_u}\right) \tag{3.18}$$

Where α = the absorbance coefficient

α_o = a constant,

$h\nu$ = the photon energy

and E_u = the Urbach energy

The absorbance coefficient α is further given by $\alpha = \frac{2.303A}{t}$

Where A = the absorbance

and t = the sample thickness

By taking the natural logarithm of both sides and further rearranging, the equation (3.19) becomes.

$$\ln\alpha = h\nu\left(\frac{1}{E_u}\right) + \ln\alpha_0 \tag{3.20}$$

A plot of $\ln\alpha$ (y-axis) vs $h\nu$ therefore yields a linear graph whose gradient is the reciprocal of the Urbach energy. Using the absorbance data, the absorbance coefficient α and consequently $\ln\alpha$ were calculated. The photon energy was equally calculated for each absorbance wavelength and graphs plotted using OriginPro. Values of Urbach energies were estimated for various samples.

3.3.2.3 Fluorescence Spectroscopy

Luminescence is a phenomenon widely observed when light interacts with matter. The word luminescence originates from Latin word *lumen* which means light. Luminescence is defined as the spontaneous emission of radiation/light from a species that is electronically excited and lacks thermal equilibrium with its environment. There are various types of luminescence depending on the mode of excitation. One of the famous types of luminescence is the photoluminescence which is the emission of light caused by the direct photoexcitation of the emitting species. Other types of luminescence caused by various excitation modes include; triboluminescence, electroluminescence, bioluminescence, chemiluminescence, cathodoluminescence, thermoluminescence, radioluminescence and sonoluminescence. The three major forms of photoluminescence are phosphorescence, fluorescence and delayed fluorescence. In modern scientific research and industrial applications, Fluorescence and phosphorescence play vital roles. Fluorescence occurs when light lifts an electron to an excited state subjecting it to rapid thermal energy loss to the environment through vibrations and rotations causing an emission of a photon from the lowest-lying singlet excited state. This process of photon emission leads to loss of energy as witnessed in other non-radiative processes such as energy transfer and heat loss. In this research, MCR F96Pro fluorescence spectrometer was used to perform fluorescence measurements on the prepared CNCs. The peak intensities were noted for various CNCs prepared from different hydrolysis parameters.

3.3.2.4 X-Ray Diffraction Measurements

X-rays is one of the high-energy radiations belonging to the electromagnetic spectrum. When an X-ray beam is incident to a crystalline surface at some angle theta, the beam undergoes deviation at the cleavage face of the crystal. The phenomenon in which of X-ray beam undergoes interference is commonly known as X-ray Diffraction (XRD). The phenomenon is a clear testimony of the periodic arrangement of crystals in a crystalline lattice. As such, XRD can be used to study the crystalline index of a material. The first scientists to discover the XRD phenomenon were Sir W.H. Bragg and Sir W.L. Bragg in 1913 from England. They managed to develop a relationship that explains the X-ray diffraction phenomenon, and is to date widely known as the Bragg's law of X-ray diffraction. Consider a beam of 2 X-rays with a constant

wavelength λ, being incident in a crystalline solid with crystalline spacing d as shown in the diagram in **Figure 3.13.** Let the beam be incident to the crystalline planes at an angle *theta*. After reflection from the two surfaces, the path difference of the two x rays will be the distance AB+BC.
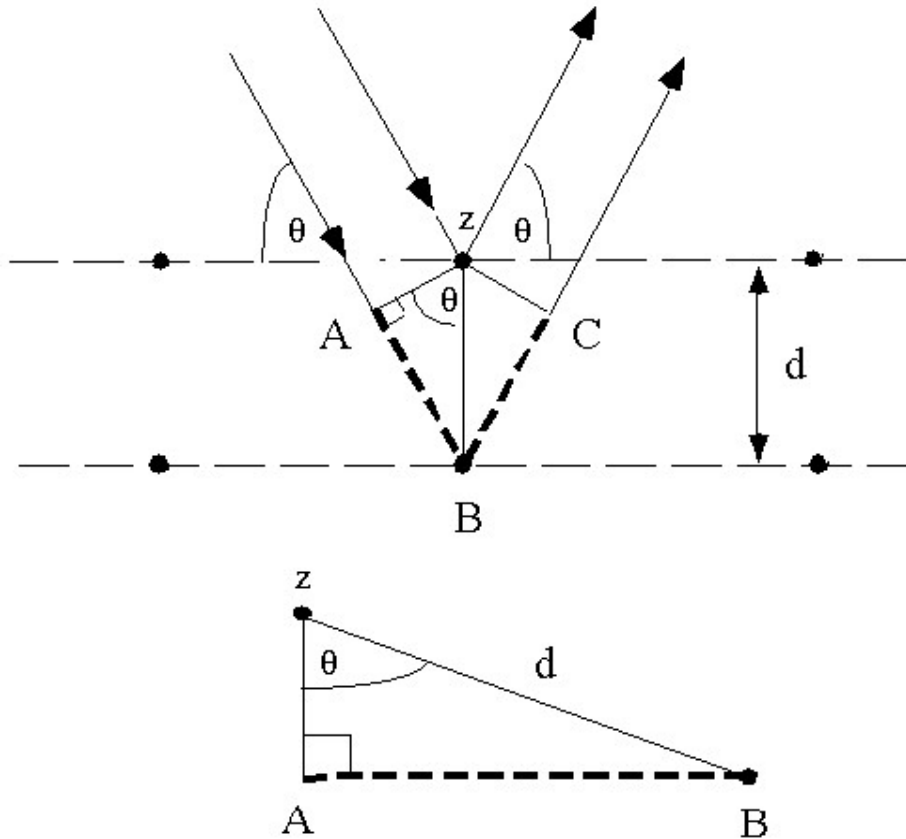
Figure 3. 13: Geometric representation of a beam two X-rays undergoing diffraction at two consecutive planes of a crystalline solid

Constructive interference occurs only when the path difference is an integral multiple of the wavelength of the x ray beam, i.e.

$$n\lambda = AB + BC \qquad (3.21)$$

Where n is an integer

But $AB = BC$. Equation (3.21) therefore becomes;

$$n\lambda = 2AB \qquad (3.22)$$

Taking triangle ABZ as shown in the inset diagram in **Figure 3.13**, we observe that;

$$\frac{AB}{d} = sin\theta \qquad (3.23)$$

$$AB = dsin\theta \qquad (3.24)$$

Using equation (3.22) in equation (3.20) we obtain;

$$n\lambda = 2dsin\theta \qquad (3.25)$$

Equation (3.24) is the widely known Bragg's law. Therefore, for diffraction to occur, *Bragg's Law* must be satisfied. The atomic planes of a crystal can cause an incident beam of X-rays to interfere with one another as they leave the crystal as depicted in X-ray diffraction. XRD has therefore been applied in crystallography. As well known, a crystal has a periodic arrangement of the unit cell into a lattice. The unit cell also has a single atom or atoms within a fixed arrangement. Crystals consist of planes of atoms that are spaced a distance *d* apart, but can be resolved into many atomic planes, each with a different *d* spacing *a, b* and *c* (length) and α, β and γ, the angles between *a, b* and *c*. The values *a, b, c*, α, β and γ are lattice constants or parameters which can be determined by XRD. With this strength, X ray diffraction technique has gained both laboratory and industrial vast applications including to measure the average spacings between layers or rows of atoms; to determine the orientation of a single crystal or grain; to find the crystal structure of an unknown material and to measure the size, shape and internal stress of small crystalline regions, amongst others. **Figure 3.14** shows the Basic Features of typical XRD Experiment. Its principal parts are the production stage, Diffraction at the substrate, detection of the diffracted ray and the analysis of the diffraction as circled in the diagram.
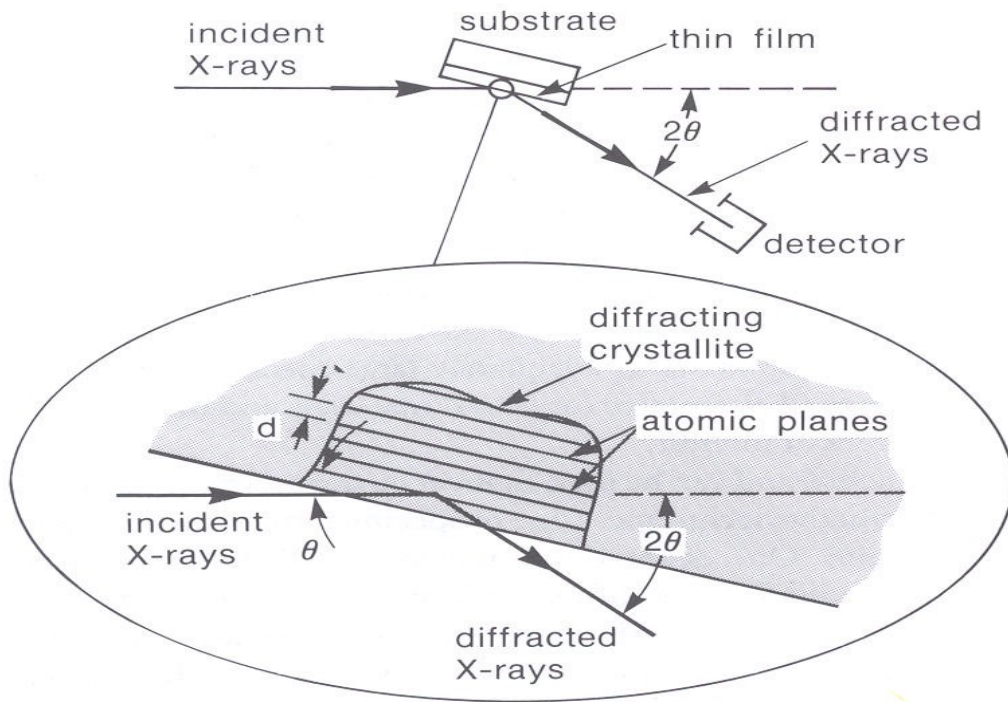
Figure 3. 14: The basic features of an XRD machine

The phase identification and crystalline structure of the cellulose composites were investigated by a PANalyticalX'Pert PRO diffractometer using a Cu Kα radiation (λ = 1.54 Å) with a current of 40 mA and an anode voltage of 45 kV.

CHAPTER FOUR

RESULTS AND DISCUSSION

4.1   Introduction

In this chapter, all the results obtained so far from our laboratory analysis using various equipment and analysis tools/software are schematically presented. The samples were subjected to optical measurements where UV-Vis spectrophotometer was used to obtain the absorption spectral graphs for optical analysis. Further a florescence spectrophotometer was used for photoluminescence measurements. The absorbance data obtained from the UV-Vis spectrophotometer was used to obtain peak absorbance wavelength, the full wave at half maximum values and the band gap energy for all the samples prepared. Similarly, the fluorescence spectrophotometer was used to obtain fluorescence measurements of various samples.

4.2   UV-Vis Characterization of the CNCs

The UV-Vis absorption data both for the liquid samples and the thin films samples of the CNCs were collected using SHIMADZU UV-Vis Spectrophotometer. During the optical measurement procedure, values of absorbance of the samples were obtained in the Ultra Violet and Visible light wavelength range (200 nm to 800 nm) in an interval of 0.2 nm and the data recorded in Excel format. The OriginPro software was then used to obtain various spectral graphs from the excel data acquired. The software was further used to perform the analysis of the spectra and investigate the optical properties of our extracted CNCs. The roles of each parameter used in the hydrolysis process on the optical properties of the extracted water hyacinth based CNCs were equally investigated. In the discussions below, we highlight some of the analyzed absorbance spectra for various samples prepared at different hydrolysis conditions.

4.3 Absorbance Properties of CNCs

4.3.1 The Role of the Acid Hydrolysis Time on the Optical Absorbance of CNCs

To investigate the role of hydrolysis reaction time on the optical absorption of CNCs, the spectral absorption graphs of samples made under same type of acid, equal acid concentration and uniform hydrolysis temperature but with varying times of hydrolysis were systematically compared. For each spectrum the value of the peak absorption wavelength, X_c, and full wave at half maximum (FWHM) were obtained after performing Gaussian fits on the spectra. The first investigation was on the CNCs prepared using H_2SO_4 of uniform concentration of 10% at a constant temperature of 50^oC with varying hydrolysis reaction times of 2hrs, 3hrs and 4hrs. To study the effect of different acids, the same conditions were used to prepare samples in HCl and HNO_3. The UV-Vis spectroscopy revealed the absorbance spectra displayed in **Figure 4.1 a), c) e)** and their normalized counterparts **b), d) f)** for H_2SO_4, HCl and HNO_3 respectively.
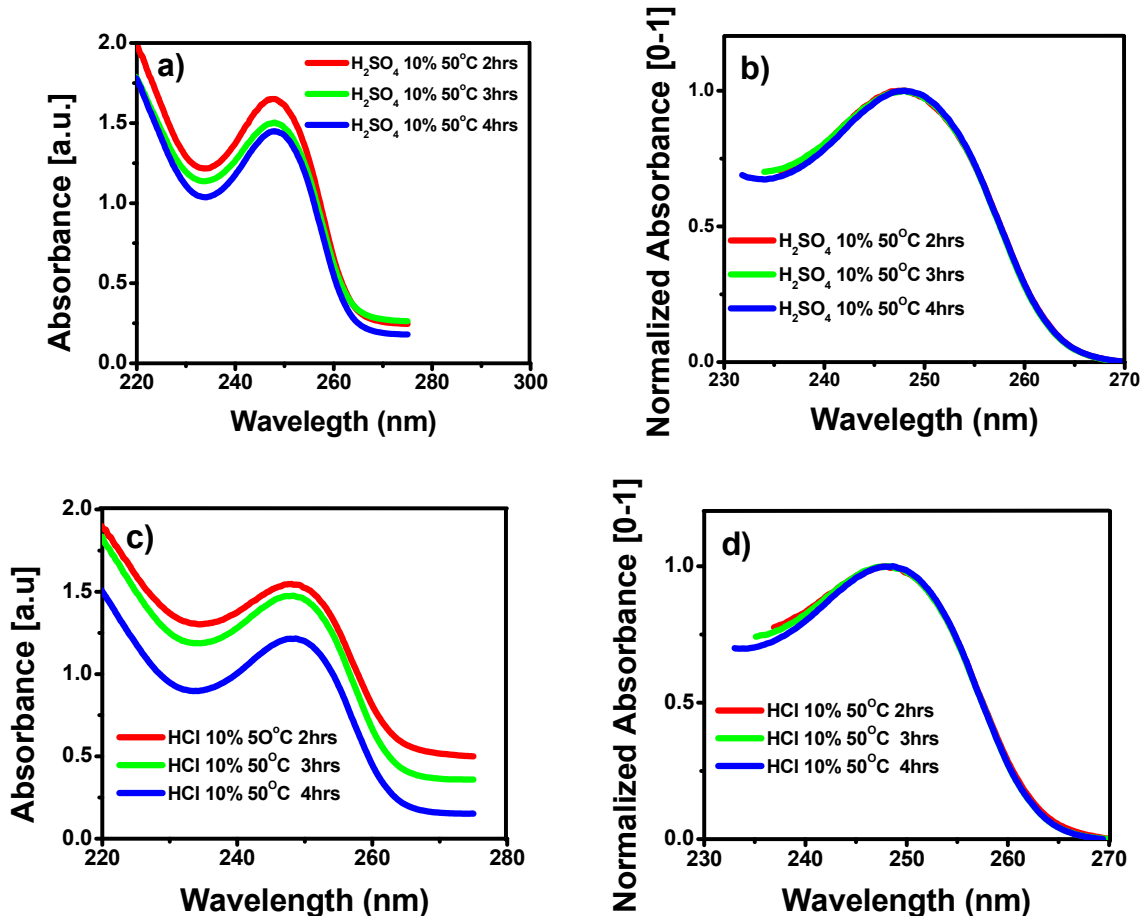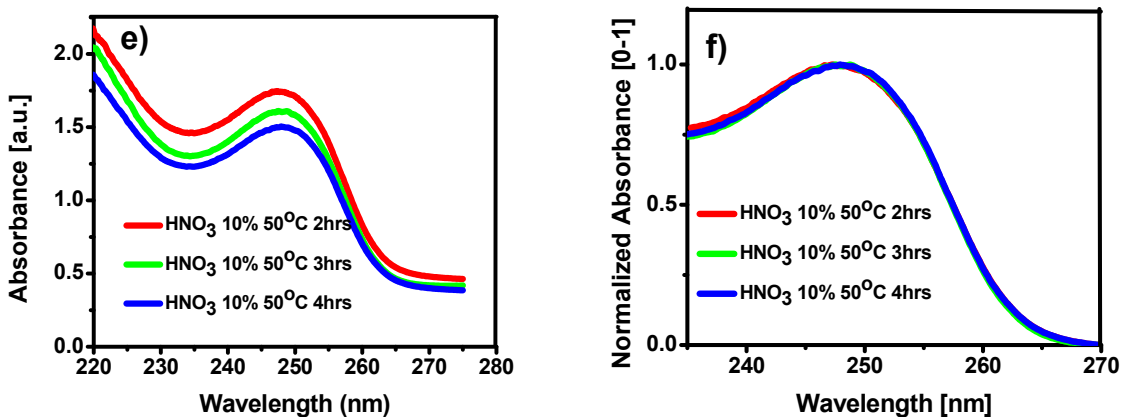
Figure 4. 1: Absorbance spectra and their normalized forms for CNC samples prepared using 10% H_2SO_4 at 50^oC a-b), using 10% HCl at 50^oC c-d) and using 10% HNO_3 at 50^oC e-f) with varying hydrolysis times of 2hrs, 3hrs and 4hrs

For H_2SO_4, the Peak absorbance wavelengths were found to be 247.28 nm, 247.34 nm and 247.62 nm for 2hrs, 3hrs and 4hrs reaction times respectively. For HCl, the Peak absorbance wavelengths were found to be 247.35 nm, 247.44 nm and 247.75 nm respectively for 2hrs, 3hrs and 4hrs reaction times respectively and lastly for HNO_3, the Peak absorbance wavelengths were found to be 246.95 nm, 247.31 nm and 247.34 nm respectively. Similarly, for H_2SO_4, the FWHM were found to be 12.12 nm, 12.40 nm and 12.98 nm for 2hrs, 3hrs and 4hrs reaction times respectively. For HCl, the FWHM were found to be 10.92 nm, 12.04 nm and 13.06 nm respectively for 2hrs, 3hrs and 4hrs reaction times respectively and lastly for HNO_3, the FWHM were found to be 11.93 nm, 13.82 nm and 15.73 nm respectively. These are depicted in **Table 4.1** and in **Figure 4.2**.

Table 4. 1: Table of absorption peak maxima X_c and FWHM for CNC samples prepared using 10% H_2SO_4 at 50°C, 10% HCl at 50°C and using 10% HNO_3 at 50°C with varying hydrolysis times of 2 hrs, 3 hrs and 4 hrs.

Acid	10% H_2SO_4 at 50°C			10% HCl at 50°C			10% HNO_3 at 50°C		
Time	2 hrs	3 hrs	4hrs	2 hrs	3 hrs	4hrs	2 hrs	3 hrs	4hrs
Peak Wavelength X_c (nm)	247.28	247.34	247.62	247.35	247.44	247.75	246.95	247.31	247.34
FWHM (nm)	12.12	12.40	12.98	10.92	12.04	13.06	11.93	13.82	15.73
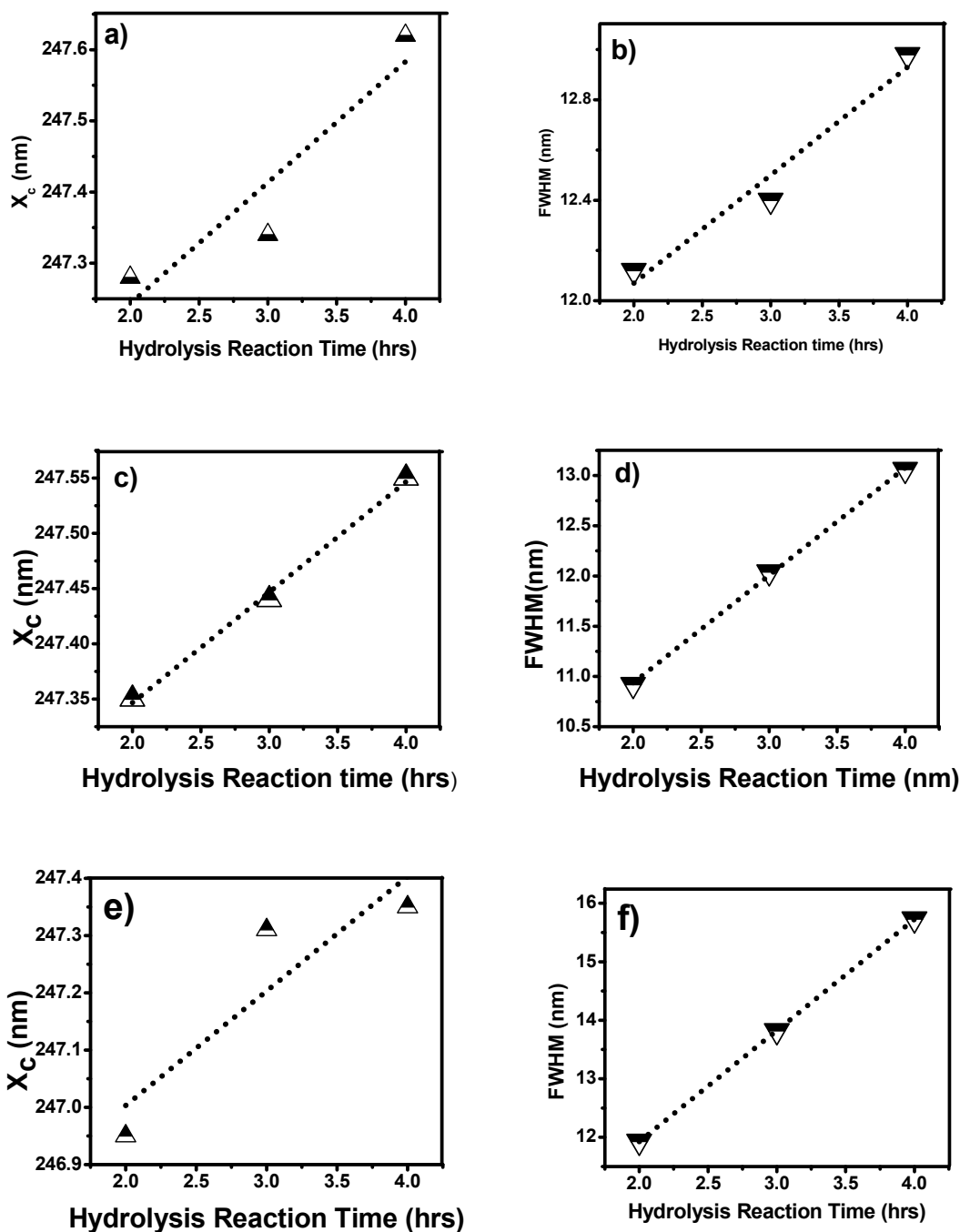
Figure 4. 2: The graphs of Peak Absorbance wavelength X_c and the Full Wave at Half maximum (FWHM) height as functions of the hydrolysis reaction time for CNC samples prepared using 10% H_2SO_4 at 50°C a-b), using 10% HCl at 50°C c-d) and using 10% HNO_3 at 50°C e-f) with varying hydrolysis times of 2 hrs, 3 hrs and 4 hrs

From **Table 4.1** and corresponding graphs in **Figure 4.2**, it is observed that the wavelength of the maximum absorption peaks X_c increased near linearly with the hydrolysis time for all the acids used. This is an indicator that increases in time of hydrolysis increases the absorption property of CNCs as they are able to absorb at lower energies. Increase in hydrolysis reaction time leads to enhanced crystallinity thus leading to the red shift in absorbance peaks. As the hydrolysis time is prolonged, the acid eats more into the lignin and hemicellulose parts leaving more crystalline cellulose. This is seen in the increase of the absorption peak wavelengths (lower energy) with the increase in time of hydrolysis. Similarly, the FWHM also increased near linearly with the hydrolysis time for all the acids used. This suggests that the distribution of the absorbing moieties increased with time of hydrolysis.

4.3.2 The Effect of the Hydrolysis Temperature on Optical Absorbance of CNCs

In order to elucidate the effect of the hydrolysis temperature on optical absorbance of CNCs, absorbance spectra of some few samples prepared under equal acid concentration, same acid type, constant hydrolysis time but with varying acid hydrolysis temperatures of 50°C, 70°C and 90°C were recorded and displayed. For each spectrum, the value of the maximum absorption wavelength and FWHM were obtained after performing Gaussian fitting of the spectra. From the analyses, the maximum absorbance wavelength for CNC samples prepared using 5% H_2SO_4 for 2hrs with varying hydrolysis temperatures of 50°C, 70°C and 90°C were found to be 244.4 nm, 245.1 nm and 247.2 nm respectively. The maximum absorbance wavelengths for CNC samples prepared using 5% HCl for 2hrs with varying hydrolysis temperatures of 50°C, 70°C and 90°C were found to be 246.2 nm, 248.1 nm and 247.3 nm respectively. The maximum absorbance wavelengths for CNC samples prepared using 5% HNO_3 for 2 hrs with varying hydrolysis temperatures of 50°C, 70°C and 90°C were found to be 245.8 nm, 247.6 nm and 246.6 nm respectively. This is an indicator that increases in hydrolysis temperature increases the absorption property of CNCs. Similarly, for H_2SO_4, the FWHM were found to be 11.13 nm, 11.46 nm and 11.81 nm for 50°C, 70°C and 90°C hydrolysis temperatures respectively. For HCl, the FWHM were found to be 10.92 nm, 12.04 nm and 13.06 nm respectively for 50°C, 70°C and

90°C hydrolysis temperatures respectively and lastly for HNO_3, the FWHM were found to be 11.97 nm, 12.89 nm and 13.61 nm respectively. These values are depicted in **Table 4.2.**

Table 4. 2: Table of absorption peak maxima X_c and FWHM for CNC samples prepared using 5% H_2SO_4 for 2 hrs, 5% HCl for 2 hrs and using 5% HNO_3 for 2 hrs with varying hydrolysis temperatures of 50°C, 70°C and 90°C.

Acid	5% H_2SO_4 for 2hrs			5% HCl for 2hrs			5% HNO_3 for 2hrs		
Temp (^{o}C)	50	70	90	50	70	90	50	70	90
Peak Wavelength X_c (nm)	244.4	245.1	247.2	246.2	248.1	247.3	245.8	247.6	246.6
FWHM (nm)	11.13	11.46	11.81	10.92	12.04	13.06	11.97	12.89	13.61

From **Table 4.2**, it is observed that the wavelength of the maximum absorption peaks X_c increased near linearly with the hydrolysis time for all the acids used. This is an indicator that increases in temperatures of hydrolysis increases the absorption property of CNCs as they are able to absorb at lower energies. Similarly, the FWHM also increased near linearly with the hydrolysis temperature for all the acids used. This suggests that the distribution of the absorbing moieties increased with increase in temperature.

4.3.3 The Effect of the Acid Concentration on Optical Absorbance of Cellulose

In order to elucidate the effect of the acid concentration on optical absorbance of CNCs, absorbance spectra of samples prepared under same hydrolysis temperatures of 50°C, same acid

type, constant hydrolysis time of 4 hrs but with varying acid concentrations of 5%, 10% and 15% were recorded and analyzed. For each spectrum, the value of the maximum absorption wavelength and FWHM were obtained after performing Gaussian fitting of the spectra. From the analyses, the maximum absorbance wavelengths for CNC samples prepared using H_2SO_4 for 4 hrs and hydrolysis of 50^oC with acid concentrations of 5%, 10% and 15% were found to be 245.0 nm, 247.8 nm and 248.0 nm respectively. The maximum absorbance wavelengths for CNC samples prepared using HCl for 4 hrs and hydrolysis of 50^oC with acid concentrations of 5%, 10% and 15% were found to be 246.3 nm, 247.5 nm and 248.4 nm respectively. The maximum absorbance wavelengths for CNC samples prepared using HNO_3 for 4 hrs and hydrolysis of 50^oC with acid concentrations of 5%, 10% and 15% were found to be 248.6 nm, 248.9 nm and 249.3 nm respectively. Similarly, for H_2SO_4, the FWHM were found to be 15.04 nm, 15.97 nm and 16.41 nm for 5%, 10% and 15% acid concentrations respectively. For HCl, the FWHM were found to be 11.21 nm, 13.01 nm and 13.61 nm respectively for 5%, 10% and 15% acid concentrations respectively and lastly for HNO_3, the FWHM were found to be 18.01 nm, 18.27 nm and 19.03 nm for 5%, 10% and 15% acid concentrations respectively. These values are depicted in **Table 4.3.**

The results so far obtained in section 4.3 show that the increase in all the three hydrolysis parameters i.e time, temperature and acid concentration all lead to corresponding increase in optical absorbance of the prepared CNC samples. This is in tandem with what is already in literature as cited by the work done by Dandan O. *et al* [168].

Table 4. 3: Table of absorption peak maxima X_c and FWHM for CNC samples prepared using H₂SO₄ 50°C for 4 hrs, HCl 50°C for 4 hrs and using HNO₃ 50°C for 4 hrs with varying acid concentrations of 5%, 10% and 15%

Acid	H$_2$SO$_4$ 50°C for 4hrs			HCl 50°C for 4hrs			HNO$_3$ 50°C for 4hrs		
Conc (%)	5	10	15	5	10	15	5	10	15
Peak Wavelength Xc (nm)	245.0	247.8	248.0	246.3	247.5	248.4	248.6	248.9	249.3
FWHM (nm)	15.04	15.97	16,41	11.21	13.01	13.69	18.01	12.27	19.03

The red-shift of the optical absorption edge for all the acids suggests increased crystallinity due to improved long-range order of the cellulose atoms within the nanocrystal. The reason is because the increase in concentration of acids directly enhances the hydrolysis process, and thus cellulose hydrolyzed more with increase in concentration of acids. The increase of the FWHM with the acid concentration also suggests that the number of the absorbing moieties were supported by the acid concentration.

4.4 Optical Band Gap Energy of CNCs
4.4.1 Effect of the Hydrolysis Temperature on Optical Band Gap Energy of CNCs

Figure 4.3 shows the *Tauc* graphs generated from the data. From the figure, the band gap energy for CNC samples prepared using 5% HNO₃ for 4hrs with varying hydrolysis temperatures of 50°C, 70°C and 90°C were found to be 5.201 eV, 5.276 eV and 5.303 eV respectively.
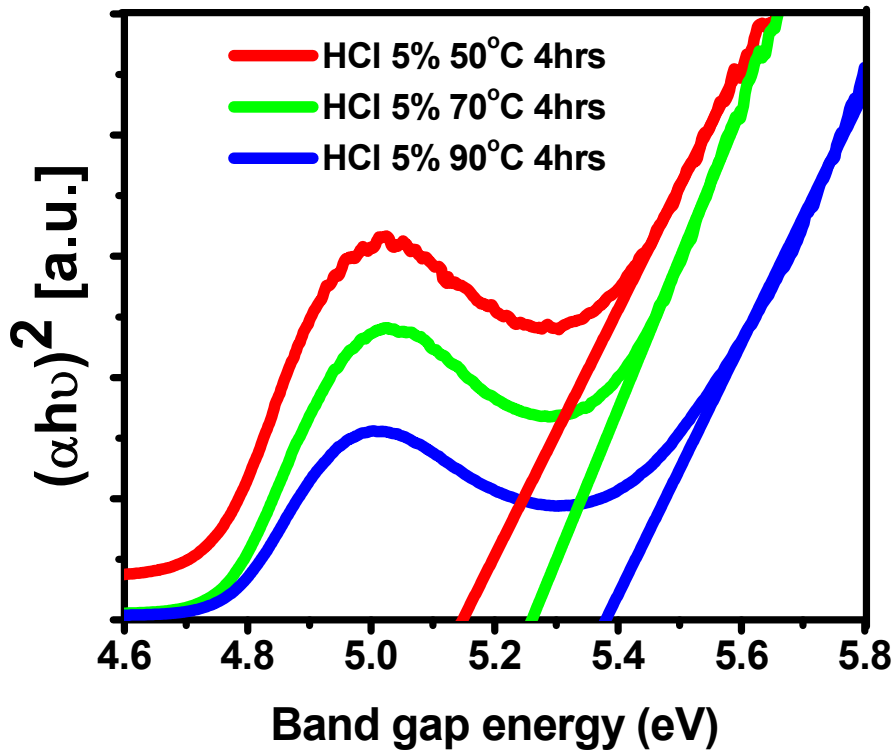
Figure 4. 3: The *Tauc's* graphs for CNC samples prepared using 5% acid concentration, 4 hrs hydrolysis time and 50°C, 70°C and 90°C hydrolysis temperature

A plot of the band gap energy (eV) versus the hydrolysis temperature (°C) shows a direct proportionality as depicted in **Figure 4.4.** The increased hydrolysis temperatures led to increase in reaction rate thus removing the amorphous regions of the cellulose microfibrils along with the semicrystalline and crystalline cellulose thus increasing the optical band gap.
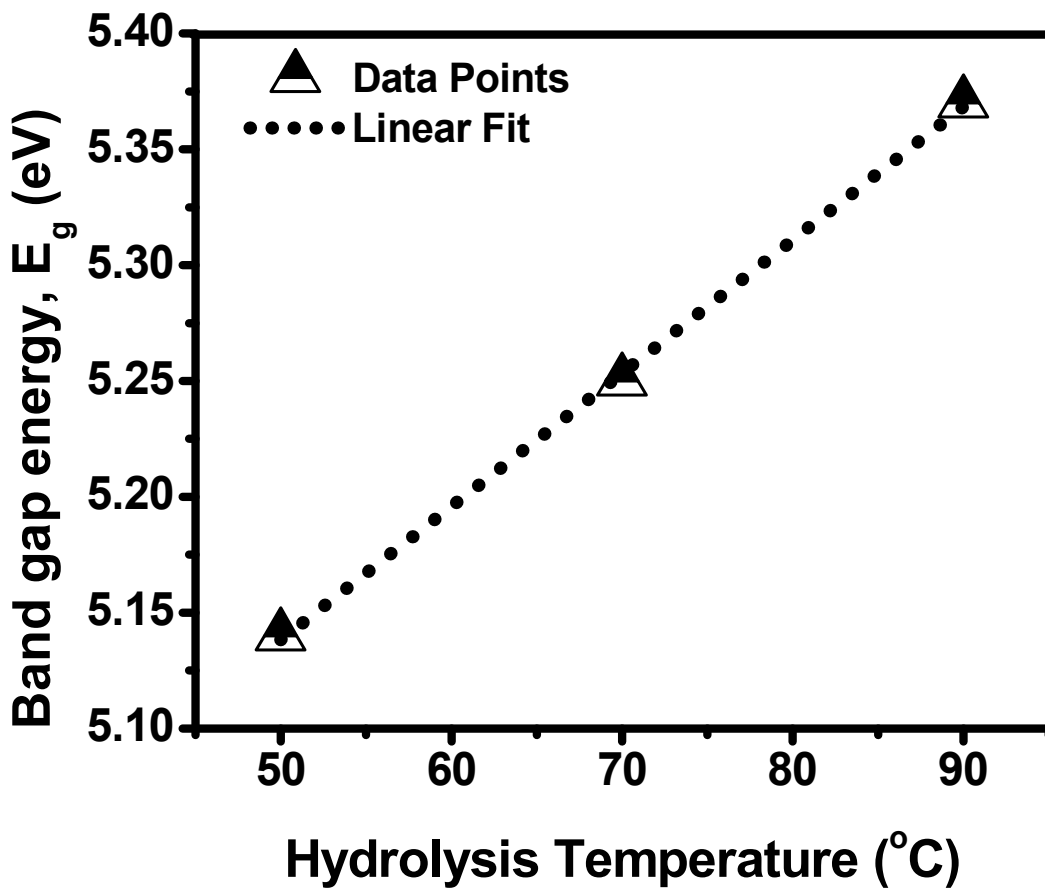
Figure 4. 4: The correlation between the band gap energy (eV) and the hydrolysis temperature (^{o}C) showing direct proportionality

4.4.2 The Effect of the Acid Concentration on Optical Band Gap Energy of CNCs

Figure 4.5: The *Tauc's* graphs for CNC samples prepared at hydrolysis temperature 50°C, hydrolysis time of 4 hrs and acid concentrations of 5%, 10% and 15% of H_2SO_4.
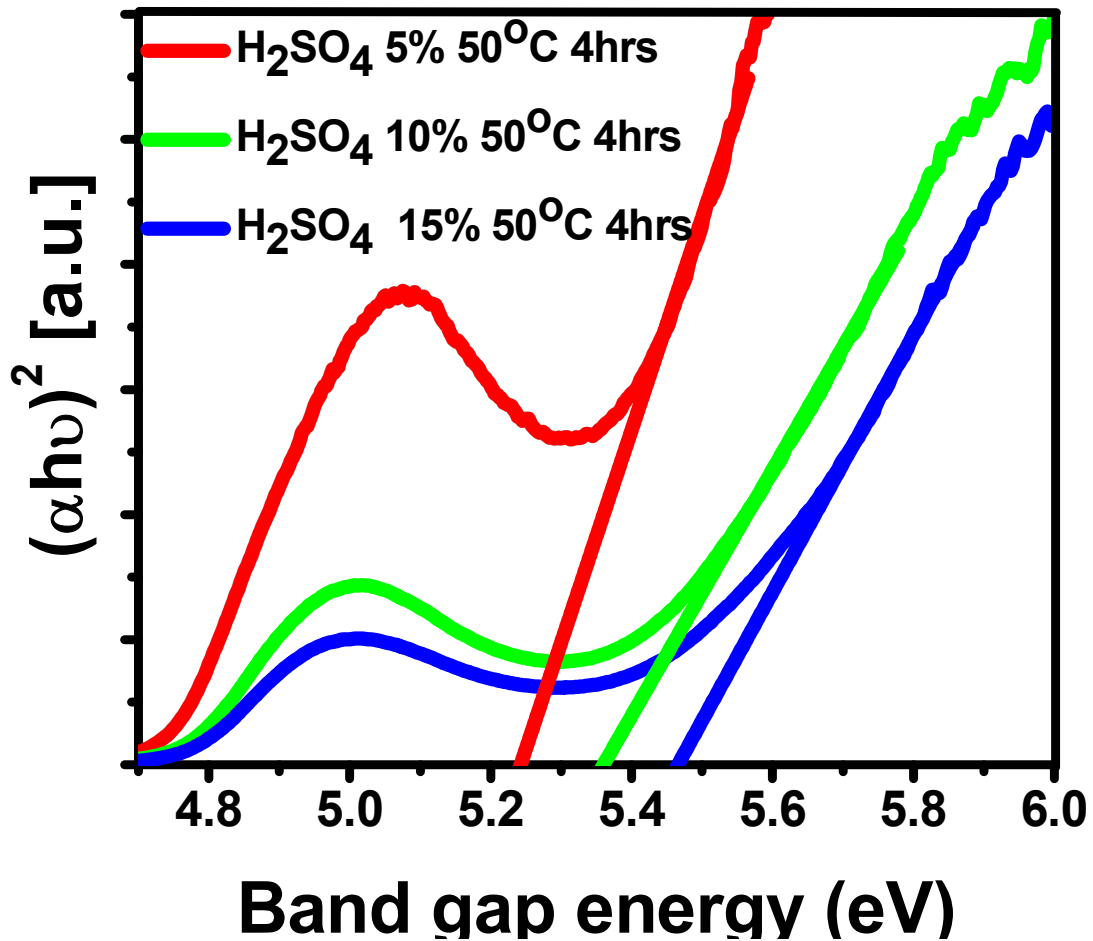
Figure 4. 5: The *Tauc's* graphs for CNC samples prepared at hydrolysis temperature 50°C, hydrolysis time of 4 hrs and acid concentrations of 5%, 10% and 15% of H_2SO_4

As seen from **Figure 4.6**, the band gap energy is seen to decrease with increased acid concentration. This has been supported by the fact that cellulose pulps usually have regions of high crystallinity (crystalline regions) and low crystallinity (amorphous regions). Increased acid concentrations led to preferentially removing the amorphous regions of the cellulose microfibrils as thus improving the optical absorbance thus lowered optical band gap.
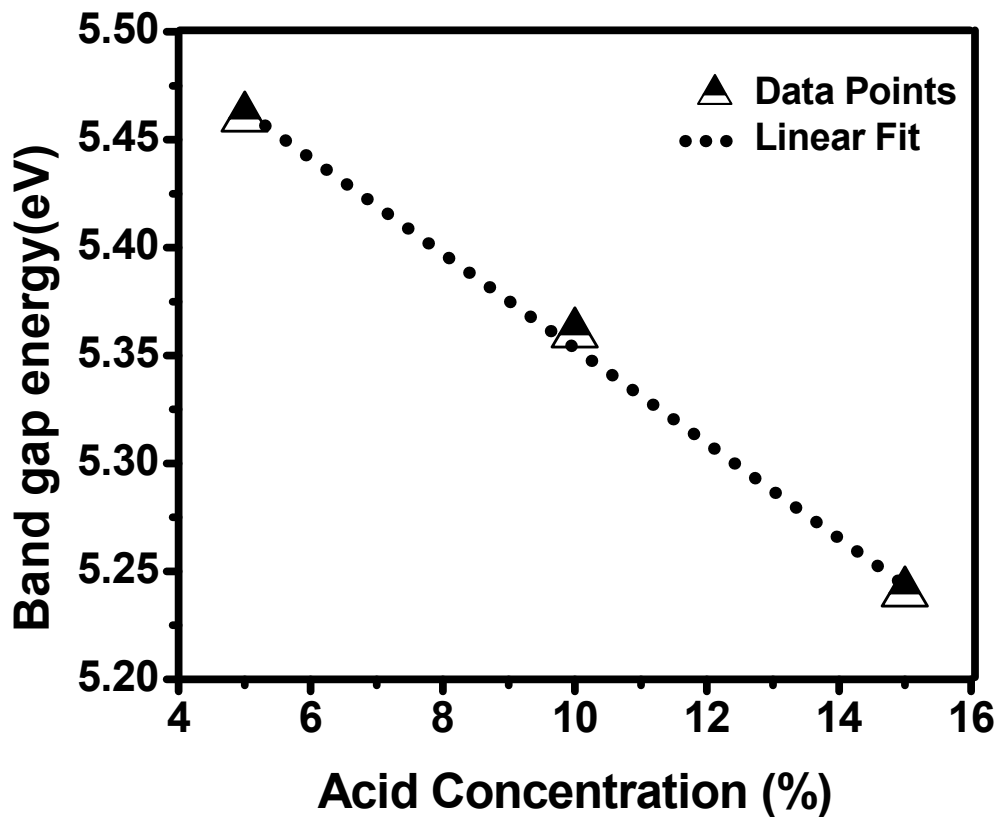
Figure 4. 6: The correlation between the band gap energy (eV) and the acid concentration showing inverse direct proportionality

4.4.3 The Effect of the Hydrolysis Time on Optical Band Gap Energy of CNCs

The graph below shows the Tauc graphs generated the data. From the *tauc* graph shown in **Figure 4.7**, the band gap energy for CNC samples prepared using 5% HNO_3 at 50°C with varying hydrolysis times of 2 hrs, 3 hrs and 4 hrs were found to be 5.303eV, 5.276 eV and 5.201 eV respectively. This shows an inverse proportionality in the band gap energy with the increase of time of hydrolysis.
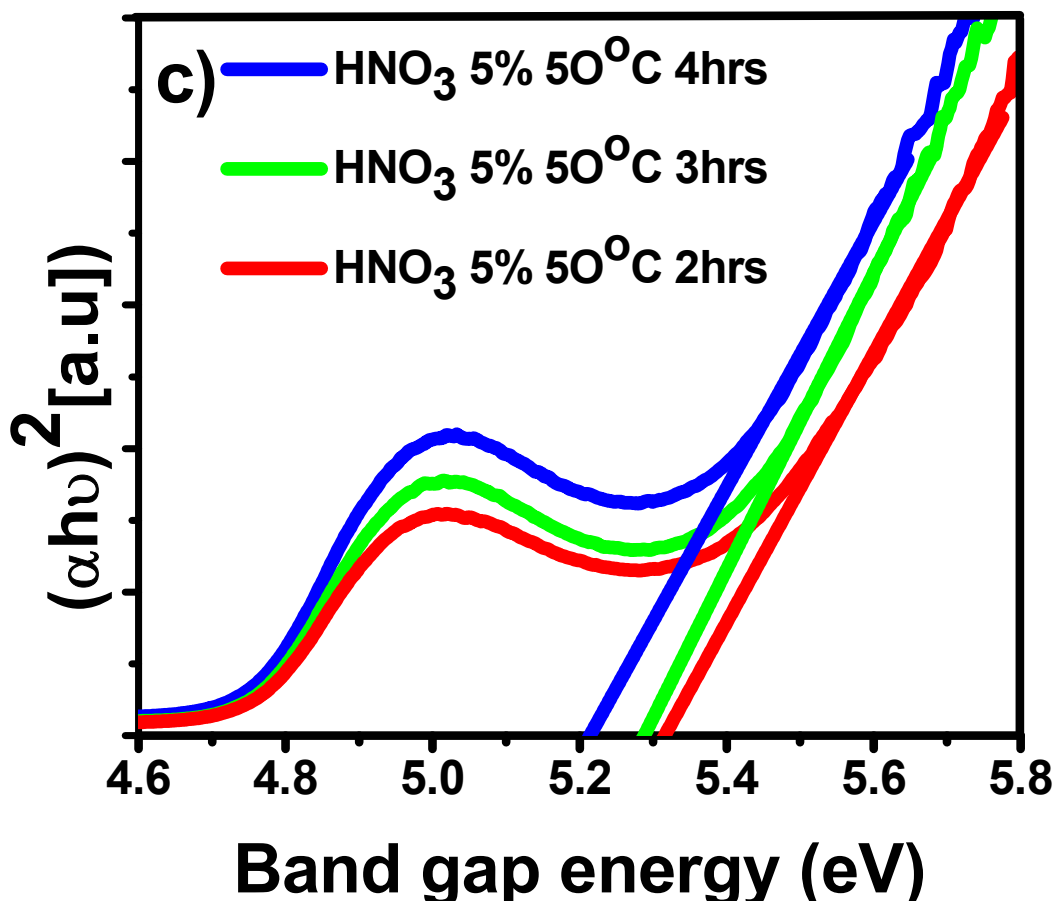
Figure 4. 7: The *Tauc's* graphs for CNC samples prepared using HNO_3 5% acid concentration, 50^oC hydrolysis temperature and hydrolysis time of 2 hrs, 3 hrs and 4 hrs

The graph in **Figure 4.8** shows the relationship between the band gap energy and the hydrolysis time depicting an inverse proportionality. Increase in hydrolysis reaction time leads to enhanced crystallinity thus leading to the red shift in absorbance peaks. As the hydrolysis time is prolonged, the acid eats more into the lignin and hemicellulose parts leaving more crystalline cellulose. This is seen in the decrease of the band gap energy with the increase in time of hydrolysis.
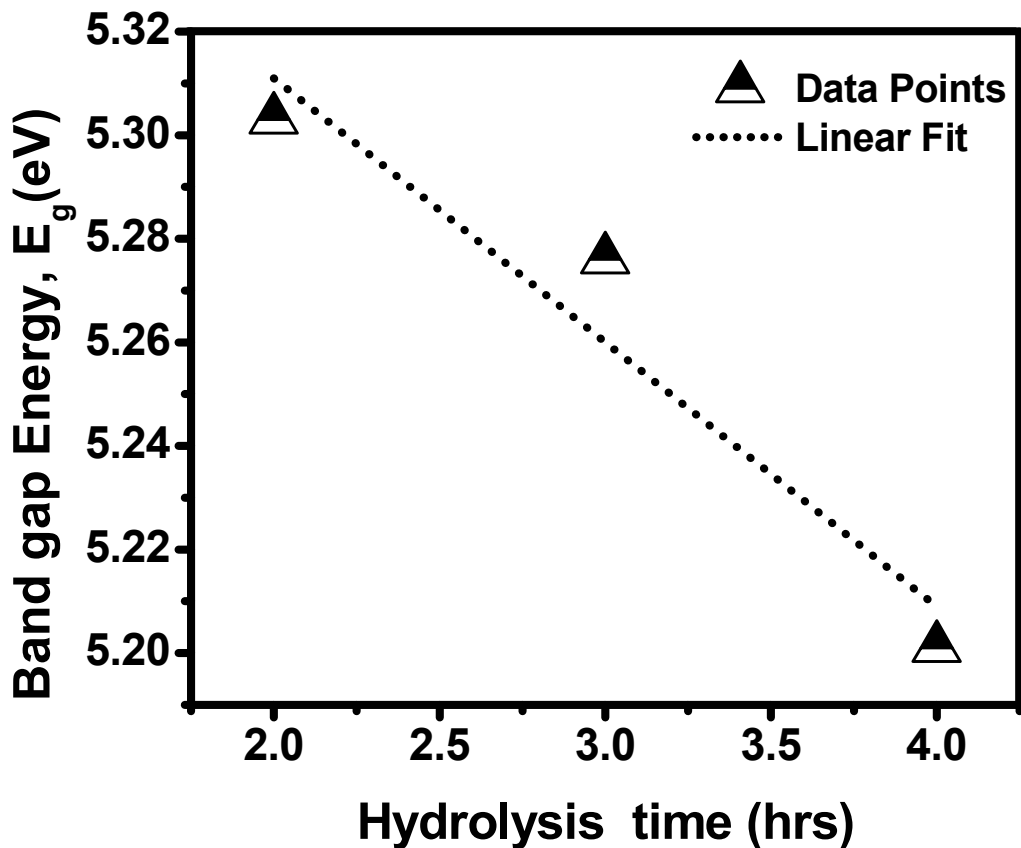
Figure 4. 8: The correlation between the band gap energy (eV) and the hydrolysis time showing inverse direct proportionality

We have so far observed that increase in the time of hydrolysis, hydrolysis temperature and acid concentration all lead decrease to the in Energy gap. We had earlier learnt in section 4.3 that the three parameters lead to increase in optical absorbance of the CNCs. Thus, our study confirms that increase in optical absorbance leads to decrease in bad gap energy of a material as held by the research study done by Ioelovich (169).

4.5 Fluorescence Properties of CNCs

4.5.1 Effect of Acid Type on the Fluorescence Properties of CNCs

Figure 4.9 shows the acid type dependent fluorescence spectra of CNCs prepared at 50°C for 2 hours hydrolysis time.
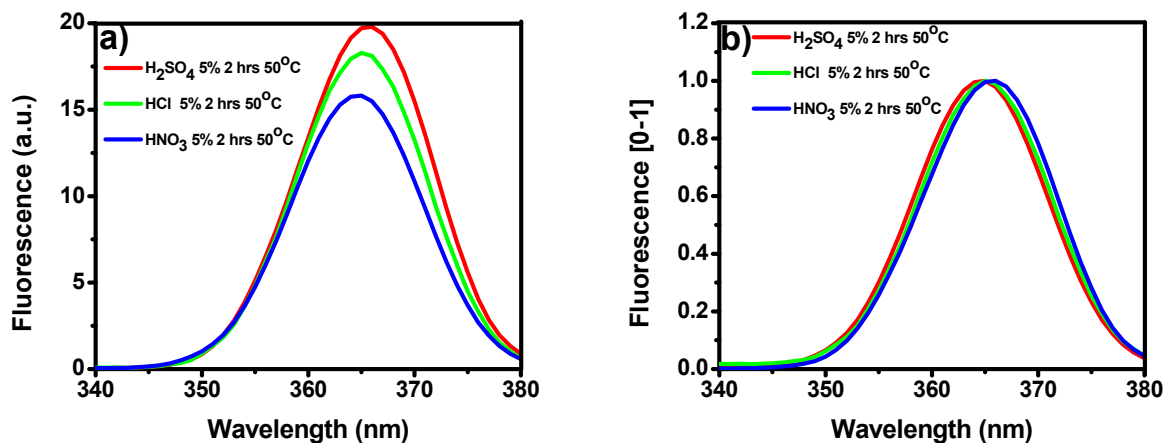
Figure 4. 9: Graphs of acid dependent fluorescence spectra (a) and its normalized counterpart (b) for CNCs prepared using 5% different acids at 50°C for 2hrs

4.5.2 Effect of Acid Concentration on the Fluorescence Properties of CNCs

Figure 4.10 shows the HNO_3 acid concentration dependent fluorescence spectra of CNCs prepared at 50°C for 2hours hydrolysis time.
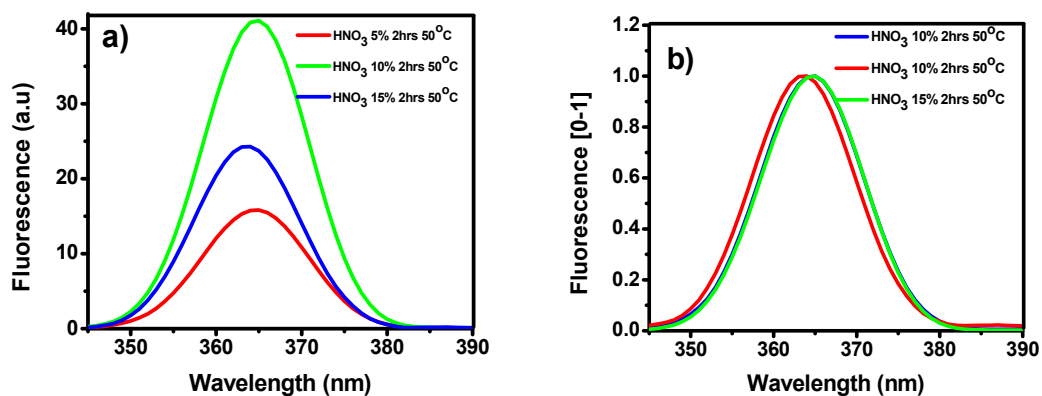
Figure 4. 10: Graphs of concentration dependent fluorescence spectra (a) and its normalized counterpart (b) for CNCs prepared using HNO_3 5%, 10% and 15% at 50°C for 2hrs

The normalized graph in **Figure 4.10 (b)** shows red shift of the fluorescence spectra with increase in the acid concentration. This suggests a more crystalline CNCs due to increased concentration of the acid as more unstable amorphous regions were able to be eliminated by the strong acids.

4.5.3 Effect of Hydrolysis Temperature on the Fluorescence Properties of CNCs

Figure 4.11 shows the temperature time dependent fluorescence spectra of CNCs prepared in HNO_3 5% for 2hours.
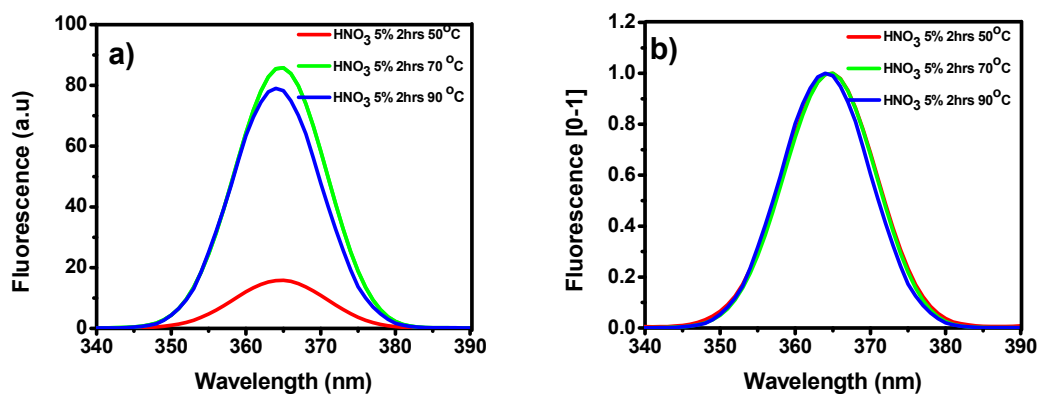
Figure 4. 11: Graphs of temperature dependent fluorescence spectra (a) and its normalized counterpart (b) for CNCs prepared using HNO_3 5%, at 50^oC, 70^oC, 90^oC for 2hrs

The normalized graph in **Figure 4.11 (b)** shows blue shift of the fluorescence spectra with temperature of hydrolysis. This suggests that the molecular orderings of the CNCs were adversely affected by the increase of the hydrolysis temperature as the acid ate much in to the crystalline regions of the CNCs.

4.5.4 Effect of Hydrolysis Time on the Fluorescence Properties of CNCs

Figure 4.12 shows the hydrolysis time dependent fluorescence spectra of CNCs prepared in HCl 5% at 50^oC for 2 hours.
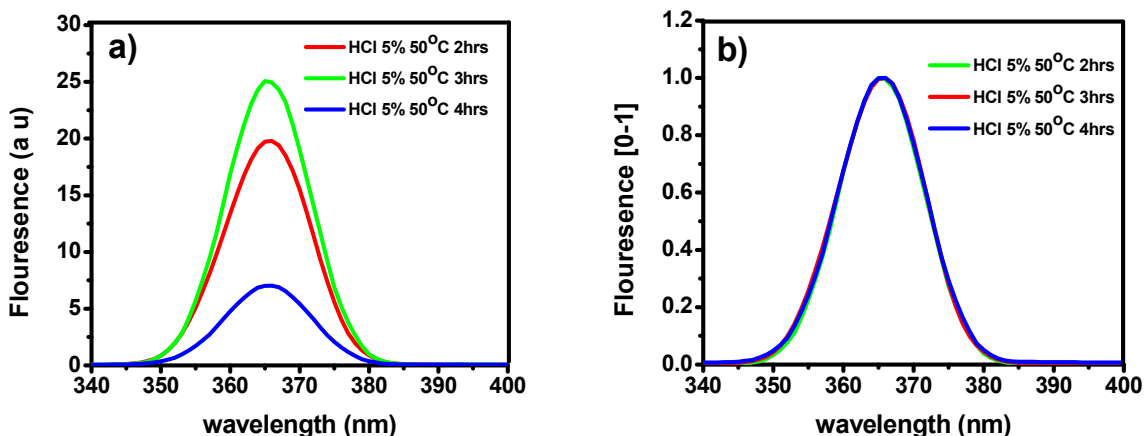
Figure 4. 12: Graphs of time dependent fluorescence spectra (a) and its normalized counterpart (b) for CNCs prepared using HCl 5% at 50°C for 2hrs, 3hrs and 4 hrs

The normalized graph in **Figure 4.12 (b),** shows no shift of the fluorescence spectra with time of hydrolysis. From the result, we conclude that the time of hydrolysis has no effect on the fluorescence of the resultant CNCs.

4.6 The Role of Acid Concentration on Band gap Shrinkage in Cellulose Nanocrystals

Studies have shown that acid hydrolysis of cellulose fibers yields highly ordered rod-like cellulose nanocrystals (CNCs) that are also known as nanocrystalline cellulose [145]. The intriguing ability of cellulose nanocrystals (CNCs) to self-organize into a chiral nematic (cholesteric) liquid crystal phase with a helical arrangement has attracted a significant interest in research. This is due to the arrangement that provides dried CNC films a photonic band gap. The CNC films in this way acquire attractive optical properties leading to possibilities for use in applications including mirrorless lasing and security papers. CNCs are highly crystalline with a length that runs up to several micrometers and a width of 2-20 nm [146]. Studies have shown that CNCs have high mechanical properties along the longitudinal direction with an estimated

modulus of elasticity of 138 GPa [147]. Further, it has been shown that the coefficient of thermal expansion of CNCs is less than $1 \times 10^{-7} \, °C^{-1}$ along the longitudinal direction which is as small as that of quartz [148]. These excellent features make cellulose microfibrils and nanofibers promising materials as the reinforcement in nanocomposites. Various methods can be used to obtain nano-cellulose, such as acid hydrolysis, ultrasonic technique, and enzymatic hydrolysis [149-152]. The method that is most widely used is acid hydrolysis [153]. This method is easy and fast to produce nanocellulose that has better properties.

Band-gap narrowing effects play an important role in bipolar devices with heavily doped regions [154]. The mechanism for band gap narrowing has been explained by the shifting of the valance band maximum and conduction band minimum of the material. The mechanism for band gap narrowing of doped samples is different in the nano and micron cases. Crystal size of the samples thus plays a very important part in the band gap change of materials. Potential fluctuations due to the random distribution of the impurities also lead to a broadening of the impurity band. The ionization level of the impurities is consequently reduced. Eventually the impurity band overlaps the conduction band or valence band, effectively narrowing the band gap. In this study, the fingerprint of the acid concentration during the hydrolysis process on the optical band gap of cellulose nanocrystals (CNCs) has been systematically studied.

Figure 4.13 shows the X-ray diffraction patterns of cellulose nanocrystals in hydrochloric acid of 5%, 10%, 15% concentration and hydrolysis done at temperatures of 50°C for 4 hours.
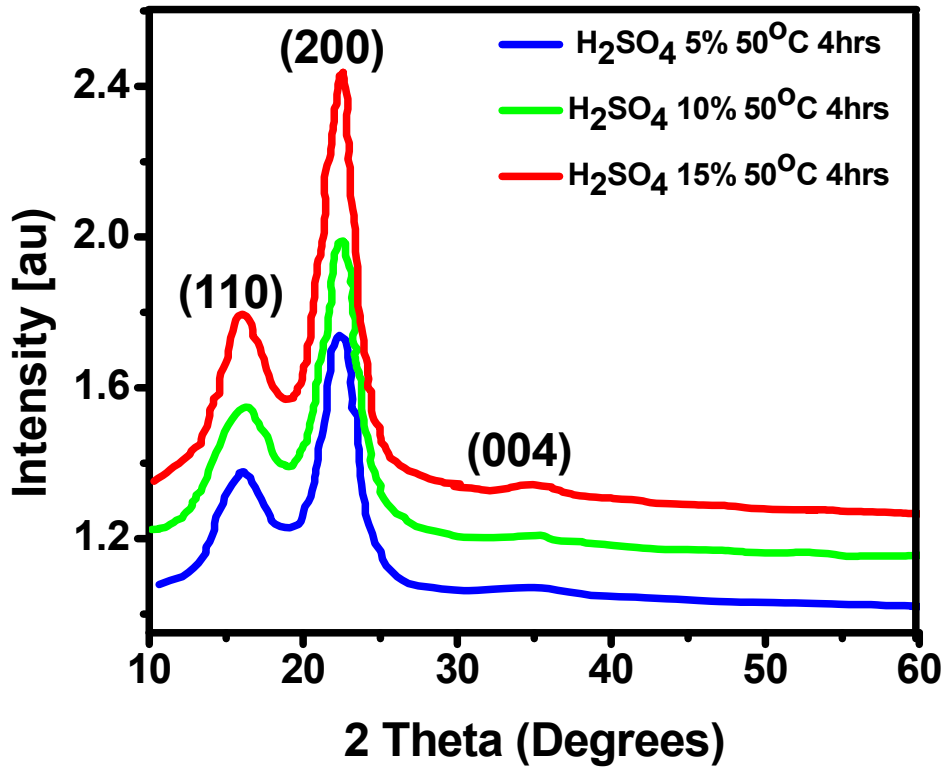
Figure 4. 13: Patterns of X-ray diffraction from samples prepared at 5%, 10%, 15% concentration and hydrolysis carried out at temperatures of 50°C for 4 hours

The grain sizes of the CNCs prepared at different hydrolysis temperatures were calculated using the *Scherrer* equation (4.1)

$$\text{Crystal size} = \frac{0.94\lambda}{\beta_{1/2}\cos\theta} \tag{4.1}$$

Where λ is the radiation wavelength, θ is the diffraction angle, and $\beta_{1/2}$ is the corrected angular width (in radians) at half maximum intensity. The results of crystal size are shown in **Table 4.4.**

Table 4. 4: The relationship between the hydrolysis temperature, the diffraction angle θ, the corrected angular width $\beta_{1/2}$ at half maximum intensity (in radians) and the grain size (nm)

Acid Concentration (%)	2Θ (degrees)	$\beta_{1/2}$ (radians)	Grain size (nm)
5	22.5	0.32	4.61
10	22.5	0.38	3.88
15	22.5	0.42	3.51

The table shows that the grain size (crystallite size) increased with decrease in acid concentration.

Figure 4.14 shows the absorbance spectra and the *Tauc's* plot of CNCs prepared using H_2SO_4 at 50°C for 4hrs with varying acid concentrations of 5%, 10% and 15% (b).
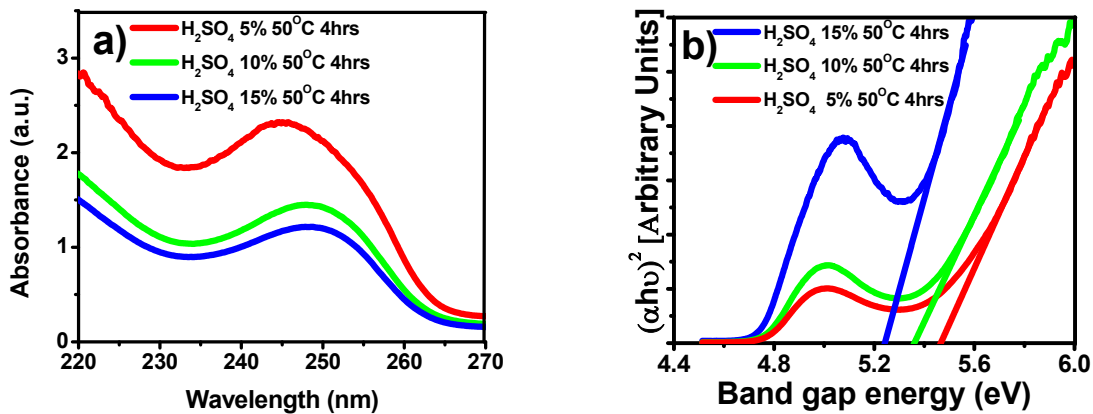
Figure 4. 14: The Absorbance spectra (a) and the *Tauc's* plot (b) of CNC samples prepared using H_2SO_4 at 50°C for 4hrs with varying acid concentrations of 5%, 10% and 15%

From the *Tauc* graph in **Figure 4.14 (b)**, the band gap energy for CNC samples prepared in HCl at hydrolysis temperature of 50°C at a constant hydrolysis time of 4 hrs but with varying acid concentration of 5%, 10% and 15% were found to be 5.098 eV, 5.358 eV and 5.468 eV respectively as depicted in **Table 4.5.**

Table 4. 5: The relationship between the hydrolysis temperature, the grain size (nm) and the band gap energy (eV)

Acid Concentration (%)	Grain size (nm)	Band gap energy (eV)
5	4.61	5.098
10	3.88	5.358
15	3.51	5.468

This indicates that there is an inverse proportionality in the grain size as you increase the concentration of the hydrolysis acid. The inverse proportionality is also seen between the band gap energy and grain size as depicted in **Figure 4.15**.
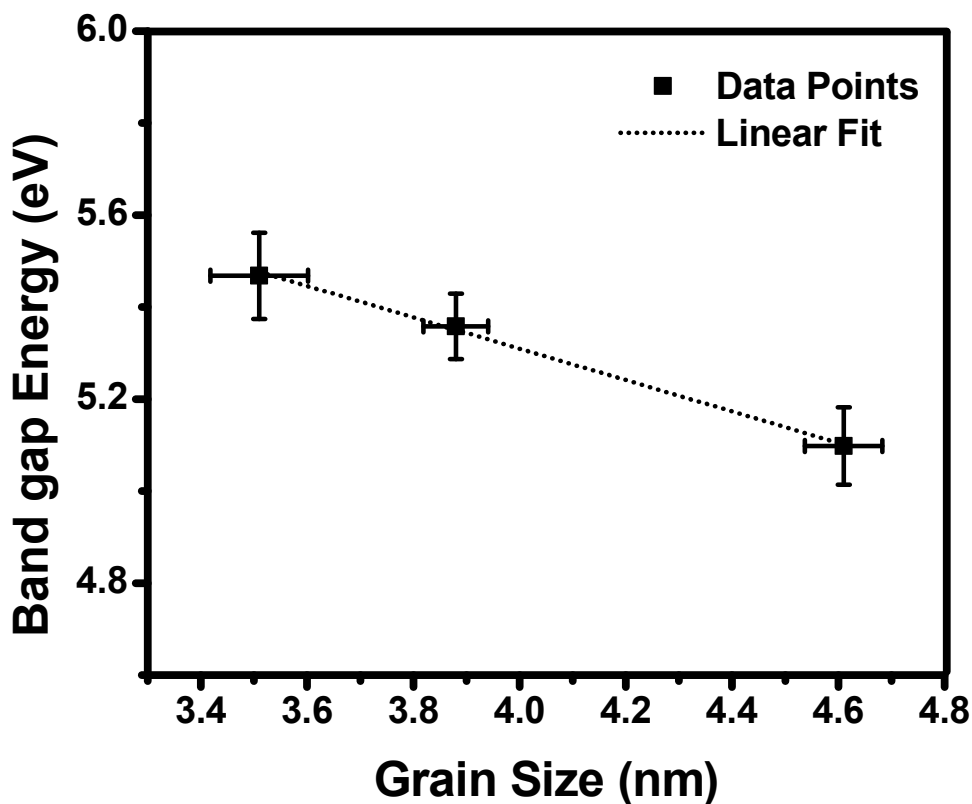
Figure 4. 15: Graph of band gap energy (eV) versus grain size (nm) showing a nearly inverse dependence

From this investigation, it was observed that increasing the acid concentration, the process was accompanied by reduction of the sizes of particles with simultaneous depolymerization of cellulose macromolecules. The intermolecular bonds between CNCs start rupturing and the particles move to the hydrolyzing solution hence reduction in grain size. The grain size was found to reduce with increase in HCl concentration. This can be explained by the fact that during the cellulose HCl hydrolysis, cellulose in amorphous region got hydrolyzed. As the hydrochloric acid concentration increased, cellulose crystalline regions were gradually swelled and more cellulose in crystalline regions reacted with the acid. Also, cellulose in amorphous regions got hydrolyzed and completely removed by the acid hydrolysis [155]. As a result, high crystallinity CNCs particles with reduced grain sizes formed. Interestingly, the band gap energy was found to

increase with decrease in the grain size. This fact confirms what is held in theory as can be corroborated by the study done Xurux T. *et al* [170].

This increase in band gap energy by decrease in grain size suggests increase in impurity concentration in spite of the increase of the overall crystallinity of the CNCs. If the crystallite size is large, there are more atoms and thus more bonding and antibonding atomic orbitals overlap that makes the gap between the band gap (valance and conduction band) to decrease. From the study, an increase in acid concentration has been found to lead to decrease in the grain (crystallite) whereas the band gap energy has been found to increase with increasing acid concentration. The optical band gaps of the CNCs have been found to decrease with the increase in crystallite size. This shrinkage of the band gap has been attributed to the increased impurity concentration leading to the narrowing of the band gap due to the emerging of the impurity band formed by the overlapped impurity states.

4.7 Hydrolysis Temperature Dependent on Structural, Optical Band Gap and the Associated Urbach Tail Energy of Cellulose Nanocrystals

In the present study, optical band-gap energy (E_g) of CNCs having different microstructures are investigated using an X-ray diffractometer (XRD) and UV-Vis spectrophotometer. The underlying dependence of microstructure on the evolution of E_g are addressed by assessing the associated Urbach energy tail (E_u). The correlation between the preparation techniques, the structure, the Optical Band Gap and the associated Urbach Tail Energy of the CNCs were mapped. The absorbance spectra were collected using Chary60 Shimadzu UV-Vis spectrophotometer transmission in the 200-500 nm range at the wavelength interval of 0.2nm. The Maximum absorbance wavelength measurements were read and recorded. The band gap energies were further calculated from *Tauc's* graphs that were generated from the absorbance spectral graphs. These optical measurement values were done for all the parameters used in the extractions and the results compared and evaluated.

4.7.1 Structural Analysis

Cellulose I polymorph has been shown to have both monoclinic and triclinic structure [156]. To investigate the crystalline structure of the fabricated cellulose nanocrystals, X-ray diffraction (XRD) analyses were performed. **Figure 4.16** show the X-ray diffraction patterns of samples prepared at 5% concentration and hydrolysis done at temperatures of 50°C, 70°C and 90°C for 2 hours.
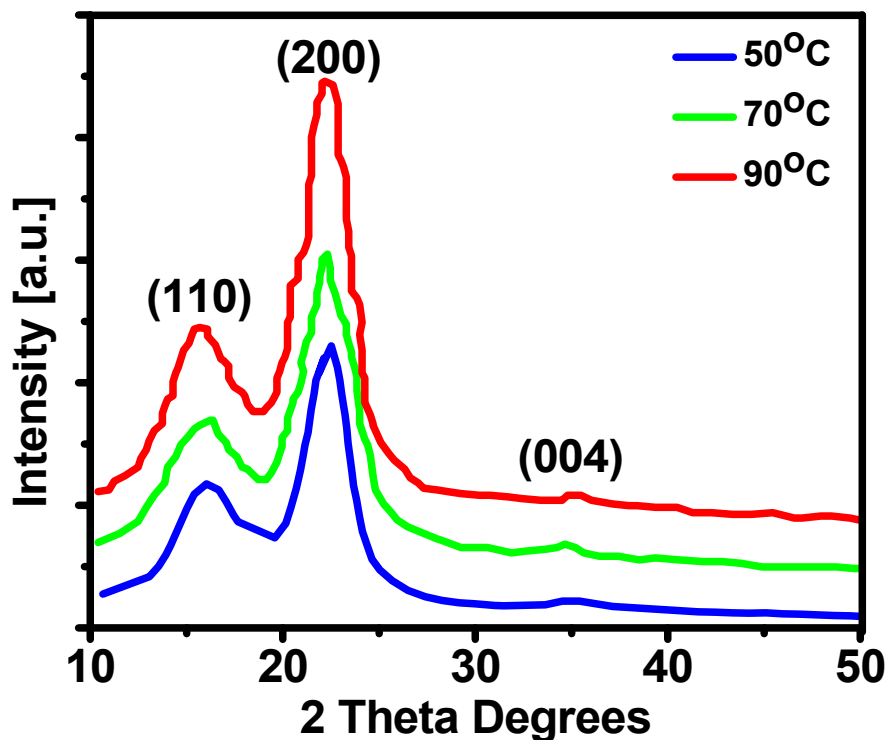
Figure 4. 16: X-ray diffraction patterns of samples prepared at 5% concentration and hydrolysis done at temperatures of 50°C, 70°C and 90°C for 2 hours

These samples indicate sharp diffraction peaks at 2θ around 16.5°, 22.5° and 34.5° corresponding to the (110) (200) and (004) lattice planes which are representing the typical cellulose I structure [157]. The crystallinity index for CNCs prepared at the different hydrolysis temperatures were calculated as explained above. The results of crystallinity indices are shown in **Table 4.6.**

$$\text{Crystallinity Index} = \frac{(I_{(200)} - I_{am})}{I_{(200)}} \, X \, 100\% \qquad (4.2)$$

Table 4. 6: The table of hydrolysis temperature (^{o}C) and associated Crystallinity indices (%)

Hydrolysis Temperature (^{o}C)	Crystallinity Index (%)
50	57.9
70	58.2
90	60.3

The results show that the crystallinity index of the fabricated CNCs increased with the hydrolysis temperature. The crystallinity increased because high hydrolysis temperatures effectively removed the amorphous phase, lignin and hemicelluloses leaving more crystalline phases. The grain sizes of the CNCs prepared at different hydrolysis temperatures were calculated by using the **Scherrer equation** as shown in equation 4.1.

Table 4. 7: The relationship between the hydrolysis temperature, the diffraction angle θ, the corrected angular width $\beta_{1/2}$ at half maximum intensity (in radians) and the grain size (nm)

Hydrolysis Temperature (^{o}C)	2Θ (degrees)	$\beta_{1/2}$ (radians)	Grain size (nm)
50	22.5	0.39	21.70
70	22.5	0.42	20.12
90	22.5	0.44	19.23

The table shows that the grain size decreased with increase in hydrolysis temperature. This decrease suggests increase in impurity concentration in spite of the increase of the overall crystallinity of the CNCs.

4.7. 2 Optical Analysis

The representative absorbance spectra of cellulose nanocrystals prepared using 5% HCl for 2 hours with varying hydrolysis temperatures of 50°C, 70°C and 90°C as displayed in the graph in **Figure 4.17**. Figure (a) shows the raw absorbance spectra and its corresponding normalized counterparts in Figure (b).

113
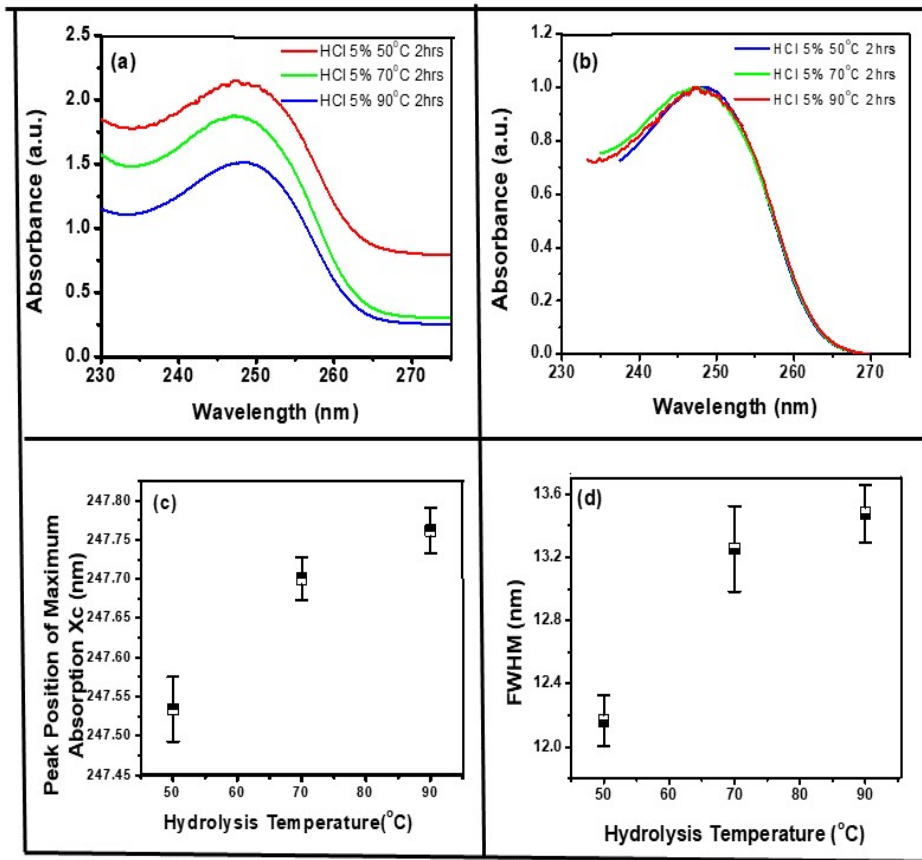
Figure 4. 17: The raw absorbance spectra (a), normalized spectra (b), peak wavelength that corresponds to maximum absorbance (c) and the Full Width at Half Maximum of the absorption peak of CNC samples prepared using 5% HCl for 2hrs with varying hydrolysis temperatures of 50°C, 70°C and 90°C

As shown in **Figure 4.17 (c),** the maximum absorbance wavelengths for CNCs were found to be 247.522 nm, 247.709 nm and 247.762 nm for temperatures of 50°C, 70°C and 90°C respectively. This is an indicator that increases in hydrolysis temperature leads to the red shift of the maximum absorption band of the CNCs. This suggests more ordered (crystalline) absorbers. On the other hand the values for the FWHM were found to be 12.17 nm, 13.26 nm and 13.48 nm for temperatures of 50°C, 70°C and 90°C respectively as shown in **Figure 4.17 (d)**. This trend shows increase of the absorption band. More absorbers were yielded by increased hydrolysis temperature thus the band spread.

114

In this study, fingerprints on the hydrolysis parameters on the optical band gap energy of the fabricated CNCs have been systematically investigated. The band gap energy for CNC samples prepared using 5% HCl for 2 hours with varying hydrolysis temperatures of 50°C, 70°C and 90°C were found to be 5.31 eV, 5.22 eV and 5.14 eV respectively. This shows a near inverse proportionality in the band gap energy with the increase of temperature of hydrolysis as depicted in **Figure 4.18 (b).**
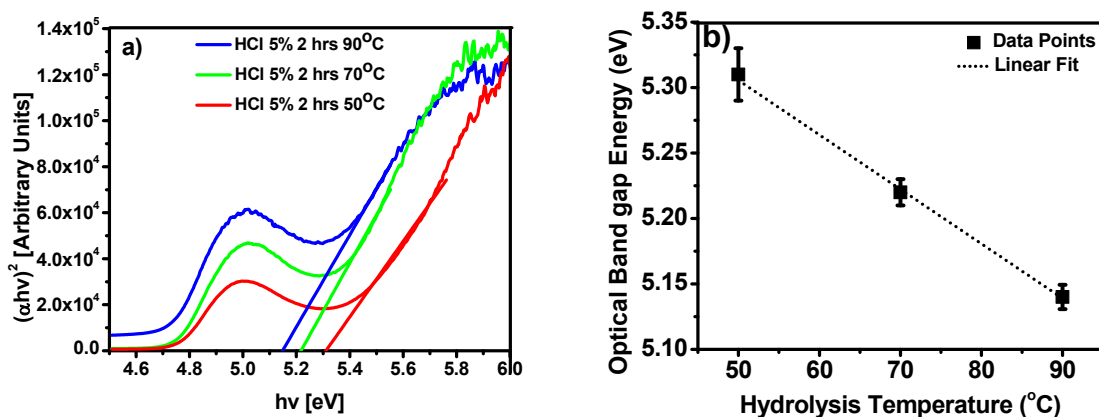
Figure 4. 18: The generated *Tauc* graphs (a) and a graph of band gap energy E$_g$ versus hydrolysis temperature (b) for CNC samples prepared using 5% HCl for 2 hours with varying hydrolysis temperatures of 50°C, 70°C and 90°C

The increased hydrolysis temperatures led to preferentially removing the amorphous regions of the cellulose CNCs as thus improving the optical absorbance thus lowered optical band gap. The decreased optical band gap with increased hydrolysis temperature suggests increased crystallinity of the CNCs. This is in agreement with what was observed in the values of crystallinity obtained by performing structural analyses. However, decrease in grain sizes was observed suggesting increased impurity concentrations.

By plotting a graph of hydrolysis temperature versus optical band gap energy, we can estimate the hydrolysis temperature at which the optical band gap will be ideally zero (y-intercept) as shown in **Figure 4.19.** This was found to be 1297.6°C as depicted in the equation below.

$$T_{hydrolysis} = -235 E_g - 1297.6\,^{o}C$$

(4.3)

This shrinkage of the band gap occurs when the impurity concentration is particularly high and it is called the band gap narrowing effect which is ascribed to the emerging of the impurity band formed by the overlapped impurity states.
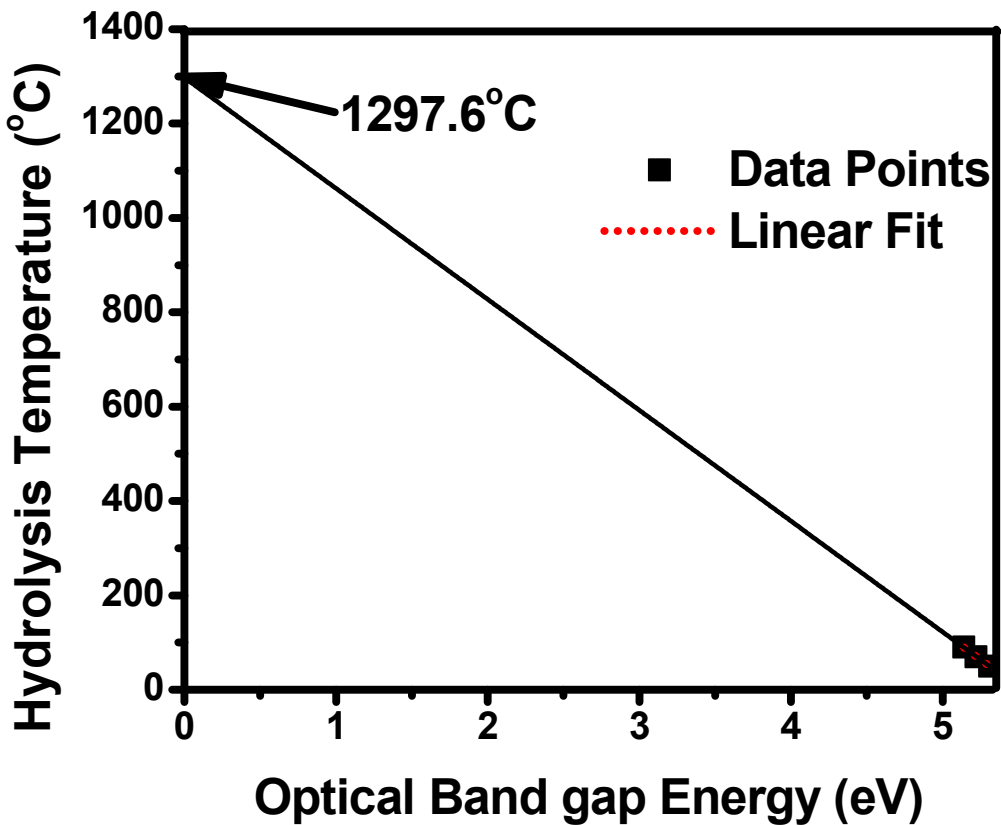
Figure 4. 19: The graph of hydrolysis temperature dependent optical band gap energy showing an inverse dependence

4.7.3 Urbach Tail Energy (E_u)

Generally, in optical absorption, near band edges, an electron from the top of the valence band gets excited into the bottom of the conduction band across the energy band gap [158]. During this transition process, if these electrons encounter disorder, it causes density of their states ρ(hν), where hν is the photon energy, tailing into the energy gap. This tail of ρ(hν) extending into the energy band gap are the localized defect states in an optical band gap region and are represented by the Urbach energy E_u which is responsible for the formation of absorption tail in the absorption spectra. Consequently, absorption coefficient α(hν) also tails off in an exponential manner as shown in equation (4.4).

$$\alpha = \exp\alpha_o\left(hv/E_u\right)$$

(4.4)

The energy associated with this tail is referred to as Urbach energy and can be calculated by the following equation:

$$\ln\alpha = \ln\alpha_o + \left(hv/E_u\right)$$

(4.5)

Where α_o is a constant, 'hν' is the photon energy and E_u is the Urbach energy and denotes an energy which is constant or weakly dependent on temperature and is often interpreted as the width of the tail of localized states in the band gap [159-160]. In **Figure 4.20,** region-U is the representative of this phenomena and corresponding range of α follows equation (4.4). The *α* versus *hv* behavior of CNCs prepared at varied temperatures are shown in **Figure 4.20**. The important features of the figure are classified into two types of absorptions [161-164]. First is the region-U where α is controlled by the transitions from the localized tail states above the valence band to the extended states in the conduction band and/or from the extended states in the valence band to the localized states below the conduction band [162-164]. In this region, the spectral dependence of α follows the Urbach rule. Second is the region-T which represents the range of α governed by the optical transitions from one extended state to another extended state. Most of the amorphous and nanocrystalline materials follow *Tauc's* relation in this region. Thus, E_g is calculated by *Tauc's* plot in this region-T.
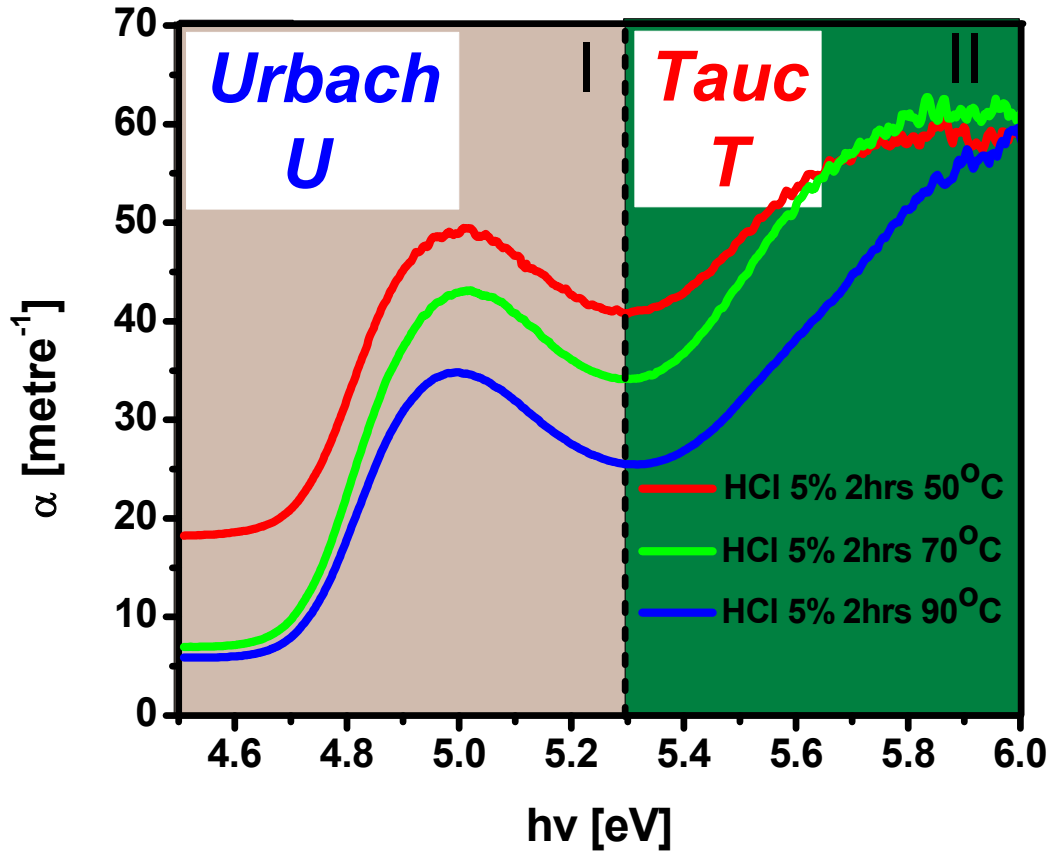
Figure 4. 20: Absorption coefficient (α) as a function of photon energy (hν) for CNC samples prepared using 5% HCl for 2hrs with varying hydrolysis temperatures of 50°C, 70°C and 90°C

The Urbach energy is estimated by plotting *ln(α)* versus hν and fitting the linear portion of the curve with a straight line. The exponential tail appears because disordered and amorphous materials produce localized states extended in the band gap is the absorption coefficient.

$$\alpha = \frac{2.303}{d} XAbsorbance$$

(4.6)

The E_u is estimated from $\ln \alpha$ versus h ν plot from which the reciprocal of the slope obtained by fitting the linear part of the curve gives the value of E_u.

$$E_u = \frac{1}{Slope}$$

<div align="right">(4.7)</div>
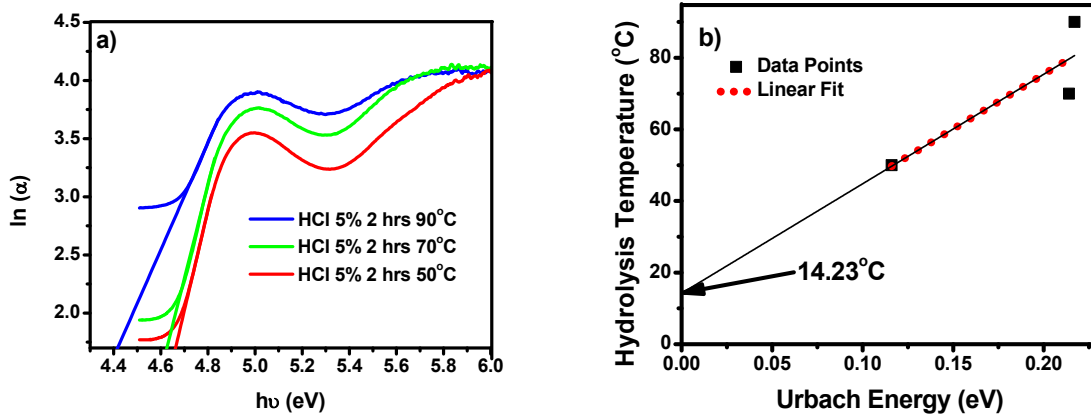
Figure 4. 21: A plot of $\ln\alpha$ versus $h\upsilon$ (a) and Urbach Energy (eV) versus the hydrolysis temperature (b) for CNC samples prepared using 5% HCl for 2 hours with varying hydrolysis temperatures of 50°C, 70°C and 90°C

By performing a linear fit, we find that $T_{hydrolysis} = 305.84E_u + 14.23^oC$. This equation shows that the Urbach energy is absent when hydrolysis is done at 14.23°C. This is the energy when the localized defect states in an optical band gap region are completely screened.

To estimate the net contribution of structural and thermal disorder in the micostructure to account for the reduction in optical band gap of CNCs, the band gap energy, $E_{g,}$ and the associated Urbach energy E_u are shown in **Table 4.8**.

Table 4. 8: Comparison of optical band gap energy (E_g) and Urbach energy (E_u) for CNCs fabricated at different hydrolysis temperatures

Hydrolysis Temperature (^{o}C)	Band gap Energy E_g (eV)	Urbach Energy E_u (eV)
50	5.31	0.116
70	5.22	0.124
90	5.14	0.217

If a plot of E_g versus E_u is done, it is found to be linear as is shown in **Figure 4.22**. When fitted with a straight line, its intercept gives the minimum possible value of E_g ~5.43 eV which can be considered to represent that value of E_g when there is no disorder in the CNCs microstructure. The decrease in the optical band gap with increase in hydrolysis temperature may be attributed to the increase in CNCs crystallinity. However, the increase observed in the Urbach energy can be attributed to decrease in grain size that means increase in structural disorder.
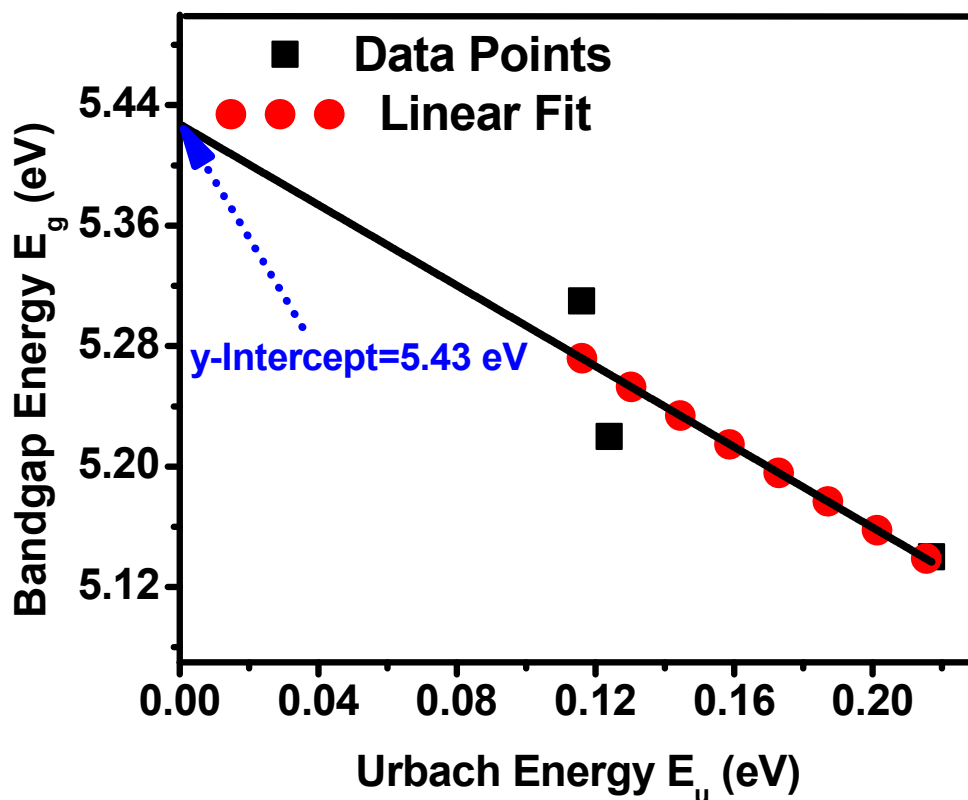
Figure 4. 22: Comparative variation of E_g with net E_u. When fitted with a straight line, intercept of the linear fit ($\sim$ 5.43 eV) represents the optical band gap energy of the films when there is no disorder in their microstructure

At increasing the hydrolysis temperature, the process is accompanied by reduction of the sizes of particles with simultaneous depolymerization of cellulose macromolecules. The intermolecular bonds between CNCs start rupturing and the particles move to the hydrolyzing solution. Thus, the more Urbach energy, the lower the energy gap and vice versa. Urbach energy expresses the degree of defects in the system, and thus the more Urbach energy, the defects are increasing, and therefore we find that the degree of defects or disorders, in general, is decreased in the crystallized system. The study has therefore confirmed the underlying principle of inverse proportionality between the Urbach energy and band gap energy as reported by Neha Sharma and co-workers in their article entitled Optical band gap and associated band-tails in nanocrystalline

AlN thin films grown by reactive IBSD at different substrate temperatures [171]. From our results, the peak wavelength for maximum absorption of cellulose sourced from water hyacinth was in the range of 244 nm to 249 nm. This range is in close agreement with the theoretical value of 260 nm of cellulose [165]. The calculated band gap energy for cellulose was also found to be in the range of 5.1 eV to 5.4 eV. This is also in close agreement with the value of 4.8eV that was found by Simao and coworkers in their study of the optical and mechanical properties of nano fibrillated cellulose [166]. This red-shift of the optical absorption edge suggests increased crystallinity due to improved long-range order of the cellulose atoms within the nanocrystal.

Thus, increase in the hydrolysis temperature directly enhances the hydrolysis process, as the cellulose is hydrolyzed more with increase in temperature [167]. Increased temperatures lead to enhanced crystallinity thus leading to the red shift in absorbance peaks. As the hydrolysis temperature is increased, the acid eats more into the lignin and hemicellulose parts leaving more crystalline cellulose. This is seen in the increase of the absorption peak wavelengths with the increase in temperature of hydrolysis and the crystallinity index. The band gap energy is equally seen to decrease with increased hydrolysis temperature. This has been supported by the fact that cellulose pulps usually have regions of high crystallinity (crystalline regions) and low crystallinity (amorphous regions). Thus, the increased temperatures led to preferentially removing the amorphous regions of the cellulose microfibrils as thus improving the optical absorbance thus lowered optical band gap. The decreased optical band gap with increased hydrolysis temperature suggests increased grain sizes and crystallinity of the CNCs. The exponential tails in the plots of $\ln \alpha$ versus E_u are associated with low crystalline films, and disordered amorphous materials because of localized states. This has been found to decrease with increase in hydrolysis temperature. From a plot of E_g verses E_u, the optical band gap energy of the CNCs when there is no disorder in their microstructure was found to be ~5.43 eV. The CNCs were found to have zero optical band gap energy when hydrolysis is done at ~1297.6°C. The hydrolysis temperature dependent increase in the electronic disorder in the crystal (Urbarch energy) with increase in associated band gap energy has thus been estimated to account for the optical disorder in the CNCs.

From this study, we have investigated the impact of the acid hydrolysis parameters on the optical properties of CNCs extracted from water hyacinth. By applying the *Tauc model*, the band gap energy E_g of the samples has been determined. From the absorbance spectra obtained, it was observed that increase in acid hydrolysis reaction time increases the values of the peak wavelength for maximum absorption, X_c and that of the full wave at half maximum (FWHM). Interestingly, increase in acid concentration also increases X_c. The Urbach energy increased while the optical band gap decreased with increase in hydrolysis temperature. From a plot of E_g verses E_u, the optical band gap energy of the CNCs when there is no disorder in their microstructure was found to be ~5.43 eV. In addition, the study has shown that the Urbach energy is missing when hydrolysis is done at a temperature of 14.23°C. This is the energy when the localized defect states in an optical band gap region are completely screened. The hydrolysis temperature dependent increase in the electronic disorder in the crystal (Urbach energy) with increase in associated band gap energy has in thus way been estimated to account for the optical disorder in the CNCs. It was further observed that increase in hydrolysis temperature led to decrease in band gap energy (E_g). It can thus be concluded that the optical properties of cellulose nanocrystals can effectively be tuned by adjusting the hydrolysis temperature during the preparation process.

4.8 The Degree of Alignment and the Piezoelectric Sensing Effect of CNCs

4.8.1 Sensor Sensitivity Measurements

The degree of alignment of the CNCs within the films as a function of voltage and frequency is studied. Variations in the parameters allow control of the piezoelectric behavior of the system and produce a large piezoelectric response. The sensitivity measurements on CNC film sensors fabricated from CNCs extracted from water hyacinth but with different crystallinity indices is investigated. The degree of polarization of the CNC films and thus the orientation of crystals of the CNC films have been varied leading to remarkable variations of piezoelectricity.

4.8.2 Factors Affecting the Sensitivity of CNC based piezoelectric sensors.

One of the factors that affect the piezoelectric effect of CNC film is the alignment of the CNCs. It is further affected by the dipolar orientation and the degree of crystallinity of CNCs in the

films. The piezoelectricity of CNC particles is caused by the electric dipole moments which occur within the particles which in turn is associated with randomly distributed carbon atoms found in the anisotropic crystalline structure of cellulose I. the occurrence of the electric dipoles moments is further influenced by the change in polarization density of charged atomic groups under the influence of the electric fields within the crystalline structure. The naturally long-range ordered polymer chains and its polarizability are responsible for the observed high shear piezoelectricity. This study was dedicated to investigating the effect of the applied voltage and the frequency on the piezoelectric effect of the aligned CNC films.

4.8.2.1 The A.C. Voltage Applied

Figure 4.23 shows the variation of the sensitivity of the fabricated CNC sensor with the applied voltage.
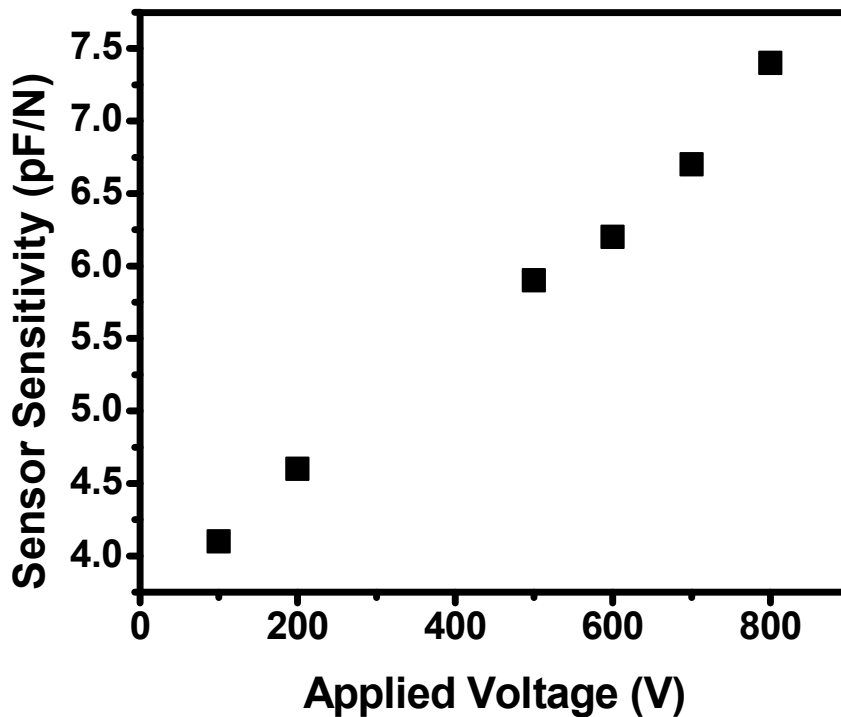
Figure 4. 23: The applied voltage dependent sensitivity of the CNC sensor

It has been observed that the CNCs alignment increases with the applied voltage. The electric field alignment process is a two-staged procedure. The first stage is whereby the cellulose nanocrystals make a gyratory motion as they get aligned by the electric field. The second stage is the inter-interaction of CNC particles forming chains which occur parallel to the electric field lines. Another notable observation made is that increasing the duration of the application of the electric field leads to increase in thickness and length of the CNC chains formed. The sensitivity of the CNF films increases after polarization, since the polarization process exposes the film to a high electric field thereby generating piezoelectric properties. Furthermore, the polarization of the CNF film makes the crystals of the films become more aligned leading to a remarkable increase of piezoelectric effect courtesy of the large piezoelectric coefficient of the CNCs.

4.8.2.2. The Frequency of the Signal Generator

Figure 4.24 shows the variation of the sensitivity of the fabricated CNC sensor with the frequency. It has been observed that the CNCs alignment increases with the frequency.
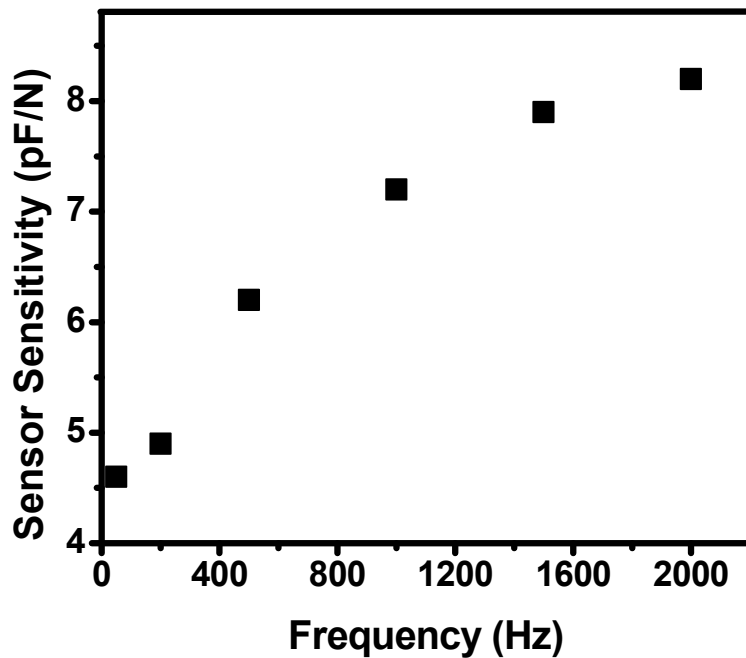
Figure 4. 24: The Frequency dependent sensitivity of the CNC sensor

Higher frequencies enhance orientations of the CNCs within the films thus leading to improved piezoelectric effect. It has been observed that the CNCs alignment increases with the applied frequency. The high frequency increases the velocity of the vibrations of the crystals making them to change their diverse orientations to common vector. The increased particle ordering leads to increased crystallinity index thereby increasing the overall sensitivity of the sensors.

CHAPTER FIVE

CONCLUSION AND RECOMMENDATIONS

5.1 Conclusions

From the research study, cellulose nanocrystals were extracted from water hyacinth that was harvested from Usenge beach, Lake Victoria, through alcohol pretreatment process that was followed by a parameterized acid hydrolysis mechanism. The prepared CNCs films were then subjected to a series of characterization techniques. From the absorbance spectroscopy, the increase in acid hydrolysis reaction temperature, hydrolysis time span and concentration of the acid all lead to the increase in the values of the peak wavelength for maximum absorption, X_c, and the full wave at half maximum (FWHM). The study further revealed that the increase in all these hydrolysis parameters all lead to shrinkage of the band gap. The shrinkage in the band gap is a clear indicator of the improved molecular ordering in the CNC films. This shows that increase in the values of the acid hydrolysis parameters led to increase in the degree of alignment of the crystals within the films which lowered the band gap energy since the electrons could easily be excited from the ground state to the excited state. The Urbach energy was found to be inversely proportional to the band gap energy. It was further learnt that the Urbach energy increased while the optical band gap decreased with increase in hydrolysis temperature. The increase in Urbach energy with decreased band gap was evidence that the density of state that was associated with the transition of the electrons from ground to excited state was increased. This further explains the fact that the, crystallinity index was improved, a sign of increased degree of alignment of the molecules of the films.

A graph of Urbach energy verses the Band gap energy showed an inverse proportionality relation between the two quantities, a fact that is supported by the research study conducted by Neha Sharma *et al* [171], in which Aluminium Nitrate thin films were used. From the graph the optical band gap energy of the CNCs when there is no disorder in their microstructure was found to be ~5.43 eV. Further, we have shown that the Urbach energy is absent when hydrolysis process is done at $14.23^{o}C$. From the fluorescence spectroscopy, the study showed that increase in

temperature of hydrolysis led to blue shift in the peak fluorescence wavelength. However, increase in the acid concentration led to a red shift. Interestingly, the timespan of the hydrolysis does not affect the fluorescence of the CNCs films.

From the XRD measurements, it was learnt that there is an inverse proportionality in the grain size with the concentration of the hydrolysis acid. The inverse proportionality is also seen between the band gap energy and grain size. From the investigation done, it was observed that by increasing the acid concentration, the sizes of particles were reducing due to simultaneous depolymerization of cellulose macromolecules. Interestingly, the band gap energy was found to increase with decrease in the grain size. This increase suggests increase in impurity concentration in spite of the increase of the overall crystallinity of the CNCs. The results also showed that the crystallinity index of the fabricated CNCs increased with the hydrolysis temperature. This was attributed to the fact that high hydrolysis temperatures effectively removed the amorphous phase, lignin and hemicelluloses leaving more crystalline phases. By use of Scherrer's equation the study revealed that the grain size decreased with increase in hydrolysis temperature, a fact suggesting that there is increase in impurity concentration in spite of the increase of the overall crystallinity of the CNCs. After the characterization procedure, the CNC samples were used to design and fabricate a piezoelectric sensor. The sensor was assembled through an electric field assisted convection shear method. The piezoelectric effect of the electric field assisted convective shear assembled CNCs were successfully studied. The effect of the applied voltage and the frequency has been mapped. The piezoelectric sensors were fabricated from CNC films. The sensitivity of fabricated sensors was measured using the fabricated measurement setup. From the study, a high degree of CNC orientation in the films is found to be a key characteristic for the piezoelectric response. The highly ordered crystals within the films become more sensitive to any application of external stress which would attempt to disorient them, thereby increasing their piezoelectric response. The amount of applied voltage and the frequency have been found to increase the degree of the orientation/alignment of the CNCs within the films hence leading to enhanced piezoelectric response. The orientation of crystalline CNC regions inside the films leads to a remarkable increase of piezoelectric effect due to the large piezoelectric coefficient of the CNCs. Thus, functional piezoelectric sensors can be fabricated

from CNF film. The study has therefore shown that increase in the three hydrolysis parameters; time of hydrolysis, temperature and acid concentration all lead to increase in the increased alignment of the crystals of the prepared CNCs extracted from water hyacinth. These further impact on the optical properties of the CNCs and also increase the sensitivity of the fabricated piezoelectric sensors. Thus the study unveiled a significant correlation between the degree of alignment of the crystals and the opto-piezoelectric properties of the cellulose nanocrystals fabricated from water hyacinth.

5.2 Recommendations

This study has embarked on the study of the impact of the degree of linearity of the cellulose nanocrystals on the piezoelectric effect of the CNC-based films. However, the study has not delved into the consideration of the nonlinearity and hysteresis of the sensors. It is our recommendation that the nonlinearity of the sensors should be investigated by measuring the magnitude of the surface charge density generated by the sensor with respect to the applied dynamic excitation force. Further, measurements should be made on the sensor deviation error. This error gives the change of the point charge generated by the sensor at a given excitation force when the point is being approached by the dynamic force from either side. Lastly, since there is a strong relationship between piezoelectricity and ferroelectricity of a material, the ferroelectric hysteresis of the CNF should be equally measured and analyzed by use of a ferroelectric tester.

References

1. Sabo R., Yermakov A., Law C. T., Elhajjar R.. "Nanocellulose-Enabled Electronics, Energy Harvesting Devices, Smart Materials and Sensors": A Review.*J.Renew. Mater*. 4(5), 297-312, (2016)

2. Sabo R., Seo J. H., Ma Z., "Cellulose nanofiber composite substrates for flexible electronics", in: *2012 TAPPI International Conference on Nanotechnology for Renewable Materials*, Montreal, Quebec, Canada, (2012)

3. Okahisa Y., Yoshida A., Miyaguchi S., Yano H., "Optically transparent wood–cellulose nanocomposite as a base substrate for flexible organic light-emitting diode displays". *Compos. Sci. Technol.* 69(11), 1958–1961, (2009)

4. Fang Z., Zhu H., Y. Yuan, D. Ha, S. Zhu, C. Preston, Q. Chen, Y. Li, X. Han, and S. Lee, Novel nanostructured paper with ultrahigh transparency and ultrahigh haze for solar cells. *Nano Lett.,*14(2), 765–773 (2014)

5. Claeyssen F., Lhermet N., Le Letty R., Bouchilloux P., "Actuators, transducers and motors based on giant magnetostrictive materials". *J. Alloys and Compd.* 258(1), 61–73 (1997)

6. Jabbour L., Bongiovanni R., Chaussy D., Gerbaldi C., Beneventi D., Cellulose-based Li-ion batteries: A review. *Cellulose* 20(4), 1523–1545 (2013)

7. Nielsen L. J., Eyley S., Thielemans W., J.W. Aylott, "Dual fluorescent labelling of cellulose nanocrystals for pH sensing". *Chem. Commun.* 46(47), 8929–8931 (2010)

8. Luo Y., Zhang J., Li X., Liao C., "The cellulose nanofibers for optoelectronic conversion and energy storage". *J. Nanomater.*(2014)

9. Bower D. I., *An Introduction to Polymer Physics*, 1ST ed. New York: Cambridge University Press, Cambridge, (2002)

10. Strobl G., "The physics of polymers—Concepts for understanding their structures and behaviors," *Lect. Notes Phys*, 714(1), 87–96, (2007)

11. Rubinstein R. H., Michael and Colby, *Polymers Physics*, 23rd ed. (2003)

12. Schärtl W., *Light scattering from polymer solutions and nanoparticle dispersions*. Springer Science & Business Media, (2007)

13. Gordobil O., Egüés I., Urruzola I., Labidi J.,Xylan–cellulose films: Improvement of hydrophobicity, thermal and mechanical properties, *Carbohydrate Polymers*, 112, , 56-62, (2014)

14. Zuluaga, R., Putaux, J. L., Restrepo, A., Mondragon, I., &Ganán, P. Cellulose microfibrils from banana farming residues: isolation and characterization. Cellulose, 14(6), 585-592, (2007)

15. Dufresne A., Dupeyre D. and Vignon M. R., Cellulose microfibrils from potato tuber cells: Processing and characterization of starch–cellulose microfibril composites. *J. Appl. Polym*. Sci., 76, 2080–2092, (2000)

16. Hafraoui E., Nishiyama Y., Putaux J. L., L. Heux,F. Dubreuil and C. RochasThe shape and size distribution of crystalline nanoparticles prepared by acid hydrolysis of native cellulose. *Biomacromolecules,*9(1), 57–65,(2008)

17. Iguchi M., Yamanaka S.,Budhiono A., Bacterial cellulose—a masterpiece of nature's arts. *J. Mater. Sci.,* 35, 261–270, (2000)

18. Kim N.-H., HerthW., Vuong R., Chanzy H., "The Cellulose System in the Cell Wall of Micrasterias" *J. Struct. Biol*.,117, 195–203, (1996)

19. Titik I., Nur R., Richa R.., Metty M.,Slamet P.Heru S. "Cellulose Isolation from Tropical Water Hyacinth for Membrane Preparation"*Procedia Environmental Sciences* 23**,** 274 – 281, (2015)

20. Azizi Samir, M. A. S., Alloin, F., &Dufresne, A. Review of recent research into cellulosic whiskers, their properties and their application in nanocomposite field. Biomacromolecules, 6(2), 612-626, (2005)

21. Haworth, W.N., Hirst, E.L., and Thomas, H.A. The existence of the cellobiose residue in cellulose. Nature *126*, 438, (1930)

22. Moon R. J., AshlieNartini, John Nairn, John Simonsen and Jeph Youngblood. Cellulose nanomaterials review: Structure, properties and composites, *Chem. Soc. Rev.*, 40, 3941–3994, (2011)

23. Erwan Gicquel, Benard Cathala, Wim Thielemans "development of stimuli responsive cellulose nanocrystals hydrogel for smart applications. Thesis

24. Klemm D.,Heublein B., Fink H.P and Bohn A., Cellulose: Fascinating Biopolymer and Sustainable Raw Material. *Angew. Chem., Int. Ed.*, , 44, 3358–3393,(2005)

25. O'Sullivan AC, Cellulose: the structure slowly unravels.Cellulose 4:173–207(1997)

26. Yamamoto, H., & Horii, F. CPMAS carbon-13 NMR analysis of the crystal transformation induced for Valonia cellulose by annealing at high temperatures. *Macromolecules,* 26(6), 1313-1317, (1993)

27. Yamamoto, H., & Horn, F. In Situ crystallization of bacterial cellulose I. Influences of polymeric additives, stirring and temperature on the formation celluloses I α and I β as revealed by cross polarization/magic angle spinning (CP/MAS) 13C NMR spectroscopy. *Cellulose*, 1(1), 57-66, (1994)

28. Belton, P. S., Tanner, S. F., Cartier, N., &Chanzy, H. High-resolution solid-state carbon-13 nuclear magnetic resonance spectroscopy of tunicin, an animal cellulose. *Macromolecules*, 22(4), 1615-1617,(1989)

29. Watanabe, A., Morita, S., & Ozaki, Y.Temperature-dependent changes in hydrogen bonds in cellulose Iα studied by infrared spectroscopy in combination with perturbation-correlation moving-window two-dimensional correlation spectroscopy: comparison with cellulose Iβ. *Biomacromolecules,* 8(9), 2969-2975,(2007)

30. Debzi E. M., Chanzy H, Sugiyama J, TekelyT and Excoffier G., The Iα →Iβ transformation of highly crystalline cellulose by annealing in various mediums *Macromolecules,* 24, 6816–6822, (1991)

31. Nishiyama Y, Langan P and Chanzy H, Crystal Structure and Hydrogen-Bonding System in Cellulose Iβ from Synchrotron X-ray and Neutron Fiber Diffraction. *J. Am. Chem. Soc.*, 124, 9074–9082,(2002)

32. Nishiyama Y, Sugiyama J, Chanzy H and Langan P., Crystal Structure and Hydrogen Bonding System in Cellulose Iα from Synchrotron X-ray and Neutron Fiber Diffraction. *J. Am. Chem. Soc.*, 125, 14300–14306, (2003)

33. J. Sugiyama, R. Vuong and H. Chanzy, Electron diffraction study on the two crystalline phases occurring in native cellulose from an algal cell wall. *Macromolecules*, 24, 4168–4175, (1991)

34. Herrick, F. W., Casebier, R. L., Hamilton, J. K., and Sandberg, K. R. Microfibrillated cellulose: morphology and accessibility. *Journal of Applied Polymer Science. Applied Polymer Symposium*. 37: 797-813 (1983)

35. Turbak, A.F., Snyder, F.W., and Sandberg, K.R. Microfibrillated Cellulose, a New Cellulose Product: Properties, Uses, and Commercial Potential, *U*. S. (1983)

36. Dufresne, A. Nanocellulose: from nature to high performance tailored materials (Walter de Gruyter).GmbH & Co KG, (2013)

37. Habibi, Y., Chanzy, H., and Vignon, M.R. TEMPO-mediated surface oxidation of cellulose whiskers. *Cellulose13*, 679–687, (2006)

38. Nishiyama, Y. Structure and properties of the cellulose microfibril. *Journal of wood science,* 55(4), 241-249, (2009)

39. Brinchi, L., Cotana, F., Fourtunati, E., & Kenny, J. M. Production of anocrystalline cellulose from lignocellulosic biomass: Technology and applications. Carbohydrate Polymers, 94, 154-16, (2013)

40. Dufresne, A. Nanocellulose: From nature to high-performance tailored materials. deGruyter, Berlin/Boston, (2012)

41. Wilson Pires F. N. morphological investigation of cellulose nanocrystals and nanocomposites applications. Thesis (2017)

42. FlauzinoNeto, W. P., Silvério, H. A., Dantas, N. O., &Pasquini, D. Extraction and characterization of cellulose nanocrystals from agro-industrial residue-soy hulls Industrial Crops and Products, 42, 480-488, (2013)

43. Sèbe G., Ham-Pichavant, F., Ibarboure, E., Koffi, A. L. C., &Tingaut, P. Supramolecular structure characterization of cellulose II nanowhiskers produced by acid hydrolysis of cellulose I substrates. *Biomacromolecules*, 13, 570-578, (2012)

44. Kaushik, M., Fraschini, C., Grégory, C., Jean-Luc, P., & Moores, A. Transmission Electron Microscopy for the Characterization of Cellulose Nanocrystals. In: Khan Maaz

(ed.) The Transmission Electron Microscope – Theory and Applications, InTech. doi: 10.5772/60985, (2015)

45. Beaumont, M., Nypelö, T., Kö nig, J., Zirbs, R., Opietnik, M., Potthast, A., &Rosenau, T. Synthesis of redispersible spherical cellulose II nanoparticles decorated with carboxylate groups. *Green Chemistry,* 18, 1465-1468, (2016)

46. Trache, D., Tarchoun, A. F., Derradji, M., Hamidon, T. S., Masruchin, N., Brosse, N., &Hussin, M. H. Nanocellulose: From Fundamentals to Advanced Applications. *Frontiers in chemistry*, 8, 392, (2020)

47. Daniel, K. Hartmut, M. K. Fanuel, K. Susanna, H. Ralf, R. Günter, and S. Michael, "Poly(3-(2,5-dioctylphenyl)thiophene) Synthesized by Direct Arylation Polycondensation: End Groups, Defects, and Crystallinity," *Macromolecules*, 30, 8,. 1–8, (2016)

48. Wardhani K., INugraha. M. A., Abidin S., Ali M., and Fahmi A., "Solution of Reduced Graphene Oxide Synthesized from Coconut Shells and Its Optical Properties," *3rd Int. Conf. Adv. Mater. Sci. Technol.*, 020045, 1–8,(2017)

49. Song J., Wang X., and Chang C.T., "Preparation and Characterization of Graphene Oxide," *J. Nanomater.*, 20, 1–6, (2014)

50. . Till P. H., "The growth of single crystals of linear polyethylene," *J. Polym. Sci.*, 24, 106, 301–306, (1957)

51. Xu S., ZhangY., Dong K., Wen J., Zheng C., and Zhao S., "Electrochemical DNA Biosensor Based on Graphene Oxide- Chitosan Hybrid Nanocomposites for Detection of Escherichia Coli O157 : H7," *Int. J. Electrochem. Sci.*, 12, 3443–3458, (2017)

52. Davidson M., Michael W., and Abramowitz, "Optical microscopy," *Encycl. imaging Sci.*

Technol., 2, 1106–1141, (2002)

53. Reiter G.and. Strobl G. R, *Progress in Understanding of Polymer Crystallization*. Springer-Verlag Berlin Heidelberg, (2007)

54. Okura M.,. Mykhaylyk O. O, and. Ryan A. J, "Effect of Matrix Polymer on Flow-Induced Nucleation in Polymer Blends," 087801,. 1–5, (2013)

55. Xiao Z., Ilavsky J., Long G. G., and Akpalu Y. A., "Progress in Understanding of Polymer Crystallization," Berlin Heidelberg, (2007)

56. Muthukumar M., "Shifting Paradigms in Polymer Crystallization,"18, 1–2, (2007)

57. Wang J., and Ellsworth M.W., "Graphene and graphene oxide aerogels," *Google Patents*, 3, 8, 1–6, (2014)

58. Johnson S., *Stephen Johnson on Digital Photography*. O'Reilly Media, Inc., (2006)

59. Methods and Concepts in the Life Sciences/Spectroscopy - Wikibooks, open books for an open world

60. Ten Wolde P. R., and Frenkel D., "Homogeneous nucleation and the Ostwald step rule," *Phys. Chem. Chem. Phys.*,1, 9, 2191–2196, (1999)

61. Lossy R., Pappas D.L., Roy R.A., Doyle J.P., Cuomo J.J., and Bruley J., "Properties of amorphous diamond films prepared by a filtered cathodic arc," *J. Appl. Phys.*, vol. 77, 9,. 4750–4756, May (1995)

62. RubinsteinR. H., Michael and Colby, *Polymer Physics*, 23rd ed. North Carolina: Oxford University Press, (2003)

63. Mugwanga K. F., "Optical Studies on Indicators of Order and Disorder in Films and Crystals of a Bulky Substituted Polythiophene," Albert-Ludwigs-Universität Freiburg, (2018)

64. Ko A., Ho S. T. , Ba H., Köhler, S. T. Hoffmann, H. Bässler, A. Ko, S. T. Ho, and H. Ba, "An Order − Disorder Transition in the Conjugated Polymer MEH-PPV," *J. Am. Chem. Soc.*, 134,. 28,. 11594–601, (2012)

65. Schiefer D., Wen T., Wang Y., Goursot P., Komber H., Hanselmann R., Braunstein P., Reiter G., and Sommer M., "Nickel catalyst with a hybrid P, N ligand for kumada catalyst transfer polycondensation of sterically hindered thiophenes," *ACS Macro Lett.*, 3, 7, 617–621, (2014)

66. Carvalho J. L. and Dalnoki-Veress K., "Homogeneous bulk, surface, and edge nucleation in crystalline nanodroplets," *Phys. Rev. Lett.*, 105, 23,. 1–4, (2010)

67. Aziz S. B., "Morphological and Optical Characteristics of Nano-Composites : Optical Dielectric Loss as an Alternative Method for Tauc ' s Model," *Nanomaterials*, 7, 12, 1–15, (2017)

68. John A. O. and Jack A. A., "The Inter-play of the Opto-Electrical Properties of Cuprite and Tenorite Semiconductors for Solar Cell Application," *Am. J. Nano Res. Appl.*,5, 6, 81–86, (2017)

69. Velasco-Soto M. A., Pe´rez-Garcı´ S. A., Alvarez-Quintana J., Cao Y., Nyborg L., and Licea-Jime´nez L., "Selective band gap manipulation of graphene oxide by its reduction with mild reagents Selective band gap manipulation of graphene oxide by its reduction with mild reagents," *Carbon N. Y.*, 93, 6, 967–973, (2015)

70. Hasan T.,Senger B.J., Ryan C., Culp M., Gonzalez-rodriguez R., Coffer J. L., and Naumov A. V, "Optical Band Gap Alteration of Graphene Oxide via Ozone Treatment," *Sci. Rep.*, 7, 1–8, (2017)

71. Rack P. D., "Optical Microscopy," (2010)

72. Johnson S., *Stephen Johnson on Digital Photography*. O'Reilly Media, Inc., (2006)

73. M. Theander, M. Svensson, A. Ruseckas, D. Zigmantas, V. Sundström, M. R.

Andersson, and O. Inganäs, "High luminescence from a substituted polythiophene in a solvent with low solubility," *Chem. Phys. Lett.*, 337,277–283, (2001)

74. M. Scandola, G. Ceccorulli, M. Pizzoli, and M. Gazzano, "Study of the Crystal Phase and Crystallization Rate of Bacterial Poly(3-hydroxybutyrate-co-3-hydroxyvalerate)," *Macromolecules*, 25, 5, 1405–1410, (1992)

75. Visible Spectroscopy, "Visible Spectroscopy," (2014)

76. Agumba J. O., "Formation and Optical Characterization of Sin- gle Crystals of Poly (3-Hexylthiophene)(P3HT), a Model Conjugated Polymer," Albert-Ludwigs-Universität Freiburg, (2015)

77. Berberan-Santos M. N. , Pioneering Contributions of Jean and Francis Perrinto Molecular Luminescence, In New Trends in *Fluorescence Spectroscopy: Applications to Chemical and Life Sciences*; B. Valeur, J. –C. Brochon, Eds.; Springer Series on Fluorescence Methods and Applications; Springer Verlag, 18-19, (2001)

78. Valeur B, Berberan-Santos M. N., Introduction, Molecular Fluorescence: Principles and Applications, 2nd Ed. Wiley-VCH 01-25, (2012)

79. Valeur B., Introduction: On the Origin of the Terms Fluorescence, Phosphorescence, and Luminescence, In *New Trends in Fluorescence Spectroscopy:* Applications to Chemical and Life Sciences; Springer Series on Fluorescence Methods and Applications; Springer Verlag ,3-6, (2001)

80. IUPAC, *Compendium of Chemical Terminology*, 2nd ed. (the "Gold Book"); Compiled by A. D. McNaught and A. Wilkinson. Blackwell Scientific Publications (1997)

81. J. R. Lacowicz, Introduction to Fluorescence, *Principles of Fluorescence Spectroscopy*, 3rd Ed. Springer US,3-6,(2006)

82. Kwok K.W., Chan H.L.W., Choy, C.L. Evaluation of the material parameters of piezoelectric materials by various methods. IEEE Trans. Ultrason. Ferroelectr. Freq. Control 44, 733–742 (1997)

83. Wu J.,,Du G. Analogy between the one-dimensional acoustic waveguide and the electrical transmission line for cases with loss. J. Acoust. Soc. Am. 100, 3973–3975 (1996)

84. Harrison JS, Ounaies Z. Piezoelectric polymers. In: Encyclopedia of Polymer Science and Technology. Hoboken, NJ, USA: John Wiley & Sons, Inc.; 2002. p. 3. DOI: 10.1002/0471440264.pst427

85. Fukada E. Piezoelectricity as a fundamental property of wood. *Wood Science and Technology*, 2(4):299-307, (1968)

86. SampoTuukkanen and SatuRajalaNanocellulose as a Piezoelectric MaterialOrganic and Inorganic Materials and Applications http://dx.doi.org/10.5772/intechopen.77025

87. Jasmani L, Thielemans W Preparation of Nanocellulose and its Potential Application. *Forest Res* 7: 222. doi: 10.4172/2168-9776.1000222, (2018)

88. Moon RJ, Martini A, Nairn J, Simonsen J, Youngblood J. Cellulose nanomaterials review: Structure, properties and nanocomposites. ChemSoc Rev 40: 3941-3994, (2011)

89. Elazzouzi-Hafraoui, S., Nishiyama, Y., Putaux, J. L., Heux, L., Dubreuil, F., &Rochas, C. The shape and size distribution of crystalline nanoparticles prepared by acid hydrolysis of native cellulose. *Biomacromolecules*, 9(1), 57-65, (2008)

90. Garcia de Rodriguez, N. L., Thielemans, W., &Dufresne, A. Sisal cellulose whiskers reinforced polyvinyl acetate nanocomposites. *Cellulose,* 13(3), 261-270, (2006)

91. Helbert, W., Cavaille, J. Y., &Dufresne, A. Thermoplastic nanocomposites filled with wheat straw cellulose whiskers. Part I: processing and mechanical behavior. *Polymer*

composites, 17(4), 604-611, (1996)

92. Beaumont M, Rennhofer H, Opietnik M, Lichtenegger H, Potthast A, Rosenau T Nanostructured Cellulose II Gel Consisting of Spherical Particles. ACS SustainableChemistry & Engineering 4:4424-4432, (2016) doi: 10.1021/acssuschemeng.6b01036

93. Jasmani L, Thielemans W. Preparation of Nanocellulose and its Potential Application. Forest Res 7: 222, (2018).doi:10.4172/2168-9776.1000222

94. Moon RJ, Martini A, Nairn J, Simonsen J, Youngblood J. Cellulose nanomaterials review: Structure, properties and nanocomposites. ChemSoc Rev 40: 3941-3994, (2011)

95. Elazzouzi-Hafraoui, S., Nishiyama, Y., Putaux, J. L., Heux, L., Dubreuil, F., &Rochas, C. The shape and size distribution of crystalline nanoparticles prepared by acid hydrolysis of native cellulose. *Biomacromolecules*, 9(1), 57-65, (2008)

96. Garcia de Rodriguez, N. L., Thielemans, W., &Dufresne, A. Sisal cellulose whiskers reinforced polyvinyl acetate nanocomposites. *Cellulose*, 13(3), 261-270, (2006)

97. Helbert, W., Cavaille, J. Y., & Dufresne, A. Thermoplastic nanocomposites filled with wheat straw cellulose whiskers. Part I: processing and mechanical behavior. *Polymer composites*, 17(4), 604-611,(1996)

98. Dufresne, A., Dupeyre, D., &Vignon, M. R. Cellulose microfibrils from potato tuber cells: processing and characterization of starch–cellulose microfibril composites. *Journal of applied polymer science*, 76(14), 2080-2092, (2000)

99. Leitner, J., Hinterstoisser, B., Wastyn, M., Keckes, J., &Gindl, W. Sugar beet cellulose nanofibril-reinforced composites. *Cellulose*, 14(5), 419-425, (2007)

100. Wang, B., &Sain, M. Isolation of nanofibers from soybean source and their reinforcing capability on synthetic polymers. *Composites Science and Technology*, 67(11-12), 2521-2527, (2007)

101. Iwamoto, S., Kai, W., Isogai, A., & Iwata, T. Elastic modulus of single cellulose microfibrils from tunicate measured by atomic force microscopy. *Biomacromolecules*, 10(9), 2571-2576, (2009)

102. Revol, J. F. On the cross-sectional shape of cellulose crystallites in Valoniaventricosa. *Carbohydrate Polymers*, 2(2), 123-134, (1982)

103. Zimmermann T., Bordeanu N and E.,Strub.,"Properties of Nanofibrillated Cellulose from Different Raw Materials and Its Reinforcement Potential," *Carbohydr. Polym*. 79, 1086–1093, (2010)

104. Asrofi, Mochamad, HairulAbral, Anwar Kasim, AdjarPratoto, MelbiMahardika, Ji-Wo Park, and Hyun-Joong Kim. "Isolation of nanocellulose from water hyacinth fiber (WHF) produced via digester-sonication and its characterization." *Fibers and Polymers*, 19, 8: 1618-1625, (2018)

105. Lee, H. V., Sharifah Bee Abd Hamid, and S. K. Zain. "Conversion of lignocellulosic biomass to nanocellulose: structure and chemical process." *The Scientific World Journal,* 2014 (2014)

106. Pitaloka, A. B., Saputra, A. H., &Nasikin, M. Water hyacinth for superabsorbent polymer material. *World Applied Sciences Journal*, 22(5), 747-754, (2013)

107. Dos Santos, Roni Marcos, Wilson PiresFlauzinoNeto, Hudson AlvesSilvério, Douglas Ferreira Martins, Noélio Oliveira Dantas, and Daniel Pasquini. "Cellulose nanocrystals

from pineapple leaf, a new approach for the reuse of this agro-waste." *Industrial Crops and Products*, 50: 707-714, (2013)

108. Athinarayanan, Jegan, Ali A. Alshatwi, and VaiyapuriSubbarayanPeriasamy. "Biocompatibility analysis of Borassusflabellifer biomass-derived nanofibrillated cellulose" *Carbohydrate Polymers*, 235: 115961, (2020)

109. Hubbe, M. A., Rojas, O. J., Lucia, L. A., &Sain, M. Cellulosic nanocomposites: A review. *BioResources,* 3(3), 929-980, (2008)

110. Siro, I. & Plackett, D. Microfibrillated cellulose and new nanocomposite materials: a review. *Cellulose*, 17, 459-494

111. Iwamoto S, Nakagaito A.N and Yano H., Nano-fibrillation of pulp fibers for the processing of transparent nanocomposites. *Appl. Phys. A:Mater. Sci. Process*., 89, 461–466, (2007)

112. Chakraborty, A.,Sain M., &Kortschot M., Cellulose microfibrils: a novel method of preparation using high shear refining and cryocrushing. Holzforschung, 59,102–107, (2005)

113. Johnson,R. K., Zink-Sharp, A.,RenneckarS. H., andGlasser,W. G. A new bio-based nanocomposite: fibrillated TEMPO-oxidized celluloses in hydroxypropylcellulose matrix. *Cellulose,* 16, 227–238, (2009)

114. NickersonR. F., and Habrle J. A., "Cellulose intercrystalline structure," *Industrial & Engineering Chemistry*, 39, 11,. 1507–1512, (1947)

115. Ranby B. G., "Fibrous macromolecular systems. Cellulose and muscle. The colloidal properties of cellulose micelles," *Discussionsof the Faraday Society*, 11, 158–164, (1951)

116. Haafiz M. K. M., Hassan A, Zakaria Z., and Inuwa I.M., "Isolation and characterization of cellulose nanowhiskers from oil palm biomass microcrystalline cellulose," *CarbohydratePolymers*, vol. 103, no. 1, pp. 119–125, (2014)

117. Yu H., Qin Z., Liang B., Liu N., Zhou Z., and Chen L., "Facile extraction of thermally stable cellulose nanocrystals with a high yield of 93% through hydrochloric acid hydrolysis under hydrothermal conditions," *Journal of Materials Chemistry*, 12, 3938–3944, (2013)

118. Li S., Li C, Li C.., "Fabrication of nano-crystalline cellulose with phosphoric acid and its full application in a modified polyurethane foam," *Polymer Degradation and Stability*, 98, 9, 1940–1944, (2013)

119. Sadeghifar H., Filpponen I, ClarkeS. P., BroughamD. F., and ArgyropoulosD. S., "Production of cellulose nanocrystals using hydrobromic acid and click reactions on their surface," *Journalof Materials Science*, 46, 22,7344–7355, (2011)

120. Rosa M. F., Medeiros E. S., Malmonge J. A., "Cellulose nanowhiskers from coconut husk fibers: effect of preparation conditions on their thermal and morphological behavior," *Carbohydrate Polymers*, 81, 1, 83–92, (2010)

121. Lynd L. R., Weimer P. J., Van Zyl W. H., and Pretorius I. S., "Microbial cellulose utilization: fundamentals and biotechnology," *Microbiology and Molecular Biology Reviews*, 66, 3, 506–577, (2002)

122. FilsonP. B., Dawson-Andoh B. E., and Schwegler-Berry D., "Enzymatic-mediated production of cellulose nanocrystals from recycled pulp," *Green Chemistry*, 11,1808-1814, (2009)

123. Sacui I. A, Nieuwendaal R.C., Burnett D.J.,Comparison of the Properties of Cellulose Nanocrystals and Cellulose Nanofibrils Isolated from Bacteria, Tunicate, and Wood Processed Using Acid, Enzymatic, Mechanical, and Oxidative Methods. *ACS Appl Mater Interfaces*, 6:6127–6138,(2014)

124. Meriko E.,**"Preparation and characterizations of cellulosenanofibers from water hyacinth and their application as reinforcement for recycled paper"**

125. Asrofi M, Abral H., Kasim A., and Pratoto, "XRD and FTIR Studies of NanocrystallineCellulose from Water Hyacinth (Eichorniacrassipes)Fiber,"*J. Metastable Nanocrystalline Mater*., 29,9 (2017)

126. Abraham E., Deepa B.,.Pothan L. A, Jacob M.,Thomas S., Cvelbar U,Anandjiwala R, "Extraction of nanocellulose fibrils from lignocellulosicfibres: a novel approach. Carbohydrate Polymers," *Carbohydr.Polym*., 86, 1468-1475, (2011)

127. Lani N. S., Ngadi N., Johari A., and Jusoh M., Isolation, Characterization, and application of Nanocellulose from Oil Palm Empty Fruit Bunch Fiber as Nanocomposites, *J. Nanomater*.,3, 1-9 (2014)

128. Cherian B.M, Pothan L.A., Nguyen-Chung T . A novel method for the synthesis of cellulose nanofibril whiskers from banana fibers and characterization. *J Agric Food Chem* 56, 5617–5627, (2008)

129. Onyianta A. J., Dorris M., Williams RL Aqueous morpholine pre-treatment in cellulose nanofibril (CNF) production: comparison with carboxymethylation and TEMPO oxidization pre-treatment methods. *Cellulose*, 25, 1047–1064, (2018)

130. Abraham, E, B. Deepa, L. A. Pothan, M. Jacob, S. Thomas, U. Cvelbar, and R. Anandjiwala. "Extraction of nanocellulose fibrils from lignocellulosicfibres: A novel approach." *Carbohydrate Polymers* 86, 4: 1468-1475, (2011)

131. Chandra S. J., George N , and Narayanankutty S. K., Isolation and characterization of cellulose nanofibrils from arecanut husk fibre, *Carbohydr.Polym*., 142: 158-166

132. Setyaningsih L., Satria E., Khoironi H., Dwisari M., Setyowati G., Rachmawati N., Kusuma R., and Anggraeni J.,Cellulose extracted from water hyacinth and theapplication in hydrogel.*IOP Conf. Ser.: Mater. Sci. Eng.,*673, 012017,(2019)

133. Oliveira J. P., Bruni G. P., Lima K. O., Halal S. L. M., Rosa G. S., Dias A. R. G. and Zavarese E. R., Cellulose fibers extracted from rice and oat husks and their application in hydrogel. *Food Chemistry* 221, 153-160, (2017)

134. Halal S , Pinto V. Z., Villanova, F A and Carreno N. L. V.Films based on oxidized starch and cellulose from barley.*Carbohydrate Polymers* 133, 644-653, (2015)

135. Alemdar A and Sain M 2008 Alemdar, A., & Sain, M. (2008). Isolation and characterization of nanofibers from agricultural residues–Wheat straw and soy hulls. Bioresource technology. *Bioresource Technology,* 99, 1664-1671 (2009)

136. Trilokesh C., and Babu K.U., Isolation and characterization of cellulose nanocrystals from jackfruit peel.*Sci., Rep*., 9, 16709 (2019)

137. Bich T. N. T., Luong H. V. T., Lan T. N. P., Thuy N. T. D., Ju Y.H., Comparison of Some Pretreatment Methods on Cellulose Recovery from Water Hyacinth (EichhorniaCrassipe), *Journal of Clean Energy Technologies*, 5 (4), (2017)

138. Xuezhu X., Fei L., Long J., Zhu J. Y., Darrin H., and Wiesenborn D.P.*, Cellulose Nanocrystals vs. Cellulose Nanofibrils: A Comparative Study on Their Microstructures and Effects as Polymer Reinforcing Agents, *ACS Appl. Mater. Interfaces*, 5, 8, 2999–3009, (2013)

139. Csoka L., Hoeger I.C., Rojas, I. Peszlen O. J., Pawlak J. J., and Peralta P. N.. "Piezoelectric effect of cellulose nanocrystals thin films". *ACS Macro Letters*, 1(7) 867-870, (2012)

140. Fukada E., "Piezoelectricity of wood". *Journal of thePhysical Society of Japan*, vol. 10(2), 149-154, (1955)

141. Firka-Petesic B., Jean B., and Heux L., "First experimental evidence of a giant permanent electric-dipole moment in cellulose nanocrystals". *Europhysics Letters,*107(2), 28006, (2014)

142. Rajala S., Vuoriluoto M., Rojas O. J., Franssila S., Tuukkanen S. ''Piezoelectric sensitivity measurements of cellulose nanofibril sensors. *XXI IMEKO World Congress "Measurement in Research and Industry*, (2015)

143. Agumba J. O., "Formation and Optical Characterization of Single Crystals of Poly (3-Hexylthiophene) (P3HT), a Model Conjugated Polymer," Albert-Ludwigs-Universität Freiburg, (2015)

144. Methods and Concepts in the Life Sciences/Spectroscopy - Wikibooks, open books for an open world." [Online]. Available: https://en.wikibooks.org/wiki/Methods and Concepts in the Life Sciences/Spectroscopy. [Accessed: 22-Feb-2019]

145. Kadla J. F., Gilbert R. D., Cellulose Structure: *Review, Cellulose Chemistry and Technology*, 34: 197-216 (2000)

146.Brito B. S. L., Pereira F. V., Putaux J. -L, Jean B. Preparation, morphology and structure of cellulose nanocrystals from bamboo fibers, *Cellulose,* 19:1527–1536, (2012)

147.Iwamoto S., Nakagaito A. N., Yano H. Nano-fibrillation of pulp fibers for the processing of transparent nanocomposites, *Appl. Phys*, 89:461-466, (2007)

148.Nishino T., Takano K., Nakamae K. Elastic modulus of the crystalline regions of cellulose polymorphs, *J. Polym. Sci. B Polym*. Phys, 33:1647-1651, (1995)

149.Iwamoto S., Abe K., Yano H., The effect of hemicelluloses on wood pulp nanofibrillation and nanofiber network characteristics. *Biomacromolecules*, 9:1022-1026, (2008)

150.Brinchi L., Cotana F., Fortunati E. and Kenny J. M,. Carbohydrate Polymer. 94 154-169, (2013) doi 10.1016/j.carbpol.2013.01.033

151.Wang N. D. and Cheng R. *Polymer.* 48: 3486-3493, (2007)

152.Salas C., Nypelö T., Abreu C. R., Carrillo C. and Rojas O. J., Current Opinion in Colloids & Interface Science, 19 383-396, (2014)

153.Habibi Y., Lucia L. A. and Rojas O. J., Chemical Reviews, 110: 3479-3500, (2010)

154.Van Vliet C. M. Band gap narrowing and emitter efficiency in heavily doped emitter structures revisited," in IEEE Transactions on Electron Devices 40 (6): 1140-1147, (1993), doi: 10.1109/16.214741

155.Kamarulzaman N., Kasim, M. F., Rusdi, R Band gap Narrowing and Widening of ZnO Nanostructures and Doped Materials. *Nanoscale Res Lett* 10**:** 346, (2015) https://doi.org/10.1186/s11671-015-1034-9

156. O'sullivan, A. C. Cellulose: the structure slowly unravels. *Cellulose, 4*(3), 173-207, (1997)

157. Wada M., Sugiyama J., Okano T., Native celluloses on the basis of two crystalline phase (Iα/Iβ) system, *J. Appl. Polym Sci.* 491491-1496, (1993)

158. Mott N.F, Davis E.A. "Electronic Processes in Non-crystalline Materials" Clarendon Press, Oxford, (1979)

159. Li W., Yue J. Liu S. Li, W., Yue, J. and Liu, S., 2012. Preparation of nanocrystalline cellulose via ultrasound and its reinforcement capability for poly (vinyl alcohol) composites. *Ultrasonics sonochemistry*, *19*(3), pp.479-485.. *Sonochem*. 19, 479-485, (2012)

160. Singh J. "Optical Properties of Condensed Matter and Applications" John Wiley & Sons Ltd, (2006)

161. Adachi S "Optical Properties of Crystalline and Amorphous Semiconductors" Materials and Fundamental Principles Springer Science + Business Media, LLC, (1999)

162. Urbach F "The Long-Wavelength Edge of Photographic Sensitivity and of the Electronic Absorption of Solids", *Physical Review.* 92 1324: 1-5, (1953) doi:https://doi.org/10.1103/PhysRev.92.1324

163. Boubaker K "A physical explanation to the controversial Urbach tailing universality" *The European Physical Journal Plus*. 126 (10): 1-4 , (2011), doi:10.1140/EPJP/I2011-11010-4

164. Choudhury B., Borah B. and Choudhury A. "Extending Photocatalytic Activity of TiO_2 Nanoparticles to Visible Region of Illumination by Doping of Cerium Photochemistry and Photobiology" 88: 257-64, (2012) doi: 10.1111/j.1751-1097.2011.01064.x.

165. Bos A. The UV spectra of cellulose and some model compounds *J. Applied Polymers*, 16 (10): 2567-2576, (1972) https://doi.org/10.1002/app.1972.070161010

166. Simao C. D., Reparaz J.S., Wagner M. R., "Nanocellulose in Thin Films, Coatings, and Plies for Packaging Applications" A Review. *Carbohydrate Polymers*, 03: 032, (2015) doi.10.15376/biores.12.1.2143-2233

167. Mwanze C. "The Effect of Temperature on Hydrolysis of Cellulose" Thesis, Caritus University, Enugu Estate, (2013)

168. Dandan Q, Meiyun Z, Jinbao L.Qiang L."Selective hydrolysis of cellulose for the preparation of microcrystalline cellulose by phosphotungstic acid" 41 (10): 1140-1147, (2003), doi: 10.1108/16.214767

169. Ielovich M."Preparation of amorphized cellulose and nano-cellulose by treatment of cellulose fibers with concentrated solutions of sulfuric acid" *Sci., Rep.*, 10, 16710 (2017)

170. Xurun Y. "Influence of Grain Size on the Band-gap of Annealed SnS Thin Films" *Journal of Mat. Sci.* 28, 1047–1064, (2017)

171. Neha Sharma, Shilpam Sharma, K. Prabakar, S. Amirthapandian, S. Ilango, S. Dash and A. K. Tyagi "Optical band gap and associated band-tails in nanocrystalline AlN thin films grown by reactive IBSD at different substrate temperatures Material Science Group" *Indira Gandhi Centre for Atomic Research Kalpakkam* 603102, TN, India 129–270, (2018)

Appendices

Appendix 1: Research Permit from the Board of Postgraduate Studies

JARAMOGI OGINGA ODINGA UNIVERSITY OF SCIENCE & TECHNOLOGY

BOARD OF POSTGRADUATE STUDIES
Office of the Director

Tel. 057-2501804
Email: bps@jooust.ac.ke

P.O. BOX 210 - 40601
BONDO

Our Ref: S261/4168/2015

Date: 19th July 2021

TO WHOM IT MAY CONCERN

RE: JACK ABIBO ADEM – S261/4168/2015

The above person is a bonafide postgraduate student of Jaramogi Oginga Odinga University of Science and Technology in the School of Biological, Physical, Mathematics and Actuarial Sciences pursuing PhD in Physics. He has been authorized by the University to undertake research on the topic: *"Experimental Study of the Degree of Alignment and Piezoelectric Effect of Cellulose Nanocrystals Fabricated from Water Hyacynth."*

Any assistance accorded him shall be appreciated.

Thank you.

Prof. Dennis Ochuodho
DIRECTOR, BOARD OF POSTGRADUATE STUDIES

Appendix 2: Ethics and Review Committee Research Permit

JARAMOGI OGINGA ODINGA
UNIVERSITY OF SCIENCE AND TECHNOLOGY

DIVISION OF RESEARCH, INNOVATION AND OUTREACH
JOOUST-ETHICS REVIEW OFFICE

Tel: 057-2501804
Email: erc@jooust.ac.ke
Website: www.jooust.ac.ke

P.O. BOX 210 - 40601
BONDO

OUR REF: JOOUST/DVC-RIO/ERC/E4

29ᵗʰ July, 2021

Jack Abibo
SBPMAS
JOOUST

Dear Mr. Abibo,

RE: APPROVAL TO CONDUCT RESEARCH TITLED "CORRELATION BETWEEN THE DEGREE OF ALIGNMENT AND PIEZOELECTRIC EFFECT OF CELLULOSE NANOCRYSTALS FABRICATED FROM WATER HYACINTH"

This is to inform you that JOOUST ERC has reviewed and approved your above research proposal. Your application approval number is ERC 23/7/21-9. The approval period is from 29ᵗʰ July, 2021 – 28ᵗʰ July, 2022.

This approval is subject to compliance with the following requirements:
i. Only approved documents including (informed consents, study instruments, MTA) will be used.
ii. All changes including (amendments, deviations and violations) are submitted for review and approval by JOOUST IERC.
iii. Death and life threatening problems and serious adverse events or unexpected adverse events whether related or unrelated to the study must be reported to NACOSTI IERC within 72 hours of notification.
iv. Any changes, anticipated or otherwise that may increase the risks of affected safety or welfare of study participants and others or affect the integrity of the research must be reported to NACOSTI IERC within 72 hours.
v. Clearance for export of biological specimens must be obtained from relevant institutions.
vi. Submission of a request for renewal of approval at least 60 days prior to expiry of the approval period. Attach a comprehensive progress report to support the renewal.
vii. Submission of an executive summary report within 90 days upon completion of the study to JOOUST IERC.

Prior to commencing your study, you will be expected to obtain a research permit from National Commission for Science, Technology and Innovation (NACOSTI) https:oris.nacosti.go.ke and also obtain other clearances needed.

Yours sincerely,

for
Prof. Francis Anga'wa
Chairman, JOOUST ERC

Copy to: Deputy Vice-Chancellor, RIO   Director, BPS   DEAN, SBPMAS

151

Appendix 3: NACOSTI Research Permit